7 Assessment of Cardiac Function: First-Pass, Equilibrium Blood Pool, and Gated Myocardial SPECT

Elias H. Botvinick, Nick G. Costouros, Stephen L. Bacharach, and J. William O'Connell

Introduction

Radionuclide-based techniques have been used to measure ventricular function for over three decades [1–8]. As shown in Fig. 7.1a, the methods for measurement of ventricular function can be divided into two basic categories. The first category employs any tracer that can directly label the blood pool itself. One then examines the deformity of the cavitary blood pool as it is moved by the thickening and systolic motion of the myocardial walls. With these methods, one can directly image the blood pool in the ventricular cavity throughout the cardiac cycle. The second category of methods for measurement of ventricular function uses tracers that label the myocardial walls (e.g., ^{99m}Tc-sestamibi, [^{18}F]-fluorodeoxyglucose). One then examines how those walls thicken and translate, move, or contract throughout the cardiac cycle. With this method, one can directly image the myocardium throughout the cardiac cycle. Active movement or contraction of the inner endocardial wall of the ventricular chamber compresses the blood pool and deforms the ventricular cavity and is the conventional marker for systolic ventricular wall motion or function. Only this method permits the evaluation of myocardial wall thickening, a marker of systolic function and viability that can help separate passive systolic wall motion from active myocardial contraction. This method for measuring ventricular mechanical function simultaneously yields a measurement of myocardial perfusion or of metabolism (depending on the tracer used to label the myocardium), but this advantage is also a source of one of the method's disadvantages: If perfusion or metabolism is reduced in a particular segment of the myocardium, then that segment is not easily visualized, hampering visualization of wall motion or thickening in that segment. Temporal and spatial resolution of the related functional image data is not as good as for the blood pool method.

E. H. Botvinick (✉)
University of California San Francisco School of Medicine, San Francisco, CA, USA

N. G. Costouros
Department of Radiology, University of California San Francisco School of Medicine, San Francisco, CA, USA

S. L. Bacharach
Department of Radiology, Center for Molecular and Functional Imaging, University of California San Francisco School of Medicine, San Francisco, CA, USA

J. W. O'Connell
University of California San Francisco School of Medicine, San Francisco, CA, USA

V. Dilsizian, J. Narula (eds.), *Atlas of Nuclear Cardiology*, https://doi.org/10.1007/978-3-030-49885-6_7

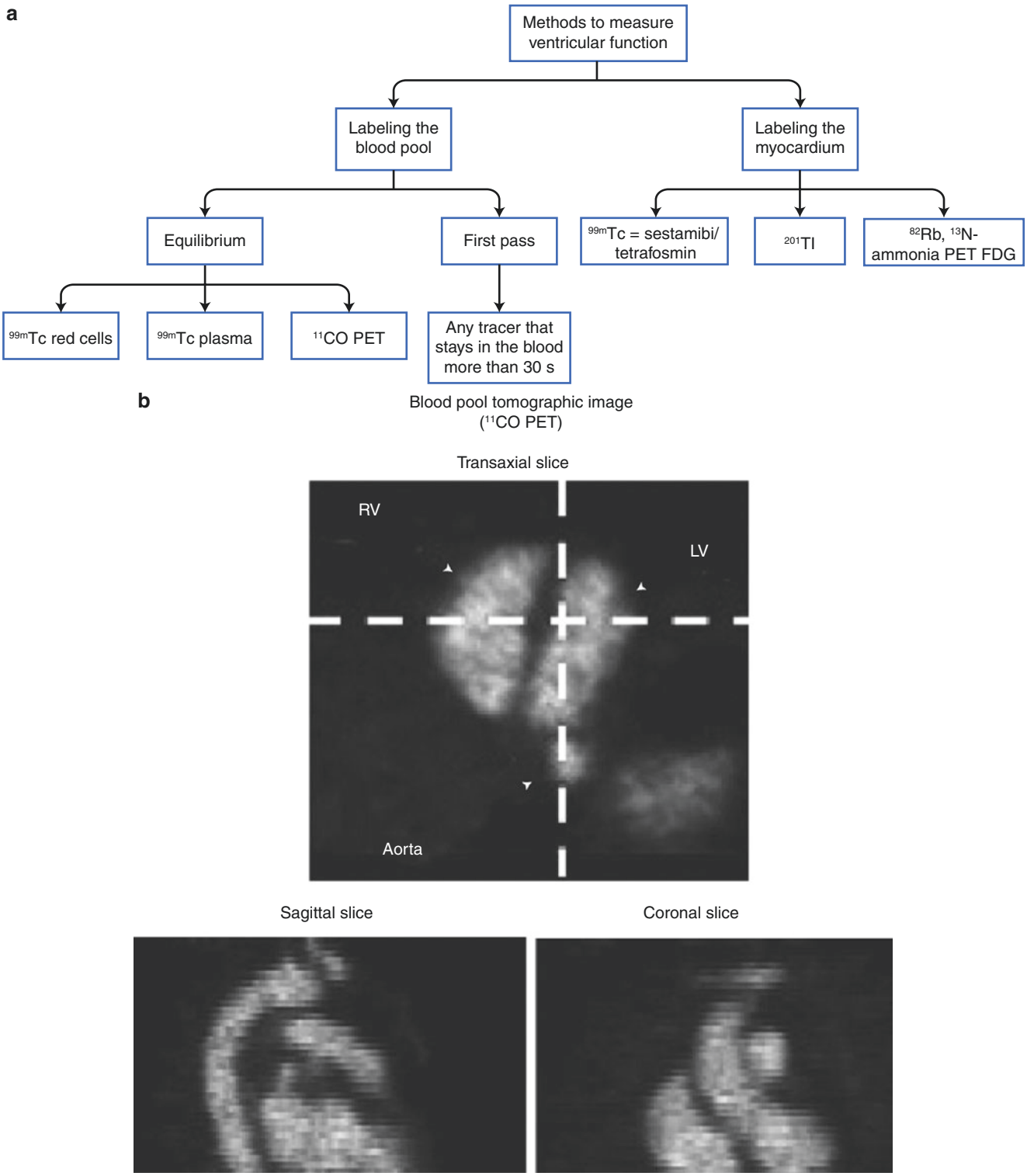

Fig. 7.1 (**a**) The methods for measurement of ventricular function can be divided into two basic categories. The first category employs any tracer that can directly label the blood pool itself. The second category uses tracers that label the myocardial walls. (**b**) Images produced from ^{11}CO PET. Transaxial slices, which display tomographic slices of the heart as it lies in the chest, are reconstructed at orthogonal angles in sagittal and coronal projections. (**c**) Diagrammatic illustration of reconstruction of the blood pool along the long axis of the left ventricle. (**d**) The resulting horizontal long-axis (HLA) and vertical long-axis (VLA) slices. ED end diastolic, ES end systolic, FDG fluorodeoxyglucose, LV left ventricle, RV right ventricle

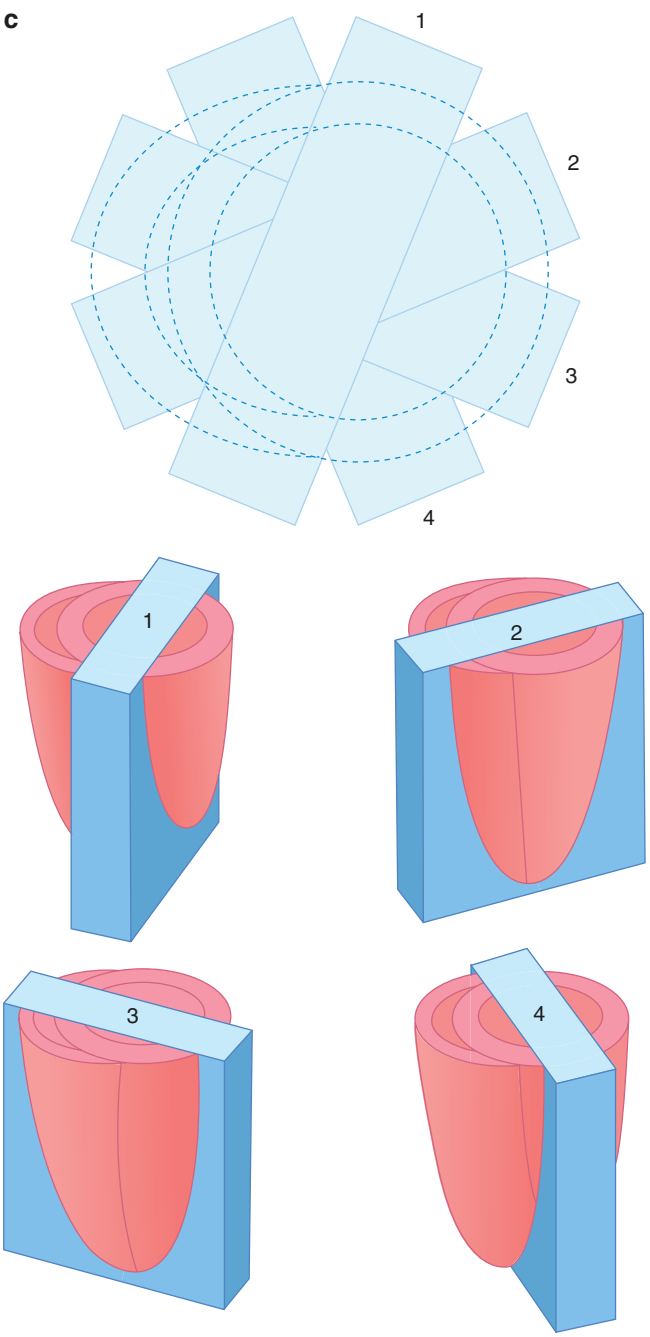

Fig. 7.1 (continued)

Both of the above methods may be gated with an electrocardiogram signal, which permits observation of either the blood pool or the myocardium throughout the cardiac cycle. The data can be displayed as a cine to either view or can be used to compute the left ventricular ejection fraction. The two methods are complementary to some extent, but give slightly different information. The blood pool method directly measures the changing volume of the blood in the cardiac chambers with time. The motion of the adjacent myocardial walls is inferred from the measured regional or global changes and motion in the blood pool contour and blood volume. The labeled myocardium methodology directly measures the motion of the walls. One must then infer changes in blood volume from that motion. Each method has its advantages and disadvantages. This chapter explores the advantages and disadvantages of both methods of measuring ventricular function, as well as how each can be applied clinically.

In recent years, there has been a rich addition of cardiac imaging methods. Each has specific advantages and disadvantages. Many are offered by imaging specialists; others are available within the cardiology practice. With this development, the cardiologist has taken an ever-increasing role in the performance of cardiac imaging studies. The American Society of Nuclear Cardiology has flourished as a vehicle of support, training, and research for all specialists seeking a role in this imaging specialty. Though some have sought a wide application, with studies performed according to the clinical setting, the specific advantage of the method, and its availability, others have simply relied on their favorite method. Studies performed and billed by the cardiologist, such as echocardiography, have found increased use. Applied mostly for its abilities and availability, this method is undeniably too often preferred, with prejudice based on non-clinical motives that are too often economic. Owing to these processes, some deserved and some not, the volume of nuclear blood pool imaging studies has diminished greatly over the years since it was the most frequently ordered nuclear cardiology study. Nonetheless, the method possesses strong advantages of accuracy, objectivity, and reproducibility. An additional major, unique advantage over echocardiography is its digital nature, with intensity/counts directly related to blood volume, permitting the formulation and derivation of parameters not available in any other way. Thus, functional imaging with the development of parametric images as "phase imaging" presents opportunities to assess characteristics of myocardial contraction that can contribute greatly to our understanding of cardiac pathology and our clinical approach to it. Soon the issue will again evolve to the question of whether the cardiology community will adapt and apply a method they do not control simply for its unique clinical advantages. The electrophysiologist may lead the way!

Blood Pool Imaging of Ventricular Function

The methods for measurement of ventricular function can be divided into two basic categories (Fig. 7.1a) The first category employs any tracer that can directly label the blood pool itself. The second category uses tracers that label the myocardial walls; one then examines how those walls thicken and translate, move, or contract throughout the cardiac cycle. For the measurement of ventricular function, labeling the blood pool has the advantage of providing a direct measure of left ventricular (LV) volumes. In the ideal circumstance, the method provides true quantitatively accurate imaging, and a measurement of absolute volume can be obtained directly from the images, since radioactivity per volume (i.e., the concentration of activity in the ventricular blood pool, or Bq/mL) can be measured within the LV chamber as well as the total Bq within the cavity. The LV volume is then calculated from the number of Bq in the entire chamber. Unfortunately, the ability to make accurate quantitative measurements of Bq/mL from image data is usually limited to positron emission tomography (PET) [9, 10]. The more common single-photon tomographic measurements can only produce quantitatively accurate results with great difficulty and actual blood counting. Inaccuracies are even greater with planar imaging. Nonetheless, single-photon emission CT (SPECT) blood pool techniques have made considerable progress in recent years [11–14]. Fortunately, for nearly all clinical applications, one is usually content to make relative measurements of ventricular function, such as ejection fraction. These relative measurements, unlike measurements of absolute volumes, depend only on relative rather than absolute accuracy of the imaging modality. For this reason, planar imaging methods can do quite well [15], although for regional measures of function using a blood pool tracer, SPECT offers some advantages [16–19].

For anatomical orientation, it is useful to first examine the higher-resolution images produced from ^{11}CO PET (Fig. 7.1b), before inspecting identical but lower resolution, SPECT gated blood pool images shown in Fig. 7.39. Transaxial slices are reconstructed at orthogonal angles in sagittal and coronal projections. Clinically, as for myocardial perfusion imaging, the blood pool is reconstructed along the long axis of the left ventricle, as illustrated diagrammatically in Fig. 7.1c, to present the horizontal and vertical long-axis slices illustrated in (**d**). Alternatively, C^{15}O has also been used, but has the disadvantage of a short (2 min) half-life. Labeling the myocardium provides direct visualization of the myocardial walls throughout the cardiac cycle. It provides only an indirect measurement of the changes in blood volume; these must be inferred from measurement of the endocardial edges, a difficult task given the resolution of nuclear techniques, but one that has proven quite feasible [20]. The method could, in principle, be used to directly measure regional myocardial thickening as well [21, 22]. The actual measurement of linear thickening has proven more difficult to accomplish with SPECT than with higher-resolution methods such as gated CT or MRI. However, intensity changes can be used to track thickening (as described below), and the gated labeled myocardial method has been widely adopted because it permits measurement of LV function simultaneously with perfusion or metabolism. Thus, one can perform two measurements with only a single injection and a single imaging session—a great logistical and financial incentive. The method has been used successfully with both SPECT and PET, but not with planar imaging.

First-Pass *Versus* Equilibrium Method

There are two methods of blood pool imaging based on the state of radiotracer mixing: the first-pass method and the equilibrium method. The first-pass method extracts data during the first passage of the radionuclide through the central circulation. The equilibrium method images the heart and calculates functional parameters when the radionuclide is fully mixed and at equilibrium, when each milliliter of blood contains the same amount of activity and blood pool counts are proportional to volume. Both methods may be gated or acquired in synchrony with the cardiac cycle to gain temporal data regarding the ventricular contraction for each beat. Tables 7.1 and 7.2 list advantages and disadvantages for each method. Aside from differences in attenuation and resolution, the two methods areidentical.

Advantages
Records and analyzes the transit of a radionuclide bolus through the central circulation
Allows imaging and the physiologic interrogation of individual chambers relatively free of adjacent chamber activity and virtually free of atrial activity
Records real-time events, which allow the characterization and quantification of individual cardiac beats
Allows short acquisition times of approximately 30 seconds at rest and 10–15 seconds at peak exercise. High-quality images can be acquired using a state-of-the-art, high-sensitivity device and, at best, a multicrystal camera. This brief acquisition time is optimal for the study of rapidly changing physiologic states.
Uses most radionuclides appropriate for a conventional gamma camera that can be safely injected intravenously in a sufficient dosage for adequate counting statistics. Macroaggregated albumin sequestered in the lungs is not appropriate, as it fails to pass the capillary network.
Can be used in combination with other imaging techniques to enhance diagnostic information
Disadvantages
Can only be used with conventional Anger cameras if they can deliver count rates of 150,000–200,000 counts per second. Many current state-of-the-art cameras are capable of this. Among other factors, the accuracy of the method varies with the statistics of the study. The greater the count density in the end-diastolic region of interest, the lower the statistical error in the calculation of ejection fraction. Much higher count density is required in patients with abnormal ventricular function than in patients with normal function to derive similar statistical reliability. The statistics applicable to the typical first-pass study result in an approximately 3% error in left ventricular ejection fraction (LVEF) calculation
Each measurement requires a separate injection, which limits the number of studies that can be acquired. Serial injections of ^{99m}Tc result in a buildup of background activity.
Study quality depends on the discreteness of the injection bolus. Up to 10% of studies will be compromised by delayed or fractionated boluses.
Patient motion or arrhythmia more easily compromises results than in an equilibrium study.
Planar methods cannot avoid structural overlap; it is difficult to separate ventricles (especially the right ventricle) from the atria (especially the right atrium).

Table 7.1 Advantages and Disadvantages of the First-Pass Method

Advantages
Presents high-resolution images
Provides excellent assessment of regional wall motion and cardiac structures, with an intraobserver variability of ±3% and an interobserver variability of ±4%
Can be fully automated to yield an objective, accurate, and reproducible left and right ventricular ejection fraction
Can be easily performed with standard, state-of-the-art, single-crystal scintillation cameras
Can be applied reproducibly for repetitive calculations with interventions
Is ideally suited for generation of functional images
Disadvantages
Must use labeled red cells
Cannot be used with any ^{99m}Tc-labeled radionuclide passing through the blood pool
Requires 2–33 minutes of acquisition time to gain adequate data with conventional, single-crystal cameras, but about 1 minute using new, high-sensitivity digital cameras
Risks loss of accuracy or "blurring" of data when applied with brief intervention
Planar methods cannot avoid structural overlap; it is difficult to separate the ventricles (especially the right ventricle) from the atria (especially the right atrium).

Table 7.2 Advantages and Disadvantages of the Equilibrium Method

The most commonly used tracer is ^{99m}Tc-labeled red blood cells. Commercially available kits are available that can easily produce this tracer [23]. Equilibrium gated blood pool imaging, as conventionally performed, is called *equilibrium radionuclide angiography*. For PET, it is possible (but not common) to also do blood pool imaging using ^{11}C-labeled carbon monoxide. This gas is breathed by the patient a few minutes before imaging begins. The quantity of ^{11}C carbon monoxide that must be inhaled is typically no greater than one might breathe in heavy traffic, so there are no deleterious physiologic effects. Both PET and SPECT blood pool imaging can give valuable three-dimensional measures, visual and quantitative, of ventricular function. SPECT blood pool imaging is of course more widely used.

First-Pass Analysis

Figure 7.2 illustrates a first-pass curve of time versus radioactivity. Such data can be generated and accurately processed with as little as 1–2 mCi of any agent that stays in the blood pool for the first circulation, but images are not available with this dose. Alternatively, volumes may be calculated from ventricular outlines using geometric considerations. A unique first-pass method of volume calculation is applied with the multicrystal camera, where image counts are sampled in a known blood volume at the attenuation distance to the mid-left ventricle and used to standardize ventricular counts during diastole and systole [24, 25].

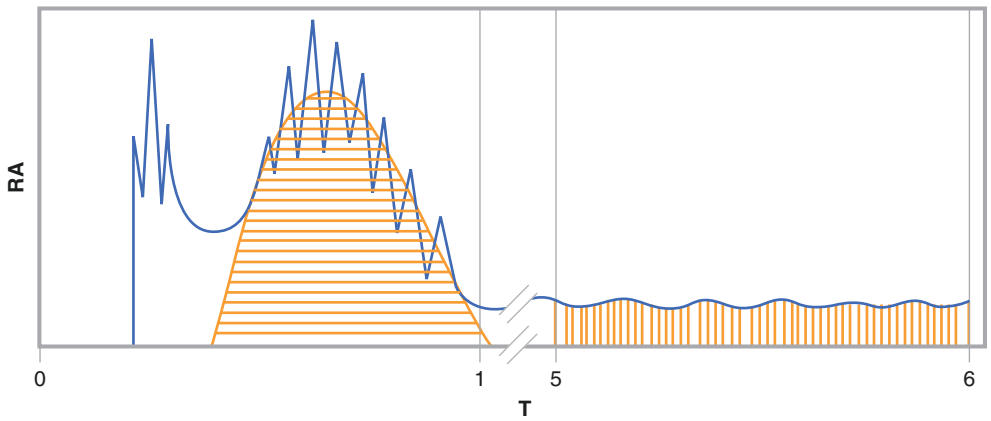

Fig. 7.2 First-pass curve analysis. Shown is a diagrammatic sketch of a first-pass time (T) in seconds versus radioactivity (RA) curve. The area under the left ventricular component (*horizontal lines*) is proportional to cardiac output and is calibrated for volume by dividing it into the integrated area under 1 minute of the equilibrium time versus the RA curve (*vertical lines*) acquired when the radiotracer is thoroughly mixed in the blood [25]

Figure 7.3 shows a first-pass analysis of the levophase, in which a region of interest is drawn on the levophase of the first-pass ventriculogram and the diastolic peaks and systolic valleys are compared to calculate the left ventricular ejection fraction (LVEF).

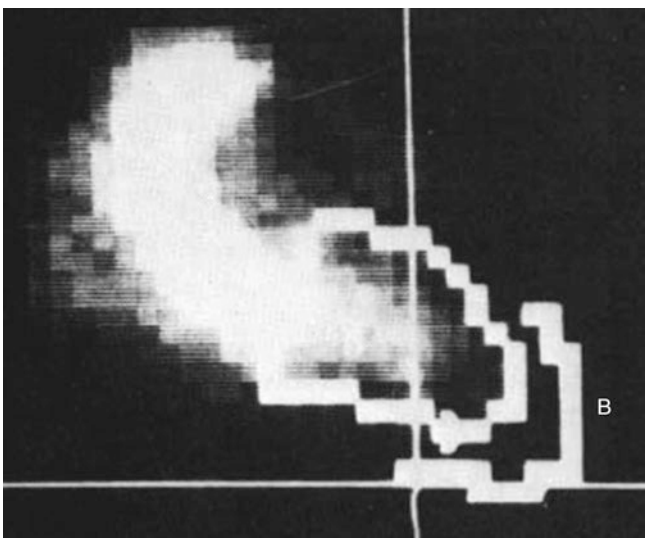

Fig. 7.3 First-pass analysis of the levophase. An irregular region of interest is drawn on the levophase of the first-pass ventriculogram. Correcting for background activity (B), the diastolic peaks and systolic valleys are compared to calculate the left ventricular ejection fraction (LVEF) [25]

First-pass imaging presents an alternative method of blood pool imaging while injecting the tracer as a bolus [6, 26–28]. Nearly all the considerations for standard gating, list mode, and phase mode can be applied to this first-pass methodology. The tracer can be a blood pool agent or almost any other imaging agent, such as Tc-MIBI (isonitrile), ^{201}Tl, Tc-tetrofosmin, or even ^{99m}Tc-pertechnetate. Regardless of the tracer's chemical form, during its first transit through the heart, most tracers stay in the arterial blood for seconds to minutes before they are taken up by the myocardium or other tissues. During that brief transit time, the tracer behaves as though it were a blood pool tracer. In an equilibrium gated study, the activity in the left ventricle (LV) is diluted by a factor of about 5000 because the tracer has been mixed with the entire volume of blood in the body, but when the tracer is injected as a bolus, the concentration of activity in the ventricular chambers is quite large during the tracer's first transit through the heart. This yields count rates that are many times higher than in equilibrium radionuclide angiography studies. Despite this much higher count rate, it is still necessary to do some form of gating in order to capture the ejection fraction. For first-pass studies, only a few beats of data need to be added together. One of the advantages of first-pass imaging is that, it can be performed with nearly any imaging agent, so one can obtain LV function data from studies done for some other purpose, such as bone scans. In addition, it is possible to position the gamma camera in a right anterior oblique view and obtain early gated images during the passage of the radioisotope through the right ventricle (RV), prior to contamination by counts from the LV. One of the disadvantages of the first transit is that one usually must obtain all the LV function information from only a small number of beats (Fig. 7.4). This means that a rapid bolus injection must be given, resulting in very high count rates during the passage of the tracer through the cardiac chambers. Such high count rates often cause unacceptable dead time in many cameras. Therefore, specialized cameras (often not using the Anger methodology) have been developed specifically for dealing with these high count rates. However, many standard cameras can perform first-pass acquisition with adequate accuracy, although the dose may need to be limited. Additionally, because the calculation of the ejection fraction is based on a few samples, it is prone to greater variability. The few samples are related to the required tight RV bolus passage.

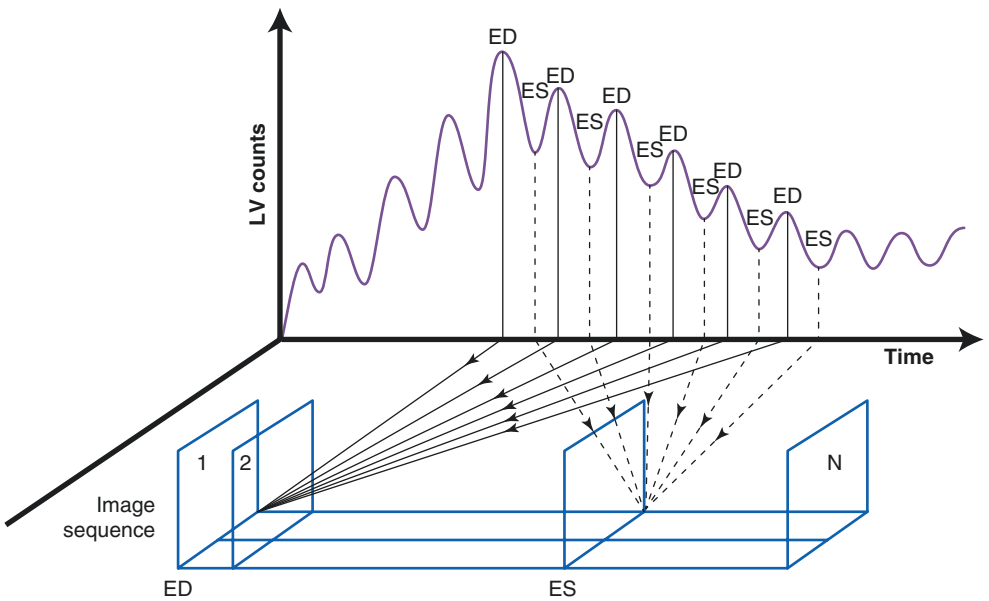

Fig. 7.4 Gated first-pass blood pool imaging. When the tracer is injected as a bolus, the concentration of activity in the ventricular chambers is quite large during the tracer's first transit through the heart. Despite this much higher count rate, it is still necessary to do some form of gating in order to capture the ejection fraction (EF). For first-pass studies, only a few beats of data need be added together. This figure illustrates the case of "gating" the first six beats of data to produce one sequence of *N* images. One of the disadvantages of the first transit is that one usually must obtain all the LV function information from only a small number of beats. Because the EF is calculated from the average values based on the magnitude of the peak counts, proportional to end-diastolic (ED) volume, and the valleys, proportional to end-systolic (ES) volume, correcting for background activity, and is based on a few samples, it is prone to greater variability [29]

Figures 7.5, 7.6, 7.7, and 7.8 present examples of the use of first-pass analysis in patients to obtain information about cardiac function.

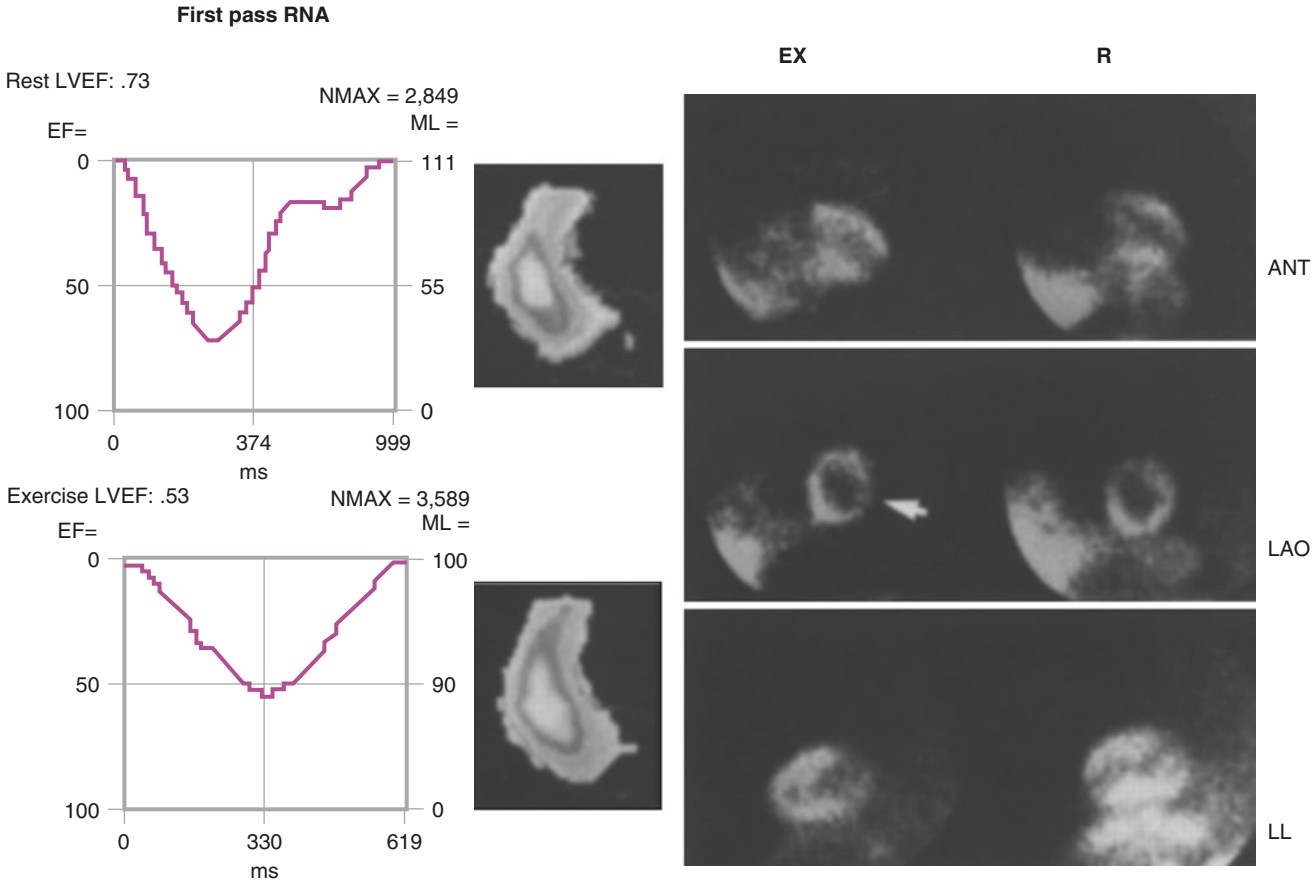

Fig. 7.5 Interaction of perfusion and function. This figure demonstrates the perfusion-function interaction [30]. Shown at the *right* are perfusion images in anterior (ANT) (*top*), left anterior oblique (LAO) 40° (*center*), and 70° (*bottom*) with exercise (EX) and at rest (R) in each image pair acquired in a 41-year-old man with a history of coronary disease, prior coronary bypass graft surgery, and atypical chest pain. On the *left* are the associated first-pass radionuclide angiography (RNA) images of the sestamibi bolus administered to evaluate LV function at rest and with exercise. Evident is a reversible inferolateral defect, cavitary dilatation, and reduced LVEF with exercise [30]

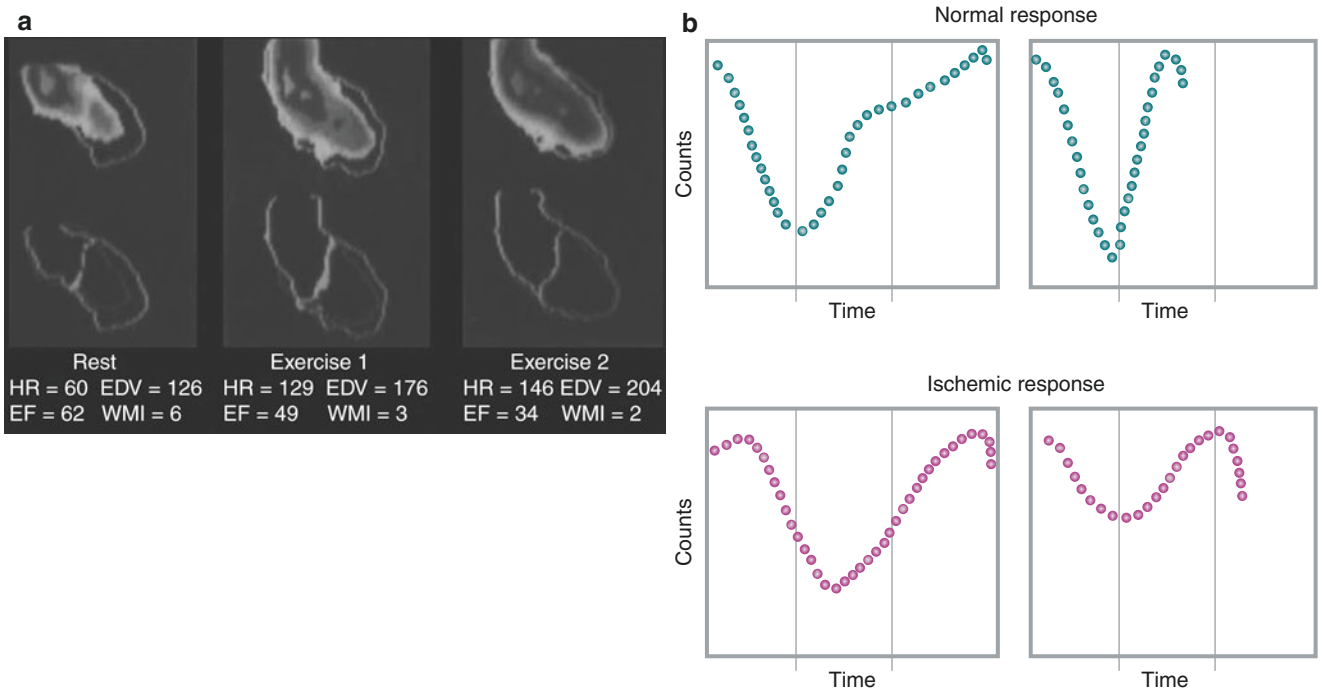

Fig. 7.6 Abnormal first-pass exercise study. (**a**) Examples of baseline (*left*), early exercise (*center*), and peak exercise (*right*) LV function in a patient with coronary disease [31]. In each panel, the end-systolic frame is related to the end-diastolic outline (*top*), while both end-diastolic and end-systolic outlines are presented below. Data presented for each period include the heart rate (HR), left ventricular ejection fraction (EF), end-diastolic volume (EDV), and wall motion index (WMI). The ischemic response is characterized (as it is with all methods that evaluate the functional response) by increased EDV and reduced WMI and EF. (From Upton et al. [31], with permission.) (**b**) Typical time versus radioactivity curves related to the normal (*top*) and ischemic (*bottom*) exercise response. In each case, the baseline curve is at the *left* and the exercise-related curve is at the *right*

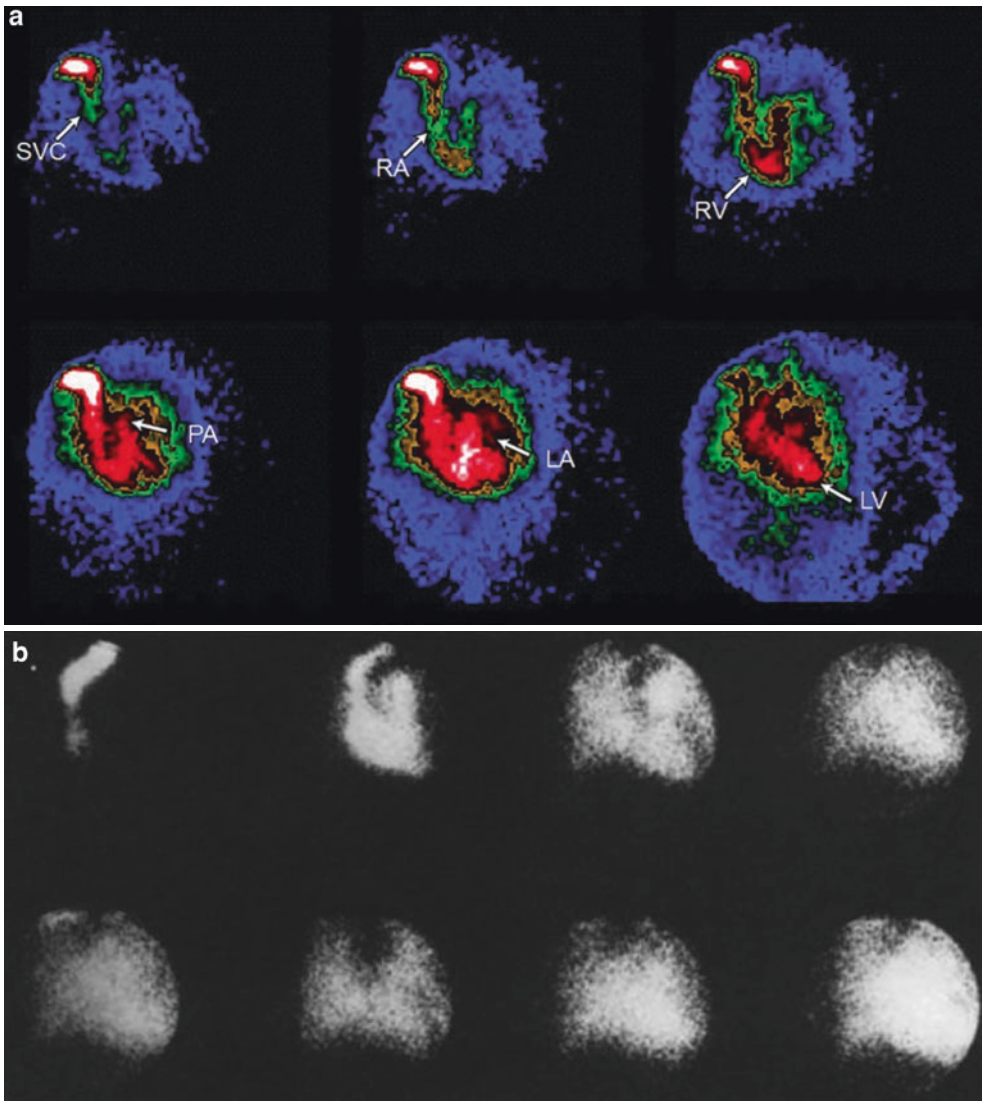

Fig. 7.7 First-pass images in a normal patient and in a patient with a left-to-right shunt. (**a**) First-pass radionuclide ventriculography. Individual frames from a first-pass acquisition illustrate the path of the bolus isotope through the superior vena cava (SVC), the right atrium (RA), the right ventricle (RV), the pulmonary outflow tract and lungs (pulmonary artery [PA]), the left atrium (LA), and the left ventricular (LV) phase, from which the isotope bolus is then distributed systemically. (From Udelson et al. [32], with permission.) (**b**) Similar images taken in a patient with a significant left-to-right shunt. The lungs were never clear, because of continued recirculation of the bolus. As a result, the LV teardrop and the levophase are not seen. This "smudge sign" generally relates to a left-to-right shunt with $Q_p/Q_s \geq 1.5$

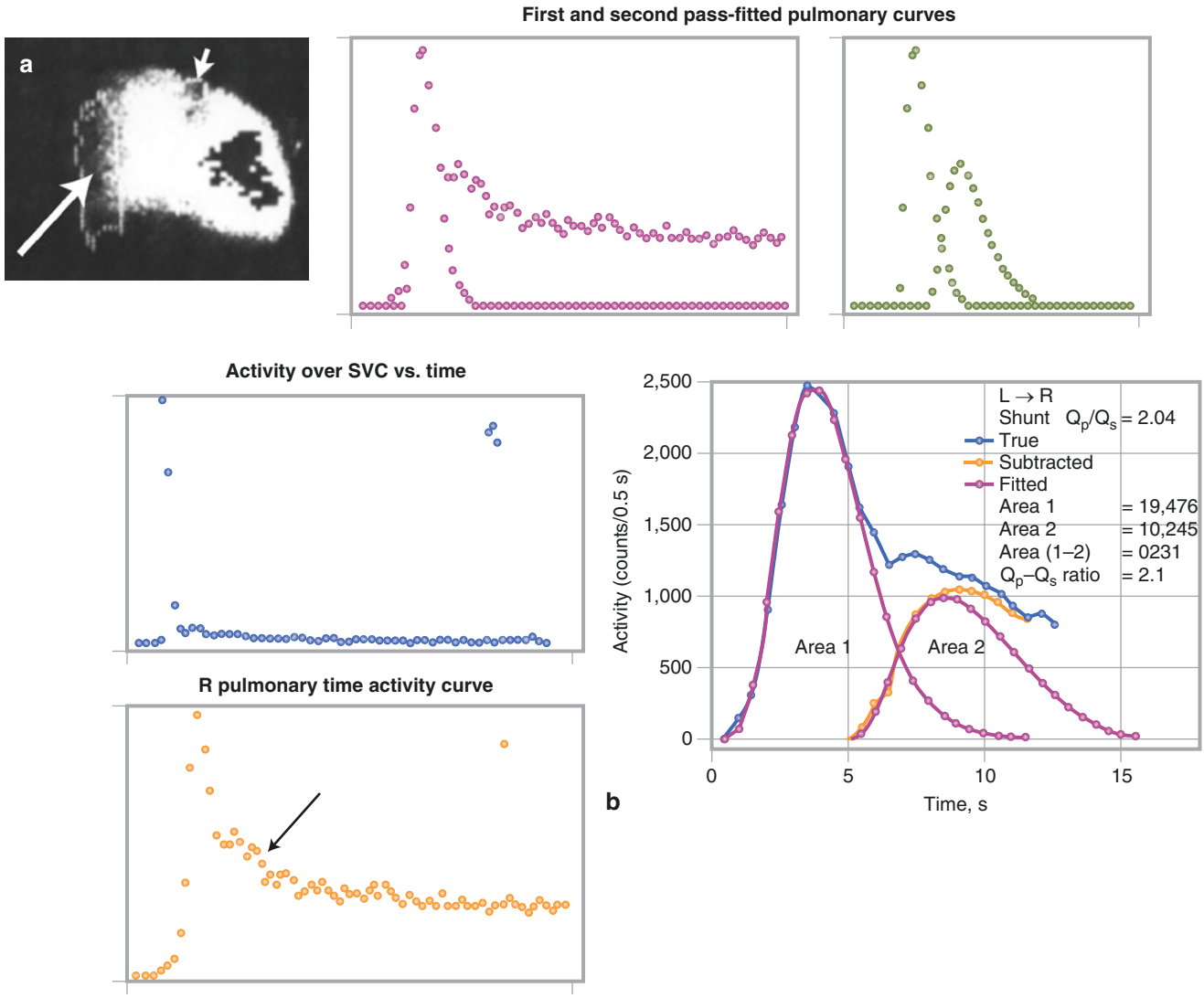

Fig. 7.8 Calculation of Q_p/Q_s. (**a**) A calculation of the left-to-right shunt magnitude in a patient with an atrial septal defect is shown according to the method of Maltz and Treves [34]. At the *upper left* is a summed view of all frames of a first-pass study performed over the central circulation. Regions of interest are taken over the superior vena cava (SVC, *short arrow*) to check on the integrity of the bolus, which must be both rapid and coherent in its delivery, and the right lung (*long arrow*), seeking recirculation via shunting. At the *upper right* are the time–activity curves generated from these regions of interest. The SVC curve confirms the rapid passage of an excellent bolus injection. The "hump" on the lung curve downslope represents the shunt recirculation through the lungs. In the *lower left*, a gamma-variate curve fits the first lung passage. At the *lower right*, the gamma-variate fitting to both the first and the second passages is shown. (**b**) The curve analysis. By principles of "dye dilution" analysis, the area under the first fitted curve, Area 1, is proportionate to systemic flow, while the area under the second passage curve, Area 2, is proportional to the shunt flow. As shown diagrammatically in this figure, Area 1 = Q_p (pulmonic) and Area 2 = Q_{sh} (shunt). Thus, Q_s (systemic) = $Q_p - Q_{sh}$ and $Q_p/Q_s = Q_p$ (Area 1)/Q_p (Area 1) − Q_{sh} (Area 2). The method is not a diagnostic tool but one meant for an accurate quantitation of such shunts between Q_p/Q_s of 1.2–3 and so is useful in prognosis and management. It is another scintigraphic method that is underutilized owing to the widespread availability and capabilities of echo Doppler examination [34]

Equilibrium Analysis

One can measure the mechanical contraction and relaxation of the heart chambers either with blood pool imaging or by labeling the walls of the myocardium. In both cases, the goal is to capture images of the blood pool (or myocardium) as the heart contracts and relaxes, that is, through systole and diastole [35]. For the measurement of myocardial function by observing the motion of the myocardial walls, any agent that remains in the walls for many minutes can be used. For blood pool imaging [20], a blood pool agent, typically labeled red blood cells, is injected and then allowed to mix with the 5–6 L of blood in a typical subject. After 3 or 4 minutes of mixing, the tracer will be uniformly distributed and the tracer is then said to be "in equilibrium." If a single heartbeat were 960 ms long (i.e., a heart rate of about 63 beats/min), we could divide up that single beat into, for example, 16 images, each 60 ms long. The first image would be acquired for 60 ms; then the second would acquire all the data in the next 60 ms, and so forth. Each image would reflect a different portion of the cardiac cycle, from end diastole through systole and back again. Unfortunately, an acquisition that was only 60 ms long would have too few counts to make an interpretable image. With the typical activities injected in a patient (10–30 mCi or 370–1110 MBq for either blood pool or myocardial imaging), one would need to acquire each image many hundreds of times longer, perhaps for 10–20 seconds or longer. To solve this problem, we use the technique of electrocardiographic (ECG) gating (Fig. 7.9). The total acquisition time of each image is not determined directly by the imaging time, but rather by the number of beats multiplied by the duration of each frame. At high heart rates, this time builds up more quickly than at low heart rates for the same image duration. Many commercial computer systems actually do a slightly more sophisticated form of data acquisition. These methods permit "beat length windowing" [5, 35, 36]. That is, data from a particular beat is added to the gated image set only if that beat is between a preselected minimum and maximum length. The user usually has to decide in advance which beat lengths to include or reject, which is sometimes problematic if the heart rate changes during the study. There are some problems with this technology. If, for example, a cardiac cycle is terminated prematurely by a premature ventricular contraction, then it could be rejected. However, the following cardiac cycle will not begin its contraction with a fully dilated left ventricular cavity; that is, it will not have filled completely, so it is the data from this subsequent cardiac cycle that should be rejected. This is problematic with some of the available beat length windowing schemes available commercially; a solution to this problem is outlined below.

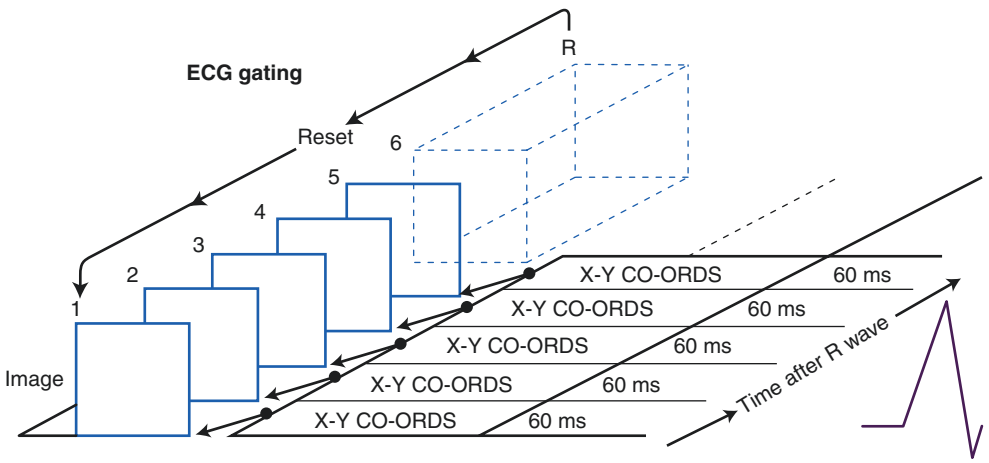

Fig. 7.9 Electrocardiographic (ECG) gating of equilibrium radionuclide angiography (ERNA). An ECG is connected to the patient and its output is put through a "trigger" device that generates a "gating" signal at each R wave peak, for example. If a single heartbeat were 960 ms long (i.e., a heart rate of about 63 beats/min), we could divide up that single beat into 16 images, each 60 ms long. Because an acquisition that was only 60 ms long would have too few counts to make an interpretable image, we use the technique of ECG gating. An ECG is connected to the patient and its output is put through a "trigger" device that generates a "gating" signal at each R wave peak, for example. For the first 60 ms after the first R wave, all the photons are sorted into the first image. After 60 ms has elapsed, all data are then sorted into the second image, and so on. Finally, at the next R wave, signifying the beginning of the next cardiac cycle, the process is repeated, and the next 60 ms of data are again added to the first image (Image 1 in the figure) and similarly for all the subsequent images. If this process continues for 300 beats, then each image is acquired for (60 ms/beat) × 300 beats = 18 seconds

Figure 7.10 illustrates the technical aspect of equilibrium radionuclide angiography (ERNA) acquisition from another viewpoint. Before acquisition, the computer monitors the R–R interval to establish the heart rate, and the mean rate is divided by the number of frames per cycle, based on the computer's memory and the software applied in frame mode acquisition. The individual frames from each beat are pooled with the same frame of subsequent beats until adequate count data are acquired, as exemplified by Fig. 7.11. Summed frames representing the total data in all image intervals are displayed as an endless loop movie and computer analyzed for the LVEF, RVEF, and ventricular size and function. Heart rate variability alters the data content of each frame and greatly distorts the data at the end of the curve [36].

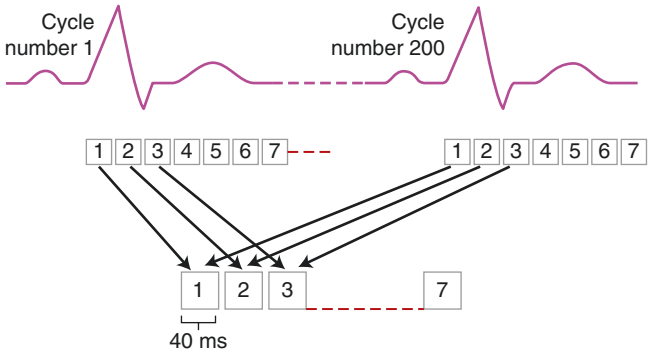

Fig. 7.10 ECG gating of equilibrium radionuclide angiography (ERNA), from another viewpoint. Before acquisition, the computer monitors the R–R interval (*top*) of multiple cardiac cycles, here 1–200. The heart rate is established and the mean rate is divided by the number of frames per cycle, based on the computer's memory and the software applied in frame mode acquisition. With a heart rate of 60 beats/min, the R–R interval is 1000 ms, and at 25 frames/cycle, the frame duration is 40 ms, a typical interval. These individual frames from each beat are pooled with the same frame of subsequent beats (*middle row*) until adequate count data are acquired in a master composite frame (*lower row*). Summed frames representing the total data in all image intervals are displayed as an endless loop movie and computer analyzed for the LVEF, RVEF, and ventricular size and function, considering that each milliliter of blood contains the same radioactivity [36]

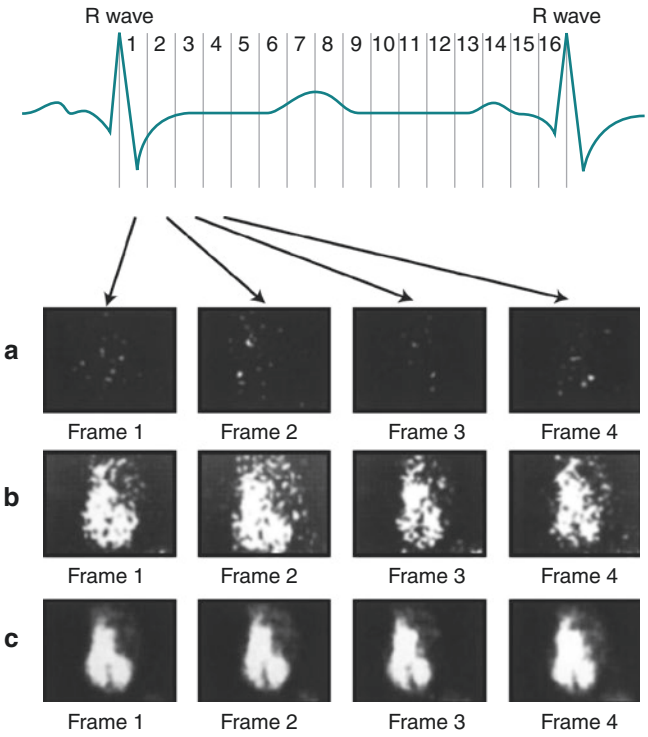

Fig. 7.11 Computer acquisition of the equilibrium study. Shown is the relationship between the cardiac cycle or R–R interval acquired over 16 separate frames or intervals and the related images in each frame over the course of the acquisition [37]. The counts acquired during frame 2 are stored in frame 2, those acquired during frame 3 are stored in frame 3, and so on. Only data accumulated over the first four frames are illustrated here. Owing to the low count rate in this study, 750 counts/frame, there is little to see after acquisition over a single cycle (**a**). However, after the accumulation and addition of the counts from 20 R–R cycles, now with 15,000 counts per frame, the cardiac chambers are taking form (**b**). With the addition of counts acquired over 400 cycles and 300,000 counts/frame, image quality is excellent and the acquisition is over (**c**) [37]

Gating Methods

Figure 7.12 illustrates a typical planar gated blood pool sequence of images that are made up of about 300 cardiac cycles "gated" together. These images can be played as a cine that will reveal the pattern of contraction. Wall motion defects can clearly be observed from such movie sequences, but because these are planar images taken from a left anterior oblique (LAO) position, the effects of motion of the anterior and posterior myocardial walls will be difficult to observe. For resting studies, two additional views are also usually acquired, an anterior view and a left lateral view. These other two views give additional visual information concerning wall motion. Only the LAO view is used to compute quantitative indices of LV function, because only this view is free from overlapping structures, albeit incompletely. The same technique can be used with gated blood pool SPECT, but in this case, there is access to all views and cross sections, so that all walls can be observed and there is no difficulty with overlapping structures [11, 12, 14, 16, 18, 38, 39].

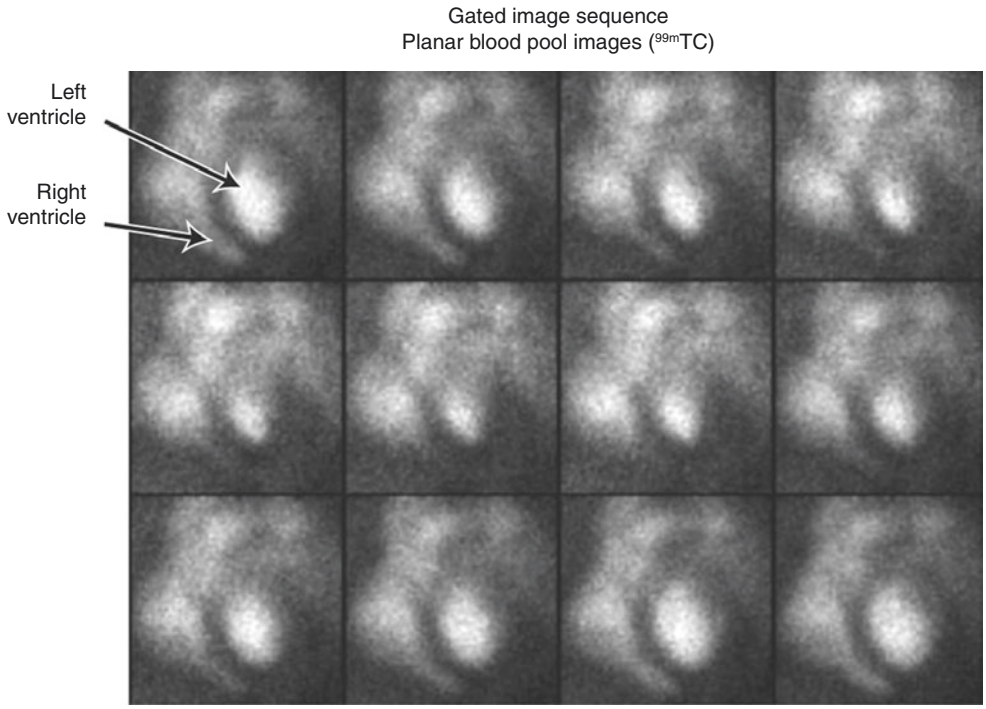

Fig. 7.12 Gated imaging sequence. This typical planar gated blood pool sequence of 12 images is made up of about 300 cardiac cycles "gated" together, as described in the previous figure. The images were taken with ^{99m}Tc-labeled red blood cells. The gamma camera was positioned in a left anterior oblique (LAO) position, approximately 45°, with a 15° caudal tilt. The caudal tilt is used to better separate the left ventricle (LV) from the left atrium. The *top left panel* shows the first image in the gated sequence triggered by the electrocardiographic R wave, at the end diastole. The LV is at the right and the right ventricle (RV) can be seen to the left (*arrow*). Each image (*left to right*, *top row to bottom*) represents an additional 60-ms elapsed time from the R wave. By about the fifth or sixth image (300–360 ms), it is clear that the LV has contracted considerably, reaching end systole. The RV is also much smaller, its apical portion almost disappearing. During the next six images, the LV begins filling in the diastolic portion of the cardiac cycle. By the 12th image, the LV is once again completely full (end diastole), and the cycle begins again. Because there are 12 images of 60 ms each, the average time between beats (the R–R time) is 60 ms × 12 = 720 ms. This corresponds to a heart rate of about 83 beats/min. These images can be played as a cine that will reveal the pattern of contraction and clearly show wall motion defects, but because these are planar images, the effects of motion of the anterior and posterior myocardial walls will be difficult to observe. In this LAO view (with caudal tilt), only the motion of the septal, apical, and lateral LV walls can be observed

Because the image intensity or counts in the gated image sequence are approximately proportional to the volume of blood (or exactly, in the case of PET), one can create an LV volume curve from the image set and draw a single region of interest (ROI) around the image. In Fig. 7.13, the planar gated image set produced an LV "volume" curve with very high temporal resolution. The word *volume* is in quotes because, in planar studies, the counts are only approximately proportional to volume as a quite linear function and because some of the counts in the planar images arise from the tissues above and below the heart, such as the soft tissue between the gamma camera and the heart. In an attempt to correct for these extraneous counts, one usually draws a second ROI adjacent to the LV cavity and takes this "background" region as a correction indicative of the extraneous counts from above and below the heart [9]. Another method uses not a single region over the LV cavity, but instead a different ROI for each image or frame. This method has the advantage of better tracking of the LV cavity and the disadvantage of introducing variability in drawing the numerous regions required. In actual practice, both methods give results that correlate quite accurately with one another, although the variable region method gives a consistently "deeper" curve and a higher ejection fraction. Practically, images for each frame are used when edges for each ROI can be applied in an automated manner. When edges must be applied manually, regions are drawn on end diastole and end systole. This procedure is semiautomated in many commercial nuclear medicine cardiac analysis packages. It has been shown that 16 frames or more are needed to provide the sampling rate required to capture the extremes of end systole and end diastole in order to gain an accurate ejection fraction and other indices of LV function [40].

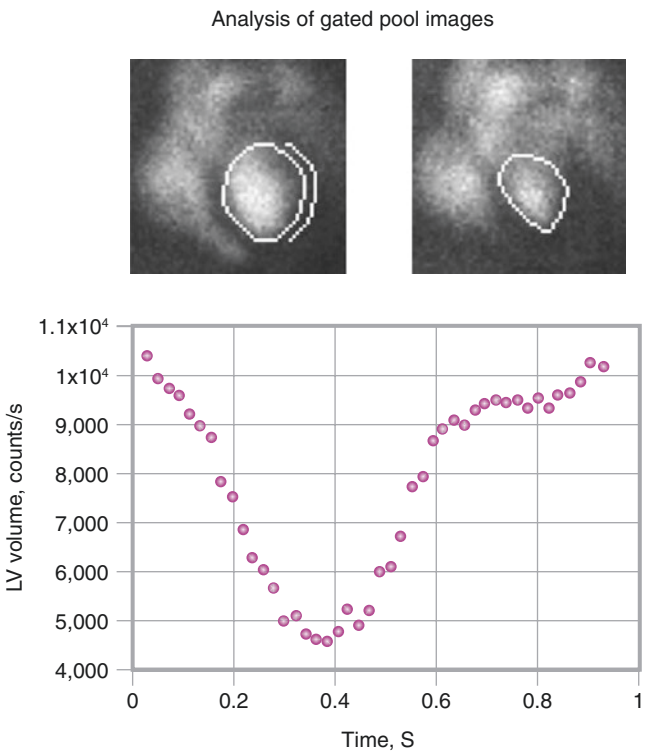

Fig. 7.13 Analysis of gated blood pool images. An LV volume curve can be drawn from the image set, and one can draw a single region of interest (ROI) around the image at the end diastole, as shown by the roughly circular ROI in the *upper left image*, and then plot the counts from within this ROI as a function of time represented by the image number against the milliseconds per image. In this figure, the planar gated image set consists of 44 images, each taken for 20 ms, thereby producing an LV "volume" curve with very high temporal resolution. The word *volume* is in quotes because, in planar studies, the counts are only approximately proportional to volume as a quite linear function and because some of the counts in the planar images arise from the tissues above and below the heart [41]

The ERNA gating method can be performed in "real time" [7, 35], with the data sorted into the images on the fly as the photons are registered by the gamma camera (often called gated "frame mode" acquisition). This method is very convenient, but sometimes it is less than ideal. For example, one may wish to retrospectively look only at beats of a certain length, which is impossible if the data are sorted into the image sequences on the fly. To enable "retrospective" analysis of the data, one can use a method called *list mode acquisition* (Fig. 7.14). In this mode of operation, the computer simply records on disk a "list" of the timing and location of every photon recorded by the camera. Typically, many millions of counts make up a gated blood pool cardiac study, so a lot of disk storage is required, which was a serious problem for older systems but is no longer an issue. Once the data have been recorded, one can read it back from the disk and perform the gating just as described previously. Why bother to write it to disk? There are several reasons. First, in frame mode, selecting the beat length window (i.e., the range of beats to accept and reject) is often problematic. One must make this decision prior to beginning the acquisition, and it is quite possible, and even common, for the heart rate to change during the course of the study if the patient becomes more comfortable on the table or even falls asleep, or, conversely, becomes uncomfortable. Thus, the heart rate may slowly shift as the study progresses. Similarly, during exercise studies it is often not possible to accurately predict the heart rate and keep it stable. In a list mode study, such difficulties are easily overcome, because one is processing the data after the fact. The computer can first display the progression of heart rates that occurred during the study, and the operator can then select whatever range of heart rates seems most suitable. This method also permits multiple levels of exercise to be studied easily. One can select any combination of heart rates and time periods desired. Finally, list mode acquisition allows the very end of the cycle, atrial contraction, to be reproduced. Again, since processing is retrospective, one can gate "backward" in time from the R wave trigger [34, 35]. If the interval from the P wave to the R wave is relatively constant from beat to beat, one can faithfully reproduce the volume increase due to atrial contraction.

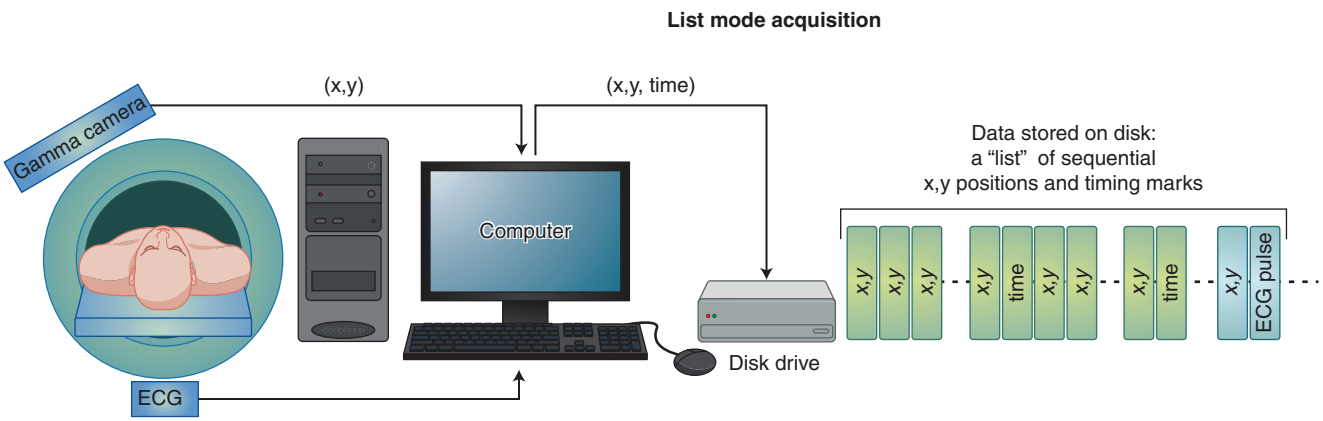

Fig. 7.14 List mode acquisition. This schematic drawing demonstrates the mechanism of list mode acquisition, which permits "retrospective" analysis of the data, which the computer has simply recorded on disk as a "list" of the timing and location of every photon recorded by the camera

The gating process assumes that the heart beats in exactly the same way, with the same contraction and relaxation pattern, from one beat to the next [41]. If the subject is in normal sinus rhythm (NSR), this approximation holds quite well, but owing to the normal sinus arrhythmia, a varying beat length requires an adjustment at the end of the cycle. The end of the cycle must be handled somewhat differently, because not all beats will be of the same length. In fact, fluctuations in the R–R interval times can be quite large, as much as 100 ms or more for a normal subject in NSR at rest. In the usual acquisitions (not list mode), this means that for beats shorter than average, the last frames, or the last few, will not accumulate for the full time, whereas for beats longer than the average, data will be thrown away. Both of these circumstances can easily be accounted for by keeping an accurate account of the actual length of each beat and, therefore, the actual acquisition time for each frame that spans the cardiac cycle. Of course, such beat length fluctuations may degrade the ability of the gated data to portray events occurring very late in the cycle as the volume increases due to atrial contraction. Not all computer systems make the compensation for this varying beat length. If such a correction is not made, the images at the end of the cycle will have an artificially reduced intensity, and quantitative data extracted from these images may be subject to error.

At first, one might think that a beat shorter than average might be a "condensed" version of an average-length beat and that a long beat is simply a uniformly stretched version of a short beat, scaled temporally with a shorter-than-average time to end systole and other characteristics. If this were true, then the assumption that all beats are identical would be violated. Fortunately, for subjects in NSR, it has been shown that at rest, fluctuations in the heart rate are caused primarily by fluctuations in the initiation of the next beat. That is, a "short" beat is shorter only because the next beat begins slightly earlier than average. Thus, at rest in normal individuals, it is only diastasis that is shorter, and the earlier parts of the cycle remain unaltered (Fig. 7.15). This is not true at higher heart rates, where there is no diastasis at all, nor is it necessarily true for subjects who are not in NSR, or for subjects in whom the filling portion of the left ventricular volume curve is so abnormal that there is no discernible diastasis at all. In these situations, the technique of "beat length windowing" is necessary, in which beats shorter or longer than some predetermined length are not included in the data. This technique may not always make physiologic sense, however, as the short beat itself in all likelihood was functioning like all other beats up until the time it was prematurely terminated. That is, it was too short simply because the next beat began too early. If the next beat began prior to complete LV filling, the beat following the short beat would *not* be identical to all the other beats. It would have a different preload and therefore a different pattern of contraction and filling. Therefore, one may wish to reject the beat following the short beat, not just the short beat itself. In fact, there may be no reason to reject the short beat. The user of the computer program for gated acquisition is usually permitted to choose not only what length beats are unsuitable but also what to do about the succeeding or preceding beats.

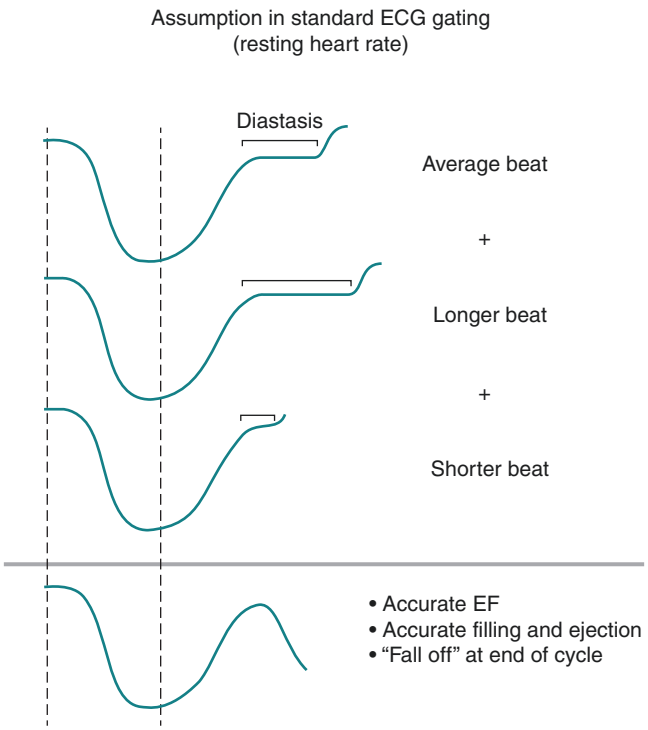

Fig. 7.15 Assumptions in standard ECG gated imaging. For subjects in normal sinus rhythm (NSR), it has been shown that at rest, fluctuations in the heart rate are caused primarily by fluctuations in the initiation of the next beat. That is, a "short" beat is shorter only because the next beat begins slightly earlier than average; it is only diastasis that is shorter, and the earlier parts of the cycle remain unaltered. EF—ejection fraction

Clinical Parameters

Figure 7.16 demonstrates the useful clinical parameters that can be extracted from the LV volume curve [35, 36]. The most useful measure is ejection fraction; others include the peak ejection rate (PER), the maximum rate at which blood is ejected by the heart; the time to end systole (TES); and the peak filling rate (PFR), the diastolic correlate of the PER. In many diseases, impending impairment of systolic function is preceded by filling that is slower and later than normal, probably due to poor ventricular compliance. Therefore, PFR, a measure of diastolic ventricular function, is often reduced even before the ejection fraction or systolic function is noticeably impaired. Figure 7.17 illustrates the application of these indices in a patient with coronary artery disease. Figure 7.18 demonstrates the effect that drugs such as verapamil can have on the filling rate.

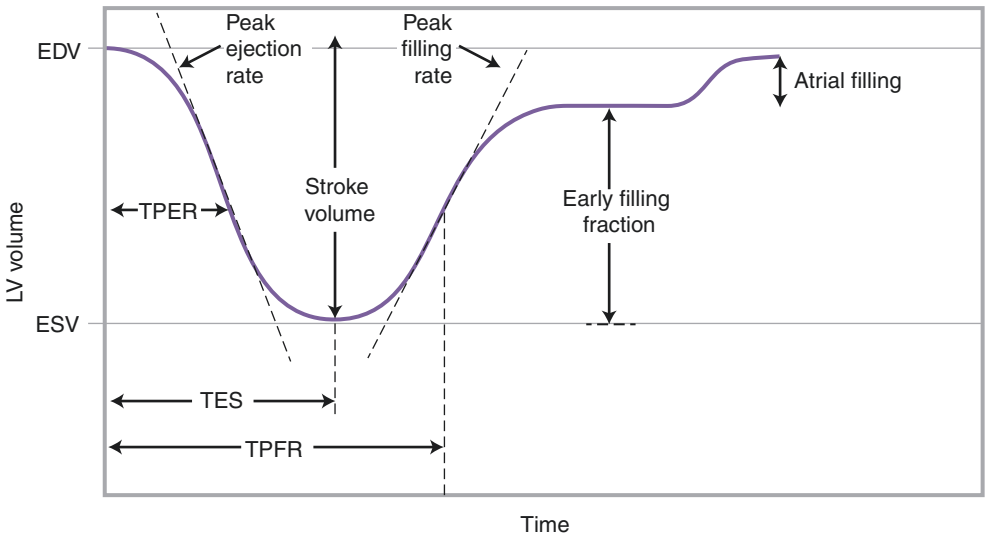

Fig. 7.16 Functional measures. The most useful measure that can be extracted from the LV volume curve is ejection fraction, which is defined as stroke volume/end-diastolic volume (EDV) = ED counts − end-systolic (ES) counts/ED counts, where the counts are assumed to have been corrected for background. Note that although the proportionality factor between "counts" and volume is in general unknown, it does not matter, because this factor will cancel out when the ratio defining ejection fraction is computed. Other parameters that can be extracted from this curve are the peak ejection rate (PER) and its time of occurrence (TPER), usually defined as the maximum negative slope of the LV curve between ED and ES. It characterizes the maximum rate at which blood is ejected by the heart. The time to end systole (TES) is, of course, defined by the minimum of the LV curve. The peak filling rate (PFR) is the diastolic correlate of the PER. ESV end-systolic volume, TPFR time to peak filling rate

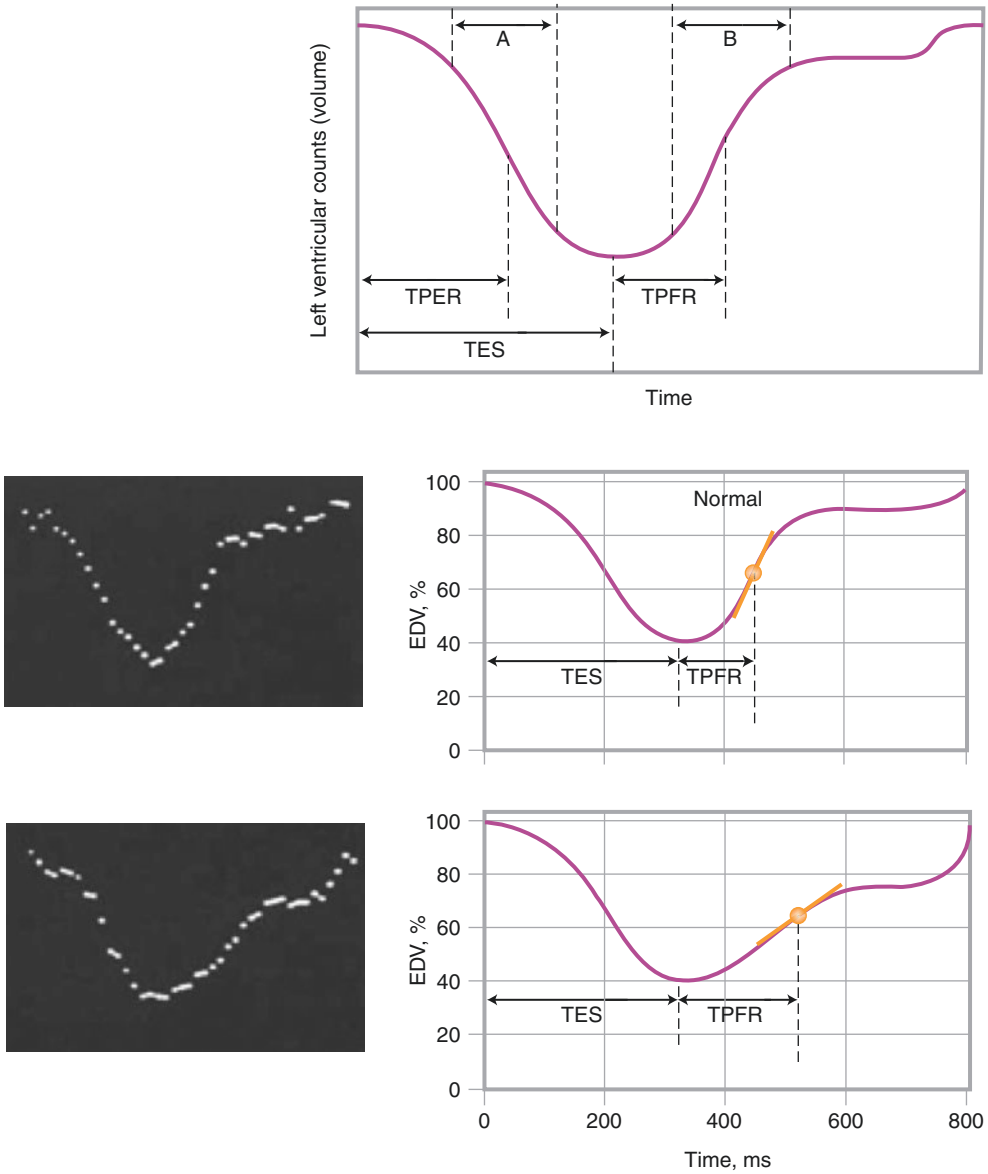

Fig. 7.17 Application of filling phase indices. Shown at the *top* is a diagrammatic left ventricular time-versus-radioactivity curve where the time to peak emptying rate (TPER), time to peak filling rate (TPFR), and time to end systole (TES) are shown in systolic (**a**) and diastolic (**b**) periods [42]. At the *bottom*, actual curves (*left*) and diagrammatic representations (*right*) are shown in a normal patient (*top*) and in a patient with coronary artery disease (CAD, *bottom*). The reduced ventricular filling rate in the latter is evident [42]. EDV end-diastolic volume

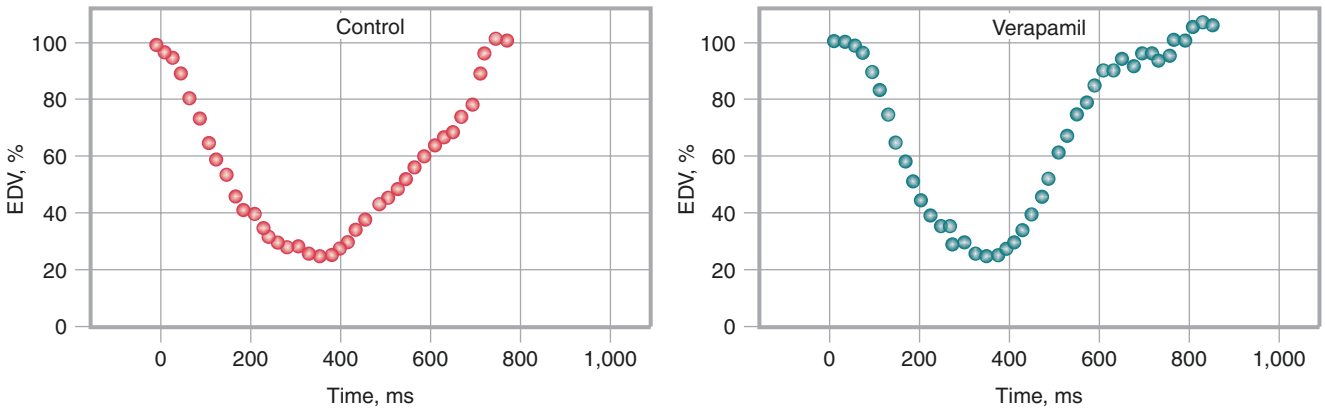

Fig. 7.18 Drug effect on filling rate. Shown is the effect of verapamil on left ventricular compliance and the filling rate in a patient with left ventricular hypertrophy. The slope and the filling rate measured in EDV per second are significantly increased with verapamil [42]

The importance of background in equilibrium blood pool studies is shown in Fig. 7.19 and Table 7.3, which lists the calculations and LVEFs derived from the varying background values shown in the figure.

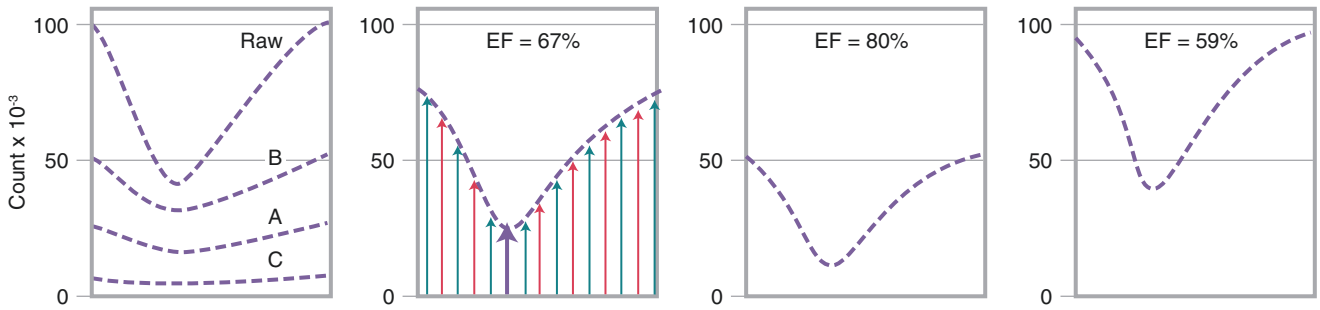

Fig. 7.19 Importance of background in equilibrium blood pool studies. Shown are three model time-versus-radioactivity curves, *A*, *B*, and *C*, which vary only in their background, the greatest in *B* and the least in *C*, as shown in the *left panel* with corresponding background-subtracted curves *A*, *B*, and *C*. The calculations and actual left ventricular ejection fractions (LVEFs) derived from these varying background values are shown in Table 7.3 [43]

Curve	LV ROI pixels	Mean count background ROI	ROI uncorrected counts	Background-corrected counts	LVEF
A	ED 500	50	100,000	75,000	67%
	ES 300		40,000	25,000	
B	ED 500	100	100,000	50,000	80%
	ES 300		40,000	10,000	
C	ED 500	10	100,000	95,000	59%
	ES 300		40,000	37,000	

ED end-diastolic, *ES* end-systolic, *LVEF* left ventricular ejection fraction, *ROI* region of interest

Table 7.3 Importance of background in equilibrium blood pool studies

The absolute LV volume can be calculated with relatively high precision from ERNAs (as well as from first-pass studies), with correction for duration of data collection (i.e., number of beats collected and frame duration), administered dose, and plasma volume. Figure 7.20 shows one method for calculating left ventricular end-diastolic volume, with the validating data comparing volumes obtained by ERNA and contrast angiography at catheterization.

a

Calculation method
$LVEDV = \frac{\text{Count rate from LV in ED frame}/e^{-Ud}}{\text{Count rate/mL from blood sample}}$
where e^{-ud} = attenuation correction
u = average linear attenuation coefficient
d = depth of the center of the LV from the chest wall
LV count rate from ED frame = $\frac{\text{Total LV counts in ED frame}}{\text{Time per frame x number of cycles acquired}}$
Blood sample of known volume is withdrawn into a small test tube and counted under the same radiation detector (camera) used for radionuclide angiography. The calculated count rate is corrected for decay from the time it was withdrawn during the study to the time it was counted.

b

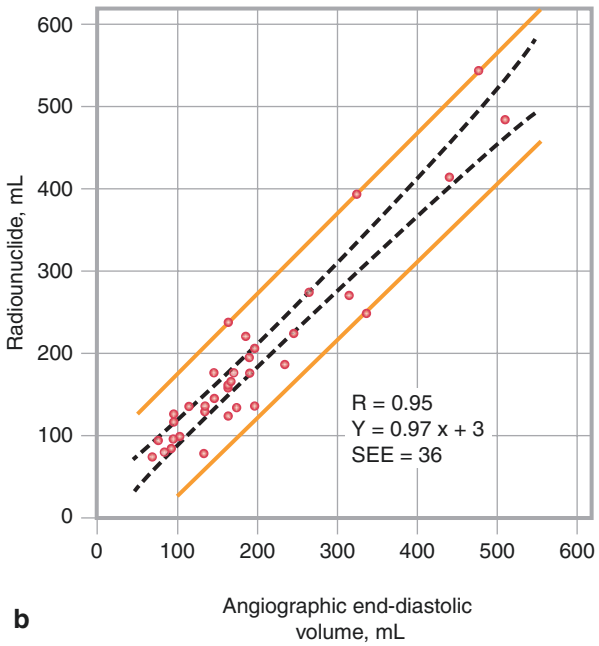

Fig. 7.20 Calculation of left ventricular end-diastolic volume from ERNAs, including correction for duration of data collection (i.e., number of beats collected and frame duration), administered dose, and plasma volume. (**a**) One of the many calculation methods. (**b**) The validating data comparing volumes obtained by ERNA and by contrast angiography at catheterization. ED end-diastolic, LVEDV left ventricular end-diastolic volume, SEE standard error of the estimate

Radionuclide Angiography in Clinical Cardiology

Radionuclide angiography (RNA) can be employed for diagnosis, prognostication, and evaluation of therapy in a variety of situations, but other modalities may be more appropriately applied in specific clinical settings. Table 7.4 lists the most appropriate situations for the application of RNA; for some patients it is an appropriate primary evaluation method, but for others, better alternatives clearly exist. *Italicized entities* are those for which RNA has the greatest potential applicability in clinical practice.

Useful for patients with
Chronic stable coronary artery disease (CAD)
Diagnosis
Prognostication
Assessment of efficacy of treatment
Regurgitant valvular diseases
Prognostication and timing of valvular surgery
Assessment of effects of treatment
Cardiomyopathy
Determination of functional severity, categorization for treatment selection
Assessment of effects of treatment
Useful only for highly selected applications in patients with
Acute CAD
Assessment of effects of treatment
Cardiomyopathy
Determination of functional severity, categorization for treatment selection
Assessment of effects of treatment
Diagnosis of acute right ventricular infarction
Prognostication
Stenotic valvular diseases
Mitral stenosis may be useful in prognostication

Table 7.4 Radionuclide angiography in clinical cardiology

RNA is the most widely accepted method for serial evaluation of cardiac function in patients undergoing doxorubicin therapy. LVEF is an important and universally accepted index of cardiac function, and overt congestive heart failure (CHF) due to doxorubicin cardiotoxicity is preceded by a progressive fall in LVEF. Serial studies can detect a change in cardiac function over time, and doxorubicin administration can be stopped when a predetermined fall in LVEF is observed. Both the absolute LVEF and the magnitude of fall are important strategic determinants. The guidelines for using serial RNA at rest, during the course of doxorubicin therapy, are standardized and are based upon experience with nearly 1500 patients over a 7-year period (Table 7.5) . A reduction greater than fourfold in the incidence of overt cardiac failure was observed when these guidelines were followed, and if CHF did develop, it was mild and rapidly responsive to medical therapy. A recent study has reestablished the clinical relevance and cost-effectiveness of serial LVEF monitoring with equilibrium RNA for the prevention of congestive heart failure during the course of doxorubicin therapy [15].

Baseline EF	Perform equilibrium RNA	At risk for CHF
Normal (≈50%)	At baseline	≥10% EF fall from baseline to <50%
	At ≈450 mg/m^2	
	At 250–300 mg/m^2	
≥30–<50%	At baseline	≥10% EF fall from baseline or EF <30%
	Prior to each subsequent dose	
<30%	Avoid doxorubicin	

CHF congestive heart failure, EF ejection fraction

Table 7.5 Radionuclide Angiography for the Evaluation of LVEF in Doxorubicin Therapy

Exercise RNA also has been used in patients undergoing treatment with doxorubicin, but patients with malignancies often have generalized debility, fever, anemia, or musculoskeletal problems that preclude exercise testing. Moreover, exercise testing does not appear to provide any additional information when compared with resting RNA. Some caution may be required in interpreting changes in LVEF during the course of chemotherapy, because these values also are affected by several noncardiac conditions such as anemia, fever, and sepsis. Resting RNA continues to be the most practical and effective way of monitoring doxorubicin cardiotoxicity. In some studies, diastolic dysfunction with a reduction in peak filling rate appears to precede the decrement in LVEF, as the earliest indication of chemotherapy cardiotoxicity [44]. Another study found that diastolic function adds little to LVEF [45]. The generation of measures of diastolic function is technically demanding; its reproducibility and accuracy are less than those of the calculation of LVEF [45].

Figures 7.21, 7.22, 7.23, 7.24, 7.25, 7.26, 7.27, 7.28, 7.29, 7.30, 7.31, 7.32, 7.33, 7.34, 7.35, 7.36, 7.37, and 7.38 demonstrate other appropriate applications for RNA, including the assessment of regurgitant valvular diseases, conduction abnormalities, and the application of pacing devices and cardiac resynchronization therapy.

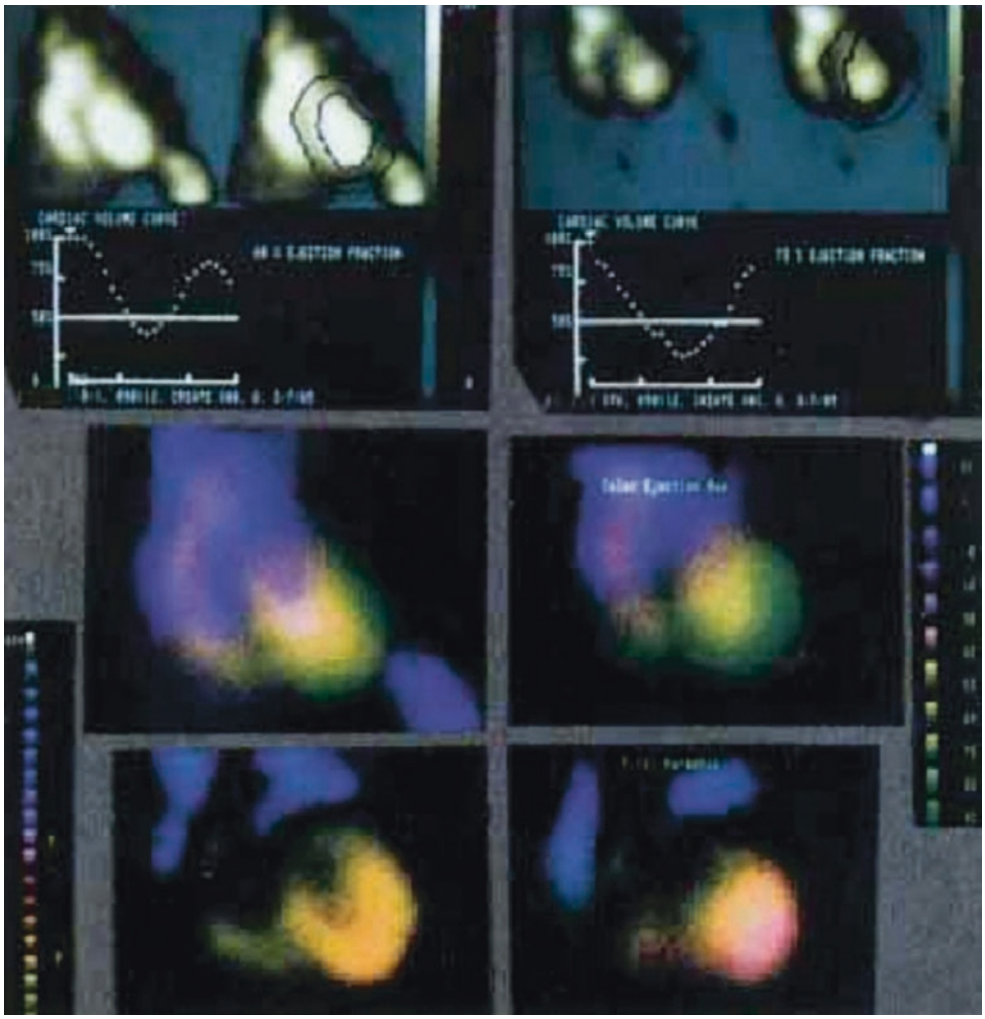

Fig. 7.21 Equilibrium blood pool assessment of aortic regurgitation. Shown are left ventricular (LV) time-versus-activity curves derived from an LV region of interest (*top panel*), ejection fraction images color-coded for regional ejection fraction (*middle panel*), and phase-amplitude images (*bottom panel*) at rest (*left*) and with maximal exercise (*right*) in a young patient with severe aortic regurgitation. Here, the LV edge is derived between the limits of the edges drawn, and the background is taken within these geometric boundaries. Dual color- and intensity-coded images, shown here, permit the integration of multiple parameters in a single image and are an example of the analytic and display potential of the scintigraphic modality. The LVEF increases with exercise. This is supported by the increased area covered by *yellow* and *green* and high ejection fraction values in the ejection fraction image. Although colors shift to later phase angles as heart rate increases, the amplitude and intensity are maintained, and apparent ventricular size decreases in all images, consistent with a normal response to exercise. The uniform phase shift, related to increased symmetry of the time-versus-radioactivity curve with increased heart rate and shortening of end diastole, represents a normal finding, as do all the image results shown here [43]

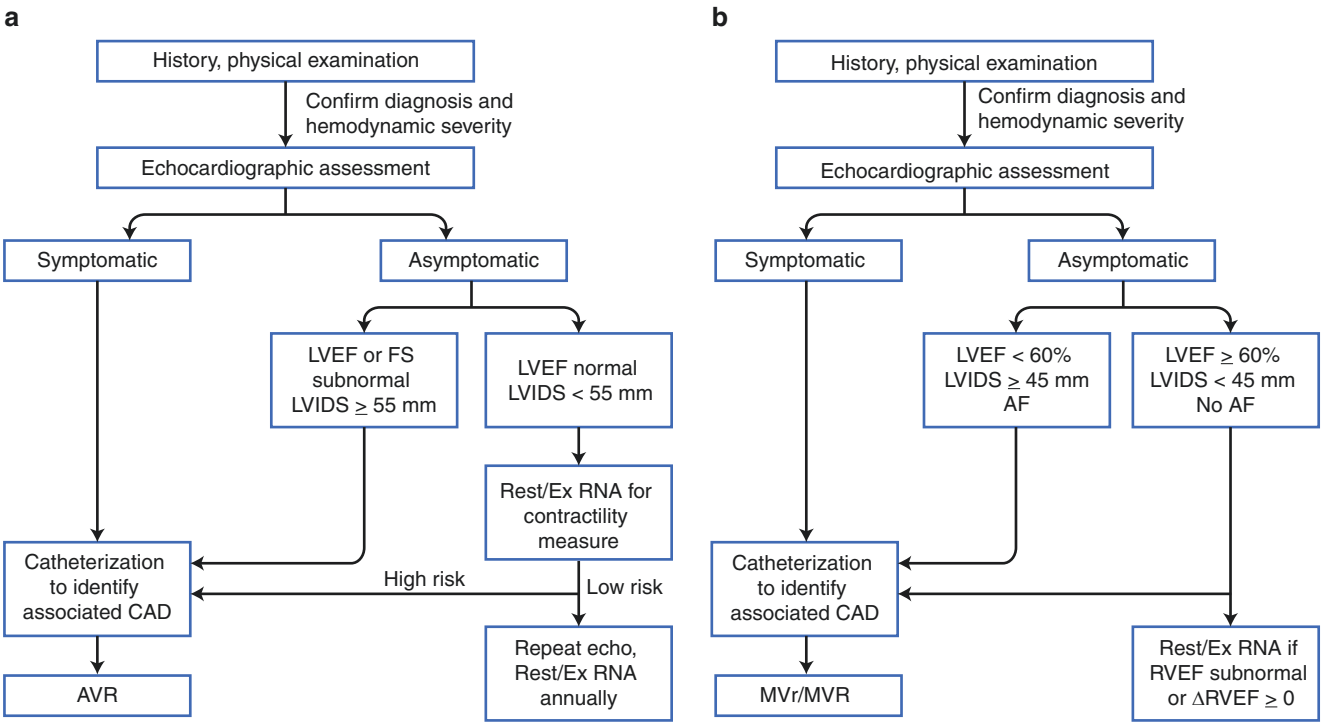

Fig. 7.22 Role of RNA in patients with aortic regurgitation (**a**) and mitral regurgitation (**b**). For asymptomatic patients with regurgitant valvular diseases, echocardiography (echo) is a primary method for diagnosis and for determination of the hemodynamic severity of disease. If echocardiography unequivocally demonstrates subnormal LVEF at rest or "high-risk" left ventricular systolic or diastolic dimension descriptors, management decisions can be made with confidence. For patients with severe aortic regurgitation (**a**) however, the geometric irregularity and regional functional variability of the large left ventricle may result in ambiguity of ejection fraction determination, obviated by non–geometry-dependent evaluation with RNA; if echocardiographic results do not indicate high risk, contractility determination by additional RNA with exercise can detect prognostically important disease. For patients with mitral regurgitation (**b**) the unique capacity of RNA to interrogate right ventricular performance adds an important prognostic dimension not available with echocardiography. In patients with mitral stenosis, a right ventricular ejection fraction (RVEF) determination by RNA carries prognostically important information, but these data have not yet reached routine use in defining management strategies in this setting. Echocardiography remains the primary evaluative modality for mitral stenosis. AF atrial fibrillation, AVR aortic valve replacement, CAD coronary artery disease, Ex exercise, FS echocardiographic fractional shortening, LVIDS left ventricular internal dimension at end systole, MVr mitral valve repair, MVR mitral valve replacement

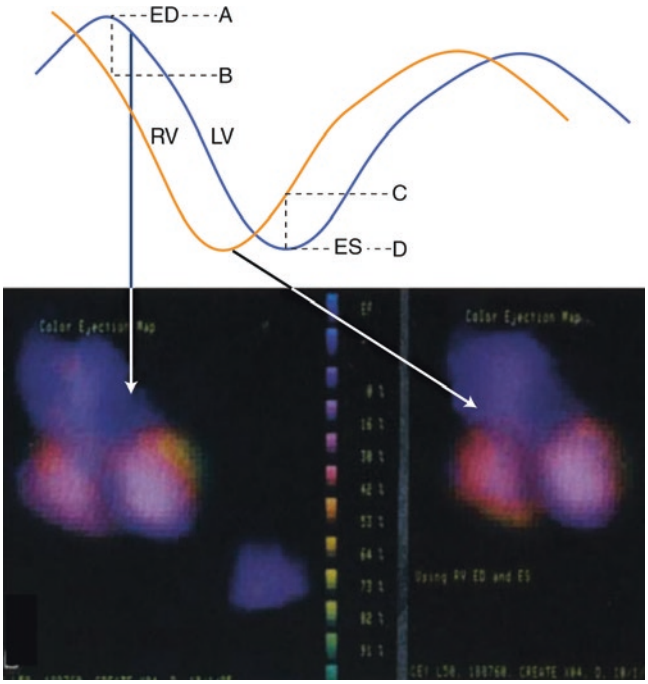

Fig. 7.23 Effect of conduction abnormality. Shown are time-versus-radioactivity curves in a patient with left bundle branch block. The LV curve lags behind the RV curve. The ejection fraction image is derived from frames chosen at LV end diastole (ED) and end systole (ES). Owing to the conduction abnormality, LVED (**a**) and LVES (*D*) correspond to points when the RV is partially filled (**b**) and incompletely emptied (**c**) giving rise to an artificially reduced RVEF. At the *bottom* are color-coded EF images in a patient with a left bundle branch block compiled using frames optimized for LVED and ES (*left*) and for RVED and ES (*right*). Note the bright *green–yellow* area at the LV base (*left*) and the augmentation of high EF colors in the RV (*right*) in these images, derived from different aspects of the same data [43]

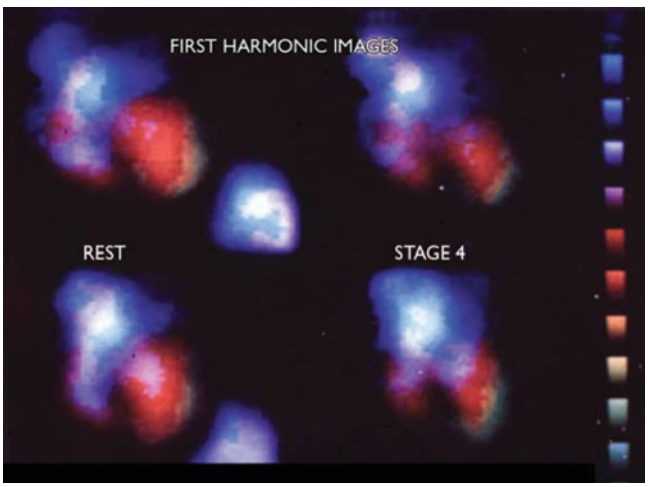

Fig. 7.24 Exercise evaluation. Shown are color ejection fraction images at rest (*left*) and with maximal exercise (*right*) in a patient with CAD (*top*) and with aortic regurgitation (*bottom*). A reduced presence of the "ejection shell," the green and yellow high ejection fraction colors at rest (*left*), demonstrates a decrement in regional function and overall LVEF at stress (*right*) in the CAD patient, whereas reduced LV size with an increased green "ejection shell" demonstrates an augmented LVEF in the patient with aortic regurgitation (*bottom*). Such functional images condense a wealth of information and provide objectivity to the assessment of the effects of intervention on ventricular size and function [43]

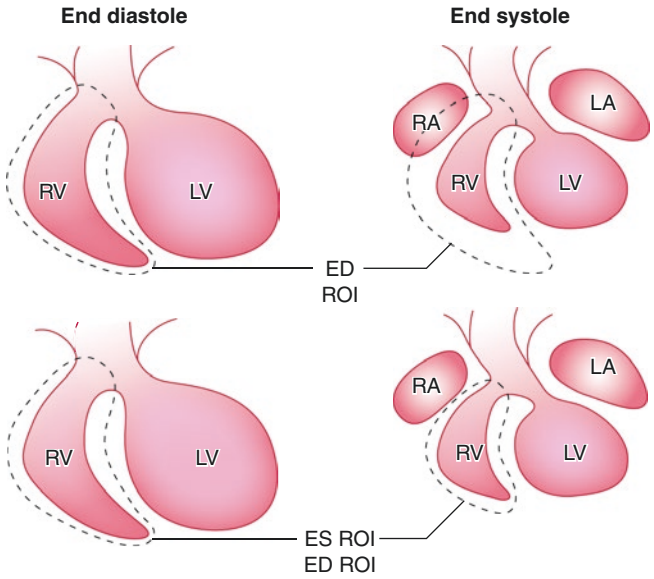

Fig. 7.25 Right ventricular (RV) ejection fraction. Shown diagrammatically is the application of an RV region of interest (ROI) to an equilibrium blood pool study in end diastole (ED) (*left*) and in end systole (ES) (*right*). At *top*, the same ED region is applied in ES with an erroneous inclusion of the right atrium (RA), which is largest in the ventricular ES below, and is ES-specific (ROI is applied with significant improvement, but without total correction for RA overlap on the RV). LA left atrium; LV left ventricle. (Adapted from Botvinick et al. [43])

Regurgitant index

$$RI = \frac{LVSVC}{RVSVC}$$

RF = Regurgitant fraction

$$RF = \frac{LVSVC - RVSVC}{LVSVC}$$

$$RF = \frac{\frac{LVSVC}{RVSVC} \quad \frac{RVSVC}{RVSVC}}{\frac{LVSVC}{RVSVC}} = \frac{RI - 1}{RI}$$

Fig. 7.26 Formulas for the regurgitant index (RI) and the regurgitant fraction (RF). These are parameters applied to determine the severity of regurgitant lesions. The RI is the ratio of the left ventricular stroke volume measured in counts (LVSVC) and the right ventricular stroke volume measured in counts (RVSVC). The amount that LVSVC exceeds RVSVC is a measure of the regurgitant volume and is expressed as the RI. The RF is that percentage of the LVSV that is regurgitating and adding to the overall LVSVC. However, scintigraphically, both measures fail to correct for right atrial overlap on the right ventricle. This error causes an underestimation of the RVSV and an exaggeration of the RI, which may be as high as 1.3 in normal subjects

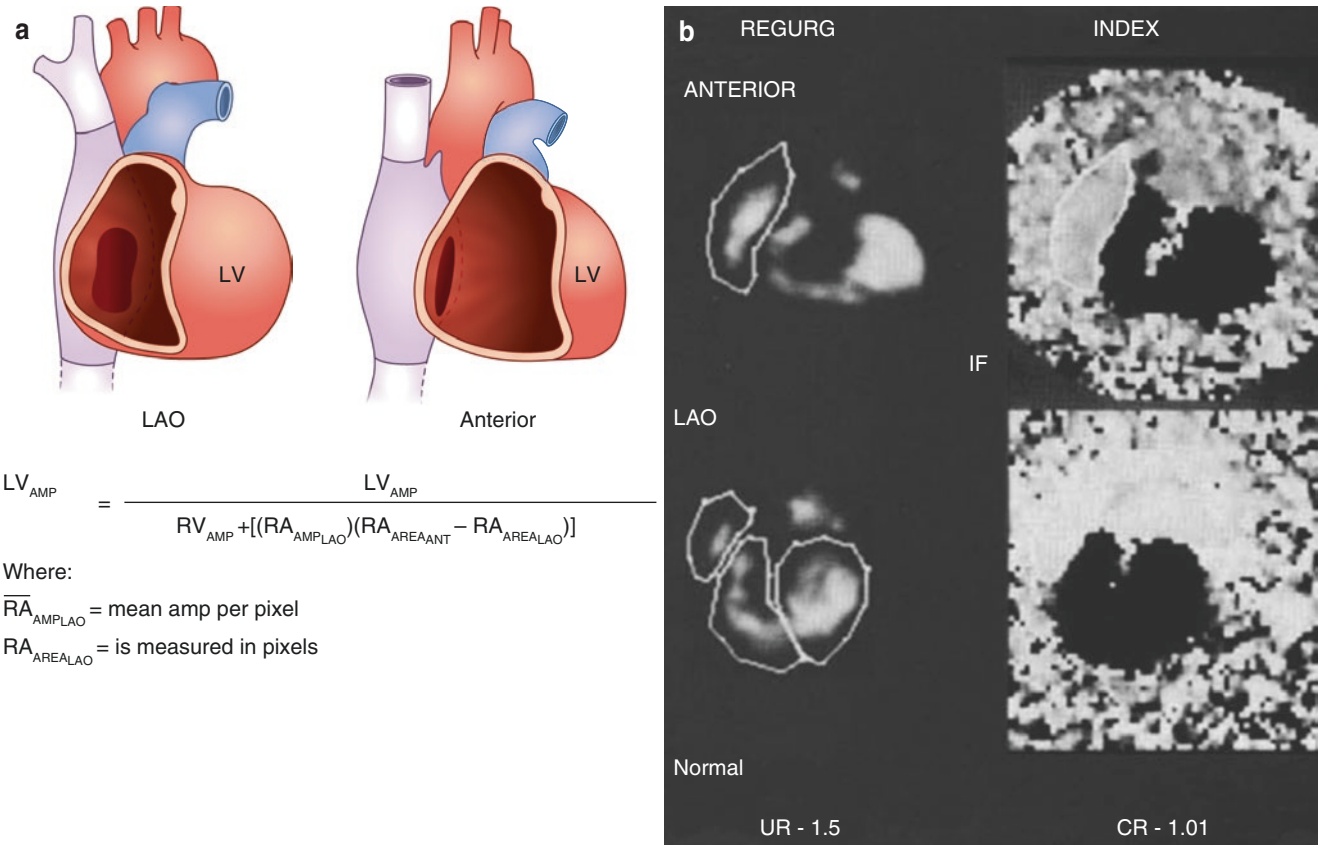

$$LV_{AMP} = \frac{LV_{AMP}}{RV_{AMP} + [(\overline{RA}_{AMP_{LAO}})(RA_{AREA_{ANT}} - RA_{AREA_{LAO}})]}$$

Where:

$\overline{RA}_{AMP_{LAO}}$ = mean amp per pixel

$RA_{AREA_{LAO}}$ = is measured in pixels

Fig. 7.27 Regurgitant index (RI) corrected for right atrial (RA) overlap. The anatomic basis (**a**) for the amplitude-based correction (AMP) of RI for RA overlap [46]. Here, right ventricular (RV) amplitude, an analogue of stroke volume, is corrected with the addition of the product of the mean per-pixel amplitude of the RA in the left anterior oblique (LAO) projection and its area, measured in pixels of the RA that are obscured by the RV, the difference in the RA area measured on anterior (ANT) and LAO projections. This correction results in the reduction of the RI to unity in normal subjects and, compared with the uncorrected value, correlates much better with other measures of valvular regurgitation, as shown in the clinical example (**b**). Given the ubiquity and capabilities of echocardiography with Doppler evaluation, it is the method of choice for evaluation of regurgitant lesions [46]

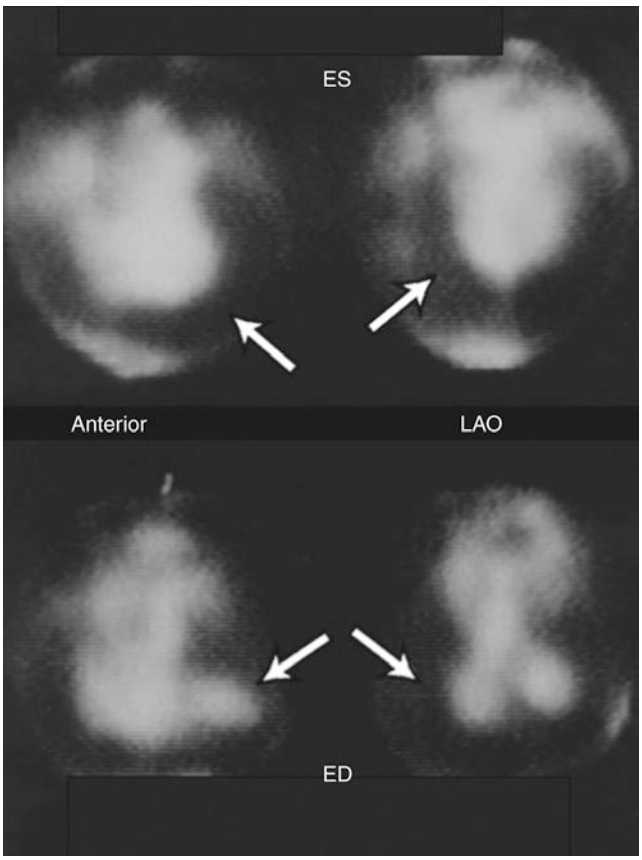

Fig. 7.28 Pericardial tamponade. Shown are left anterior oblique (LAO) and anterior views in end systole (ES) (*top*) and end diastole (ED) (*bottom*) in a man with severe fatigability and weakness several weeks after coronary bypass graft surgery. The large "photopenic" region around both ventricles indicates a large pericardial effusion (*arrows*). The small, volume-starved left ventricle is consistent with tamponade, which was the eventual diagnosis

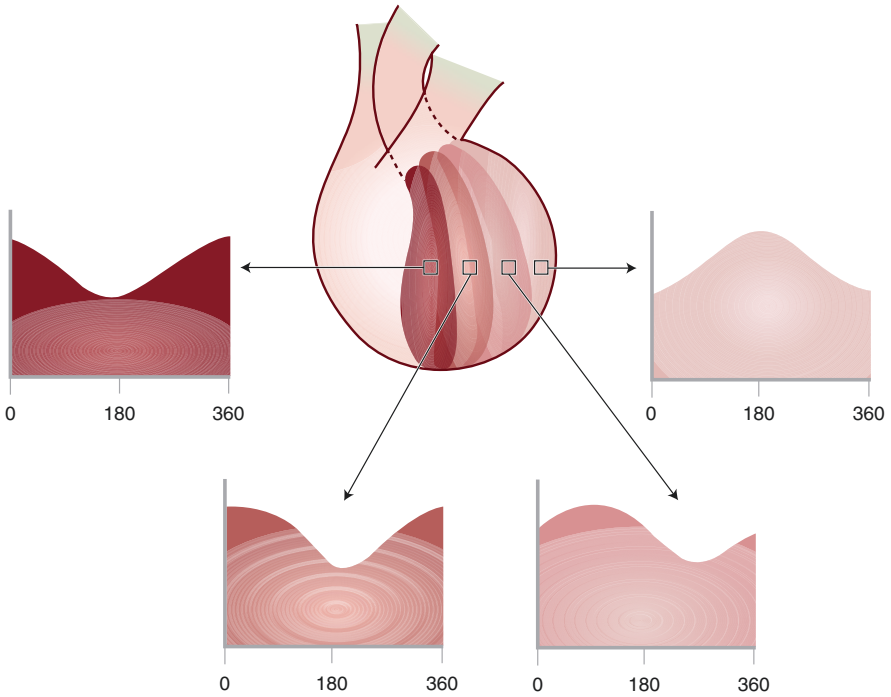

Fig. 7.29 Phase analysis. This diagram presents a ventricle that is gray-scale coded for increasing delay in contraction sequence, from the septum to the lateral wall. The resultant cosine curves, fitted to the regional time-versus-radioactivity curve, are shown below. The septum and its corresponding curve begin contraction at the R wave. The region has a phase angle of 0° and is coded as dark. The lateral wall and its related cosine curve fill when the ventricle should empty. This wall would demonstrate paradoxical motion, and the curve would have a phase angle of 180° [47]

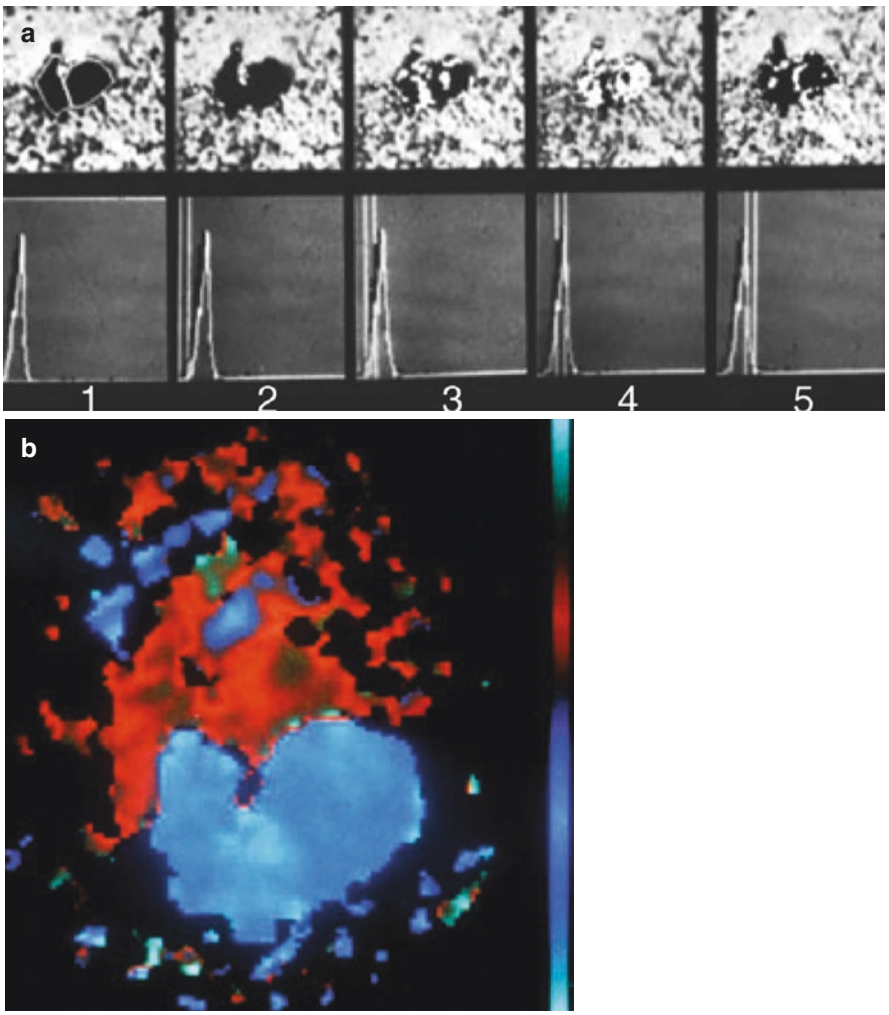

Fig. 7.30 Phase image with normal conduction. (**a**) Phase image (*top*) and left (*white*) and right (*black*) ventricular histograms (*bottom*) plotting the phase angle on the abscissa and its frequency of occurrence on the ordinate in the "best septal" LAO projection in a patient with normal conduction. The serial phase angle is sampled in the intervals of the vertical gray bars setting the histogram windows, and the corresponding spatial location is indicated by a progressive white highlight of associated pixels on the phase image, from left to right. The earliest phase angle is seen at the base of the septum. (**b**) A background subtracted color composite image of the sequential phase angle in this patient reveals symmetric phase distribution and contraction of the two ventricles

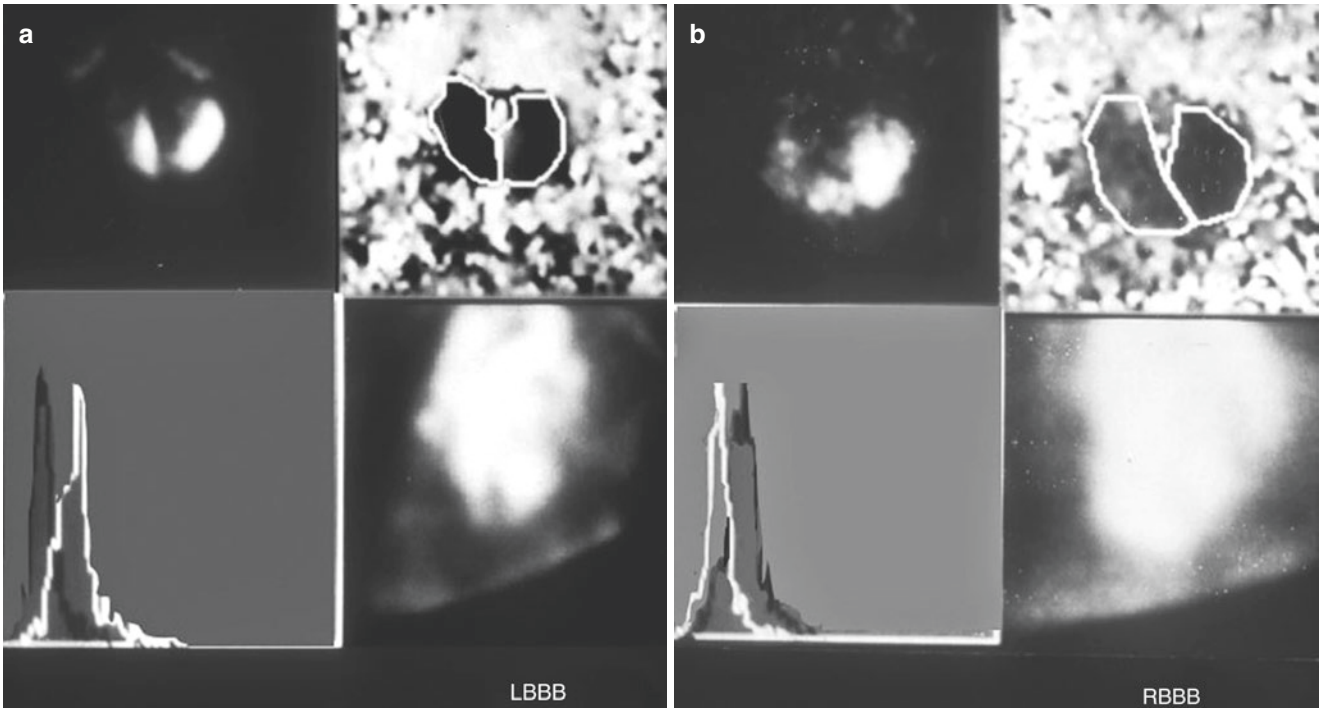

Fig. 7.31 Phase images in a bundle branch block. Shown are amplitude images (*upper left*), phase images with right and left ventricular regions of interest (*upper right*), phase histograms (*lower left*), and summed blood pool images in the "best septal" LAO projections in patients with left bundle branch block (LBBB) (**a**) and right bundle branch block (RBBB) (**b**) [45]. The phase histogram plots left (*white*) and right (*black*) ventricular histograms, with phase angle on the abscissa and its frequency on the ordinate. The right ventricular phase histogram and right ventricular activation are earliest in LBBB, whereas the left ventricular histogram and activation are earliest in RBBB [47]

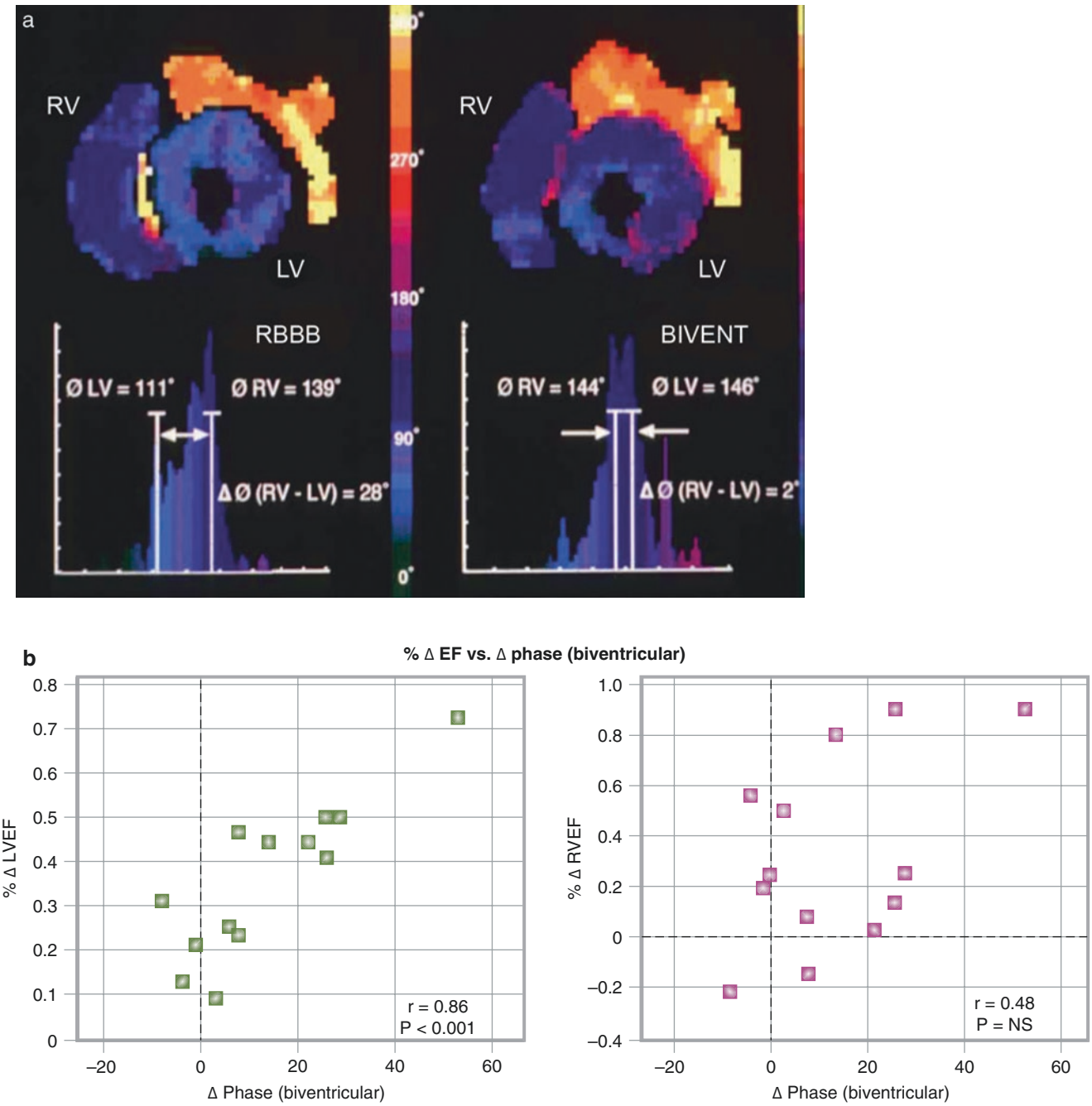

Fig. 7.32 The effects of biventricular (Bivent) pacing. (**a**) Phase images and RV and LV phase histograms from a heart failure patient with baseline RBBB are shown, before and after placement of a biventricular pacemaker [46]. The difference in the mean ventricular phase angle is reduced, with increased interventricular synchrony. (**b**) The inverse relationship between the LVEF (*left*) and the RVEF (*right*) and the interventricular phase difference. That is, the greater the reduction brought by biventricular pacing in the difference between the mean phase angles of RV and LV, the greater the subsequent improvement in LVEF. (From Kerwin et al. [48]; with permission from Elsevier)

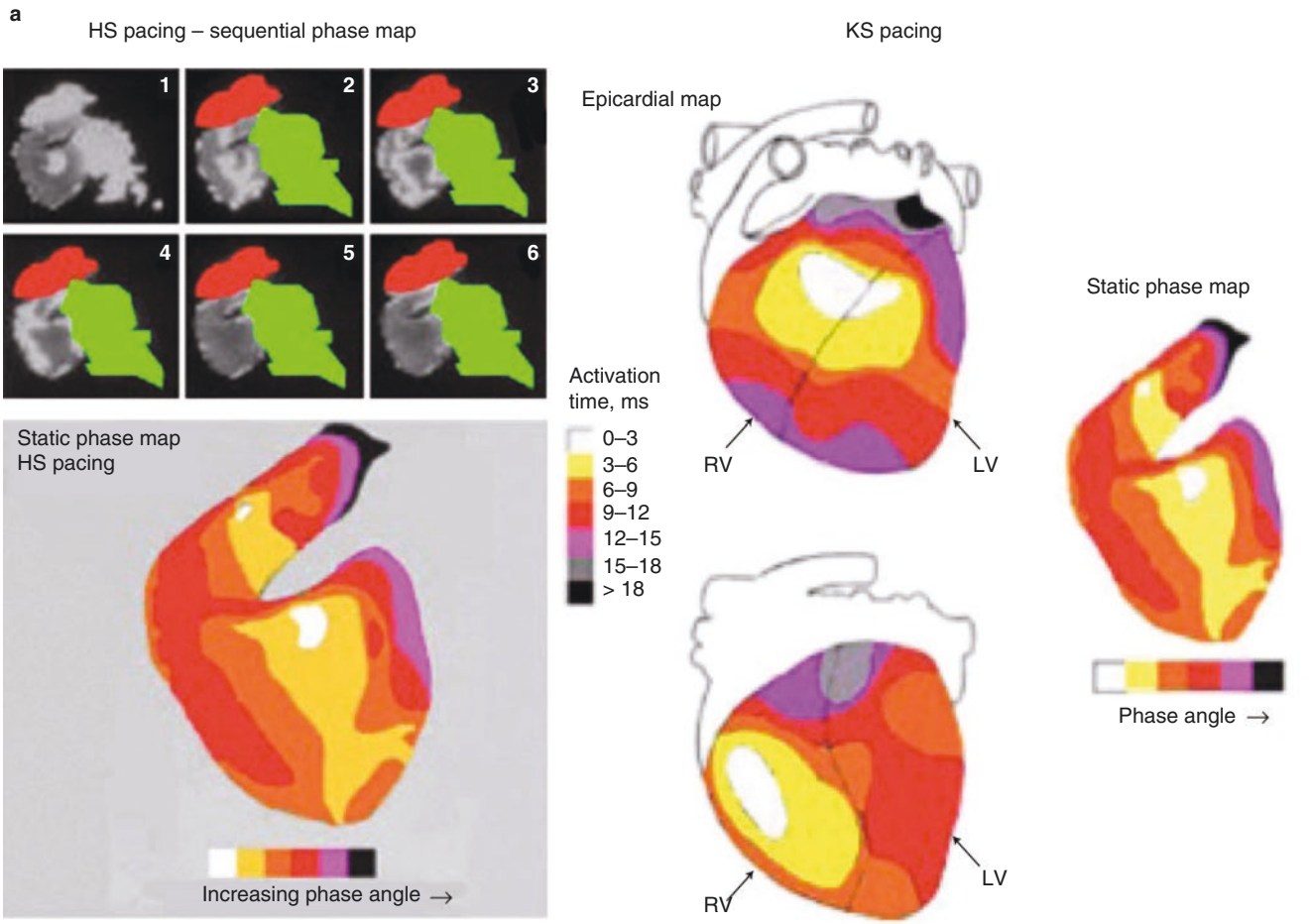

Fig. 7.33 Relationship between myocardial contraction (scintigraphic phase image analysis) and conduction (electrophysiologic mapping). This dog study was performed to validate the relationship between contraction and conduction, which is of high potential importance to patients. It could be applied with significance to answer other questions of great clinical importance, as shown in the study illustrated in Fig. 7.34. (**a**) High-septal (HS) pacing. Phase images are shown in the *top left* image. Shown in a left oblique projection are frames in a sequential phase map, from 1 through 6, demonstrating the serial progression of the phase angle and related contraction in an infarcted dog. The ventricles are in *gray* in the upper left image with progressive phase intervals shown in *white highlight*. The right atrium is masked in *red* and the left atrium in *green*. A phase map (*lower left*) is based on the images in the *top left* panel. This diagram characterizes the sequence of phase progression in six color-coded intervals to match the pattern in the *top left image*. Increasing the phase angle and contraction delay is shown in the color code (*below*). The number of phase intervals illustrated in this and subsequent figures has been chosen empirically to illustrate the sequence of progression in association with contraction patterns of varying rate and complexity. Good phase and electrophysiologic activation map (EAM) agreement is shown in the *right* panel. Shown at *right* is the same diagram of serial phase progression, the phase map. At *left* are anterior (*above*) and posterior (*below*) views of the epicardial map presented in seven color-coded intervals. The parallel of the conduction pattern on the epicardial map with the phase map sequence is evident. (**b**) Right ventricle (RV) pacing. Phase images are shown in the *top left* image. Shown in a left oblique projection (as in **a**) are frames in a sequential phase map, from 1 through 6, demonstrating the serial progression of phase angle and related contraction, with RV pacing in the same dog. The ventricles are in *gray* in the upper left image with progressive phase intervals in *white*, and the atria are again masked. Shown in the *lower left* is the phase map of the images in the *top left* panel, where the phase map is a diagram characterizing the sequence of phase progression in six color-coded intervals. Incomplete phase and EAM agreement is shown in the *right* panel. Shown at *right* is the same diagram of serial phase progression shown in the *top left* panel. At *left* are anterior (*above*) and posterior (*below*) views of the epicardial map presented in seven color-coded intervals. The parallels and inconsistencies with the phase map are evident. (**c**) Left ventricle apical (*LVa*) pacing. A phase map (*top left*) again Is a left oblique projection, with frames sequential from 1 through 6, demonstrating a serial progression of phase angle and related contraction, with LVa pacing in the same dog. The ventricles are in *gray,* with progressive phase intervals sequentially highlighted in *white*. The atria are again masked in the same way. The *bottom left* image is a phase map of the images in the *top left* panel, where the phase map is a diagram characterizing the sequence of phase progression in nine color-coded intervals to match the pattern of the *top left* panel. Good phase and EAM agreement is shown in the *right* panel. Shown at *right* is the same diagram of serial phase progression shown in the *top left* panel. At *left* are anterior (*above*) and posterior (*below*) views of the epicardial map presented in eight color intervals. The parallel with the phase map is evident. (From Munoz del Romeral et al. [49]; with permission from Springer Nature)

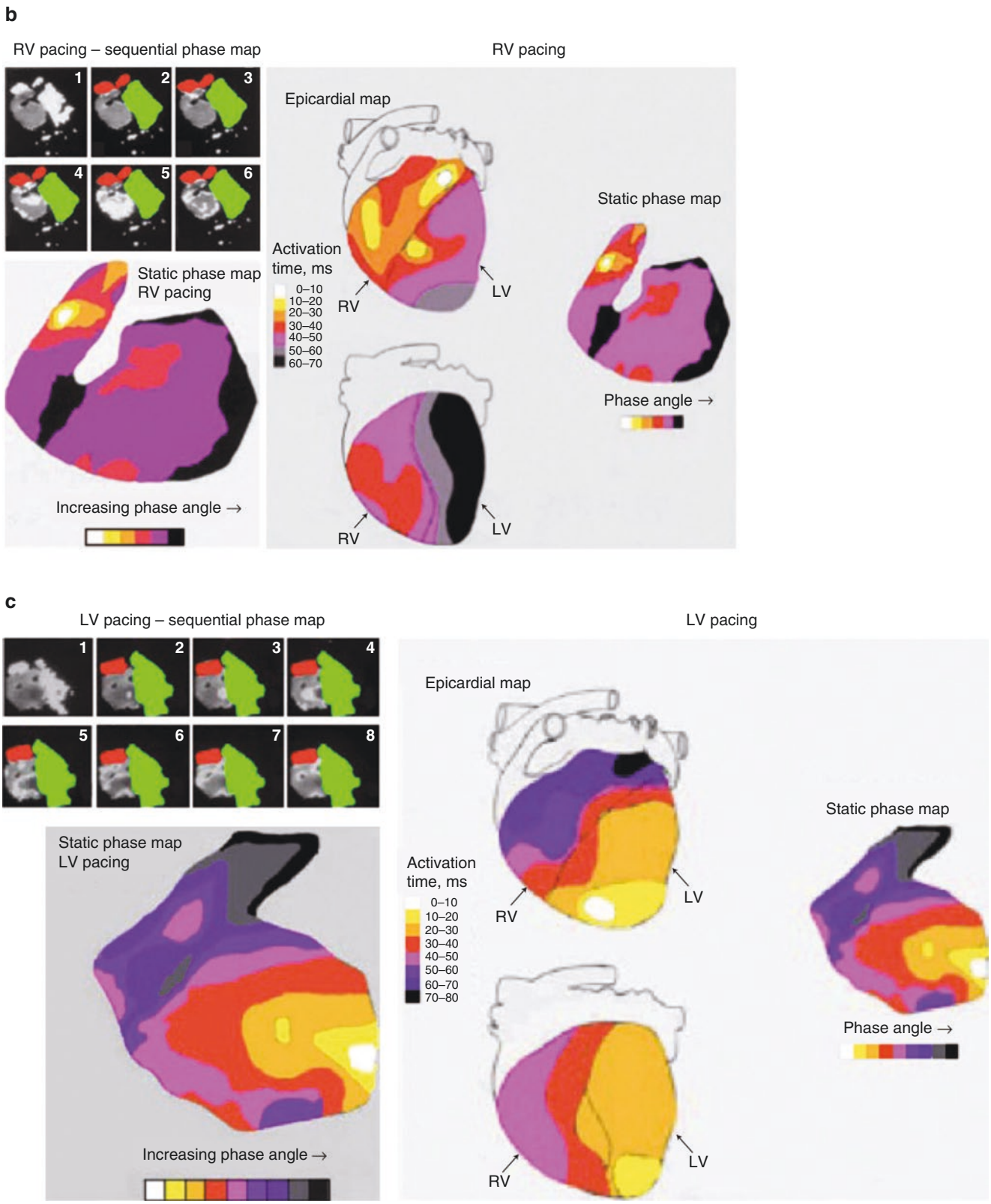

Fig. 7.33 (continued)

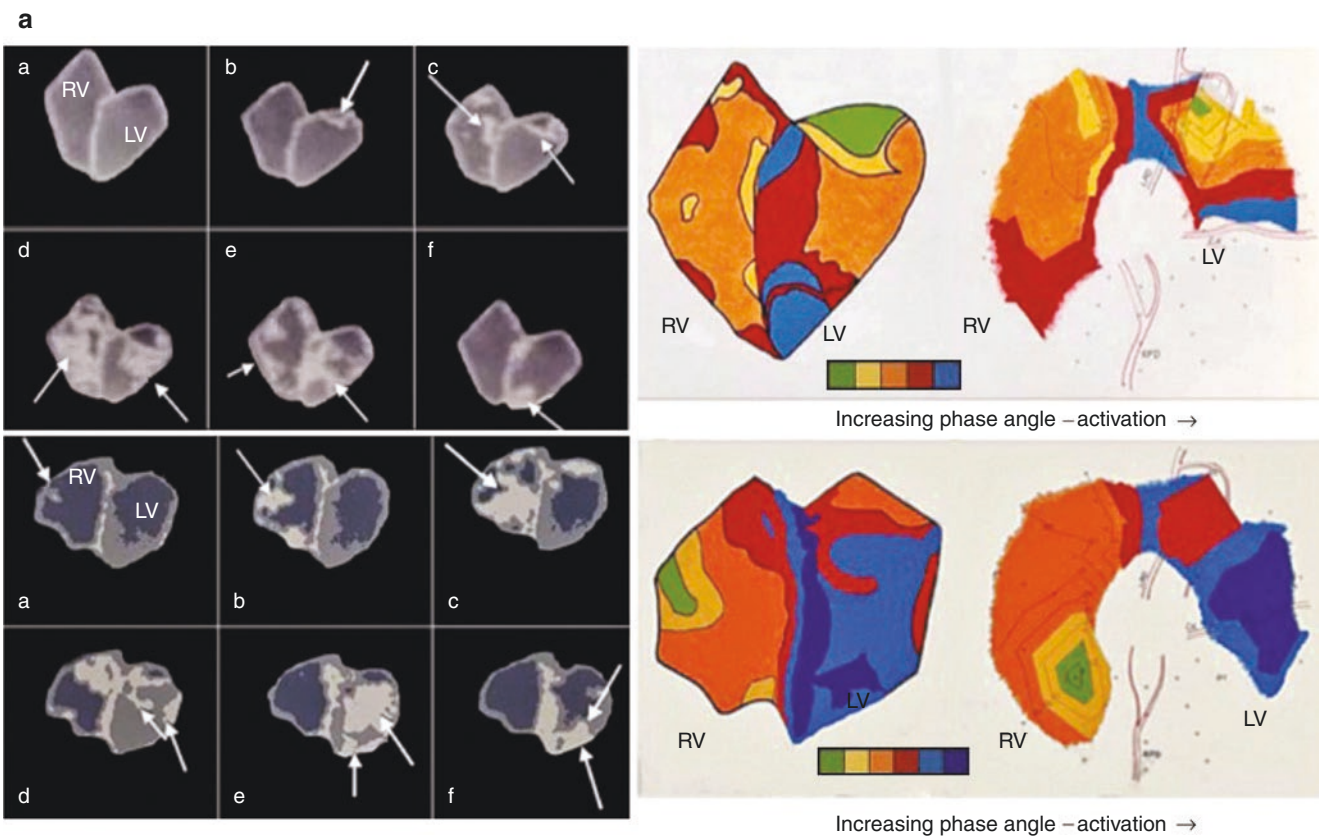

Fig. 7.34 Variable functional effects of pacing site in normal and scarred ventricles. The value of equilibrium RNA in investigative work is illustrated here in images from an animal study of cardiac resynchronization therapy that could have wide implications for the treatment of advanced heart failure patients with biventricular pacemakers. (**a**) Phase and isochronous epicardial maps. Shown are serial phase images with a masked background, in a normal animal studied with high septal (HS) pacing (*top left*) and in an infarcted animal with RV pacing (*bottom left*). Progressive whitening of the phase images in *a* to *f* delineates the course of progression of a serial phase angle and related contraction through the right and left ventricles. *Arrows* in *a* and *b* of each figure part localize the site of the earliest phase angle. Subsequent *arrows* point to areas of sequential phase angle progression. The *left* images of the *right* panels are diagrammatic color-coded phase maps that summarize the serial phase progression of the phase image in the figures they follow: *upper right*, with HS pacing, and *lower right*, with RV pacing of an infarcted ventricle. Here, the color progression, shown in the color scale at the bottom of each figure, parallels the phase progression highlighted in *white* in the preceding figures. The *right* images in the *right* panels present the related color-coded isochronous epicardial maps, which summarize the serial activation pattern, here related to their associated phase maps (*left*), drawn in the anatomically opened RV and LV, with walls exposed. The coronary distribution is roughly illustrated by the left anterior descending (LAD) coronary artery, left circumflex coronary artery, and right posterior descending coronary artery. In each case, serial phase progression related well to the epicardial activation sequence. In the normal ventricle (*upper* panels), the phase angle progressed through contiguous LV regions. Contrast phase images (*lower left*), summarized in the *left* image in the *lower right* panel in the animal with a distal LAD infarction, reveal an initially contiguous phase progression (*arrows*, *c* and *d*), until near the infarct area. Here, myocardial contraction "skips" a distal myocardial region between the *arrows* in *e*. This region demonstrates delayed phase progression (*arrow*, *f*). A similar pattern was well seen on the activation map (*lower right*, *right* image), with some variation. (**b**) Blood pool images. Shown are end-diastolic (ED) and end-systolic (ES) frames from the ERNA acquired in an animal with an LAD myocardial infarction (MI), during baseline normal sinus rhythm (NSR, *above*) and with septal pacing (*below*). Normal RV and LV wall motion (*arrows*) is evident and confirmed by the superimposition of ED (*black*) and ES (*red*) contours. (**c**) ED and ES frames from the ERNA acquired in the same animal illustrated in (**a**) now during RV pacing (*above*) and with LV apical pacing (*below*). Evident is apical hypokinesis with the RV pacing site, as well as apical dyskinesis and an apical aneurysm with LV apical pacing. Again, LV wall contours are drawn and superimposed for ED (*black*) and ES (*red*). These images clearly demonstrate variable regional LV wall motion and systolic function with a variation of the pacing site in relation to an LV infarction. This same principle could be applied to recognize the benefits of specific cardiac resynchronization therapy pacemaker locations and, potentially, to optimize them. (From Munoz Del Romeral et al. [50]; with permission from Springer Nature)

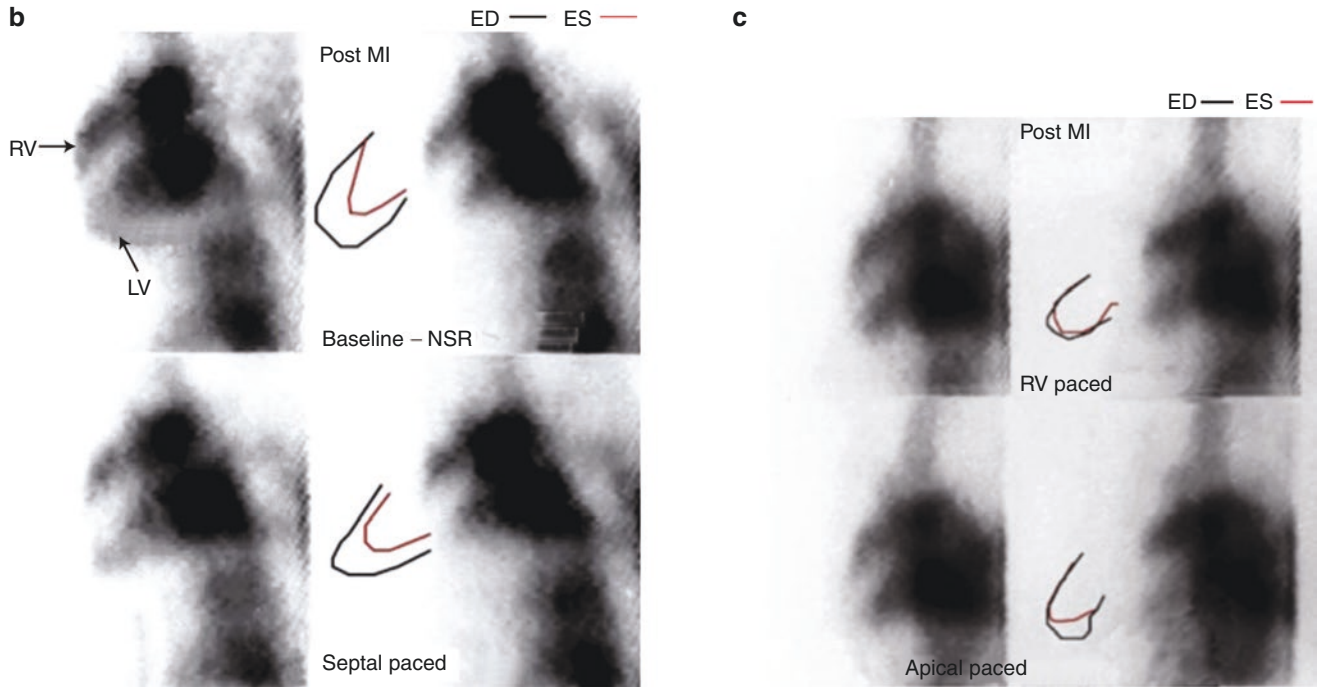

Fig. 7.34 (continued)

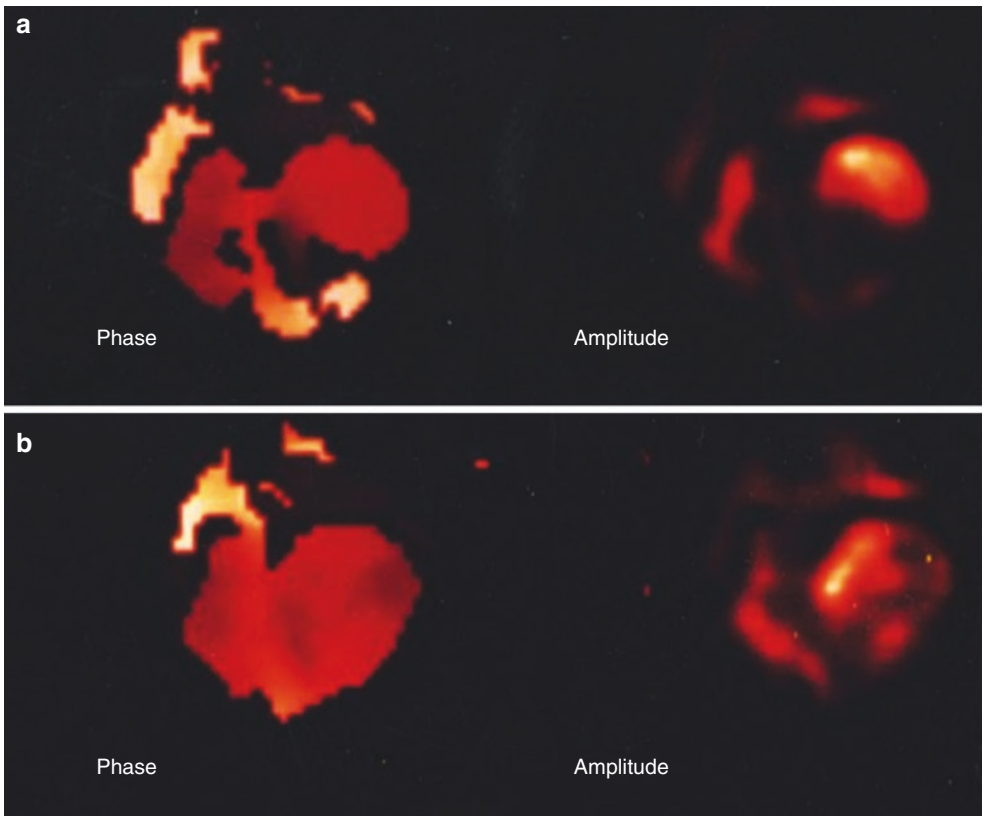

Fig. 7.35 Phase image analysis of synchrony before and after biventricular pacing. Shown are examples of phase and amplitude images derived from gated equilibrium blood pool scintigrams in a patient with advanced systolic heart failure [51]. In such patients, the placement of pacemakers in both the right ventricle and the left ventricle, as well as biventricular pacing, serves as an advanced interventional therapy, cardiac resynchronization therapy (CRT). (**a**) Images from the patient were acquired at baseline, with evidence of gross regional dyssynchrony in the phase image at *left* (white color in the septum and apex) and with reduced amplitude in most of the distal left ventricle, as shown by the low-intensity regions of the amplitude image at *right*. (**b**) The color is more homogeneous and phase is more synchronous, with much improvement in the intensity of the amplitude image following biventricular pacemaker insertion. Not surprisingly, the patient was much improved clinically following the procedure. This method has been tested and validated for accuracy and reproducibility of synchrony measurement in 48 normal subjects [51, 52]

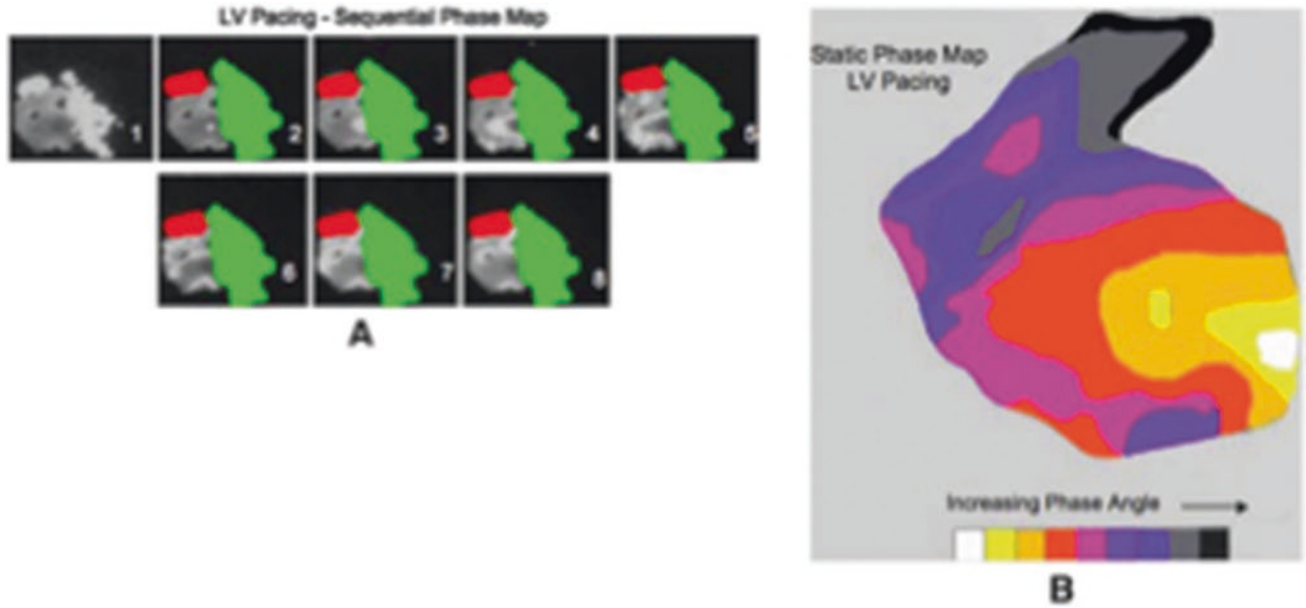

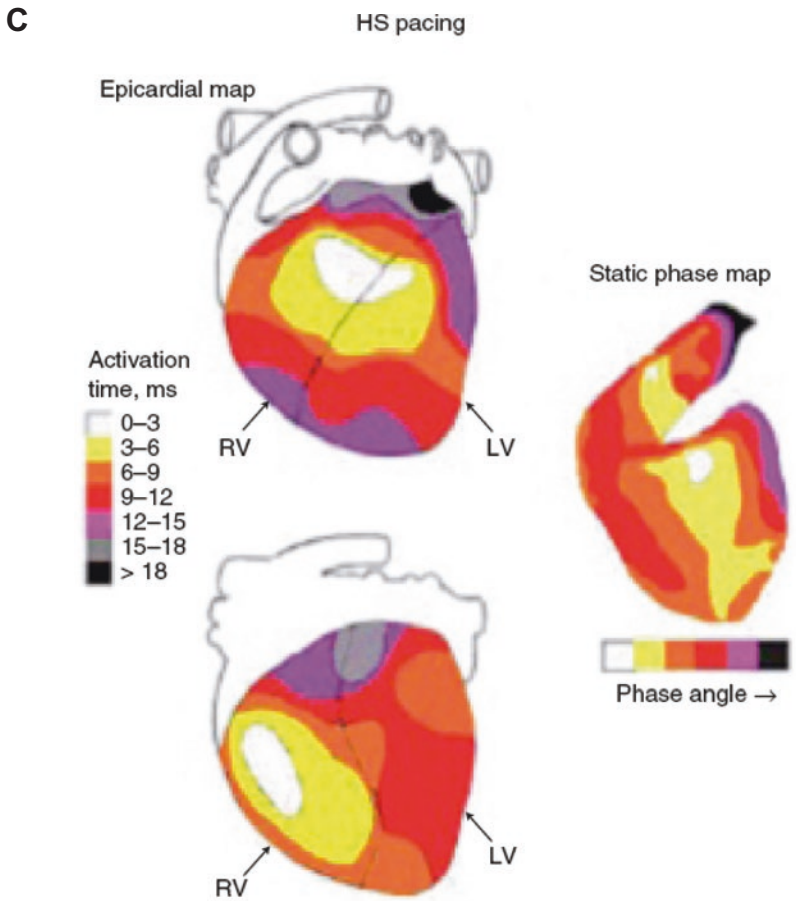

Fig. 7.36 Atrial LV pacing. (**a**) Sequential frames in phase map. Shown at *upper left*, in a left anterior oblique projection, are frames in a sequential phase map, from 1 through 6, demonstrating serial progression of phase angle and related contraction, with atrial LV pacing in a dog model. The ventricles are in gray in the *upper left* image with progressive phase intervals sequentially highlighted in white. The atria are in *green*. (**b**) Phase map. Shown is a phase map of the images in (**a**), a diagram characterizing the sequence of phase progression in nine color-coded intervals to match the pattern of (**a**). (**c**) Good phase and epicardial map agreement. Shown at *right* is the same diagram of serial phase progression shown in (**a**). At left are anterior (*above*) and posterior (*below*) views of the epicardial map presented in eight color intervals. The pattern agreement with the phase map is evident. (From Munoz del Romeral et al. [49]; with permission from Springer Nature)

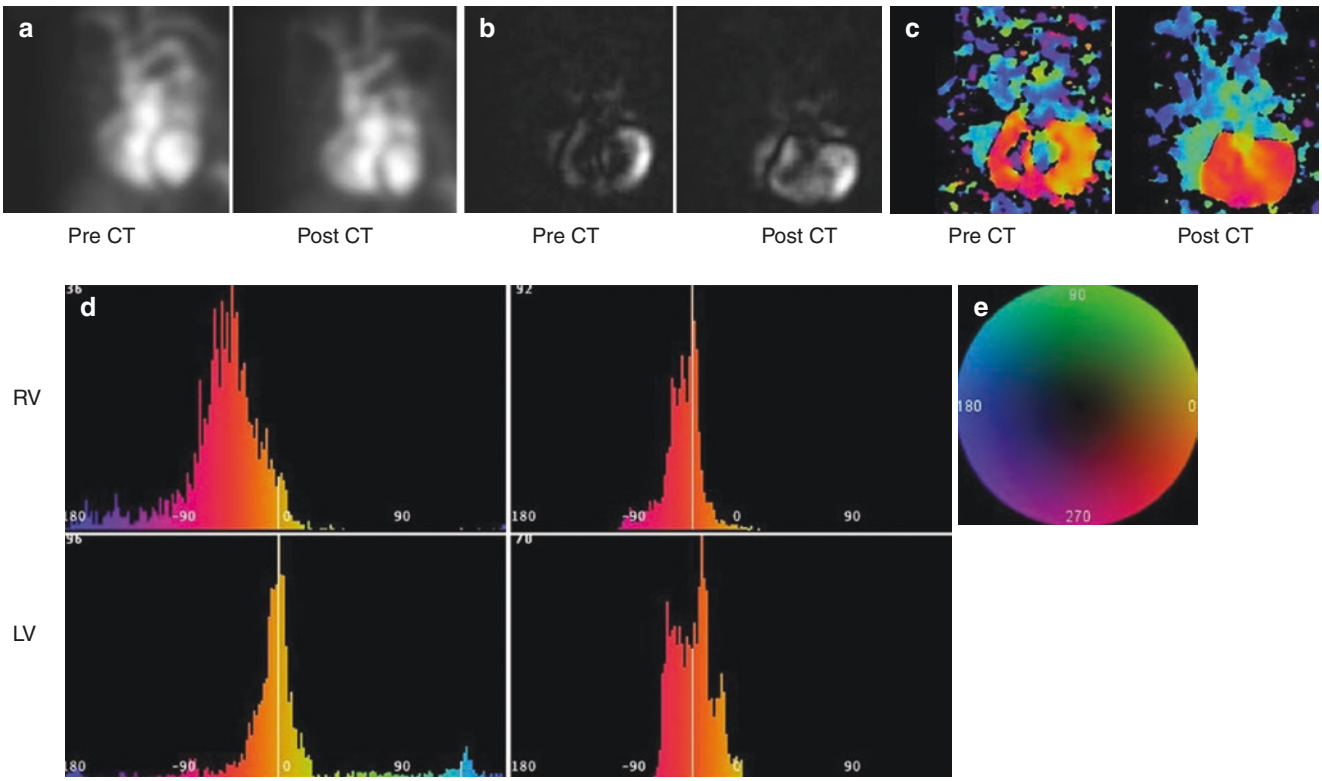

Fig. 7.37 Good outcome of cardiac resynchronization therapy (CRT). Heart failure (HF) is the most frequent cause of cardiac hospitalization in the United States, affecting 5,000,000 patients, with 250,000 deaths yearly. Both ventricular systolic function and synchrony have been shown to have significant prognostic impact in HF. CRT has been proven to reduce both the morbidity and the mortality of HF patients who become refractory to medications and present with a wide QRS. However, improvement of HF with CRT based on clinical and echocardiographic criteria is highly variable; 30–40% of patients do not improve or worsen with CRT. Scintigraphic methods that image myocardial perfusion and function have been adapted for synchrony analysis. SPECT myocardial perfusion scintigraphy combines measures of both perfusion and function, and extracted parameters have been demonstrated to measure ventricular synchrony and even to predict CRT outcomes. ERNA has advantages of higher temporal resolution, greater reproducibility, and volumetric analysis of both ventricles that can be applied for analysis of intraventricular synchrony and interventricular synchrony (IVS). Novel, objective measures of regional contraction and global mechanical synchrony based on the first harmonic fit of the ERNA ventricular time-versus-radioactivity curve, the synchrony (S) and entropy (E) parameters, have been developed and are generated by in-house software. These parameters were demonstrated to be highly reproducible, with both intraobserver and interobserver variability in the range of 2%. Applied in a simulation model, S and E were observed to discriminate better the synchrony profiles among a spectrum of patterns of wall motion than LVEF or the SD of LV phase angle (SDLVØ) measured on the phase histogram, which plots phase angle (Ø) on the abscissa versus its frequency on the ordinate within the LV region of interest (ROI). The aim was to correlate these novel parameters of S and E with clinical outcomes in patients with advanced HF undergoing CRT. (**a**) ERNA cines. Shown are best septal LAO projections of a gated ERNA acquired in a heart failure patient with excellent CRT outcome (before CRT, *left*; after CRT, *right*). NYHA class fell from III to I as ERNA LVEF increased from 22% to 35% with CRT. (**b**) Amplitude images. Shown are amplitude images with intensity proportional to amplitude, derived from cines in (**a**) (before CRT, *left*; after CRT, *right*). Note the more complete appearance of the post-CRT image. (**c**) Phase images. Shown are phase images derived from cines in (**a**) color-coded for phase angle according to the sequence on the color wheel in (**e**) (before CRT, *left*; after CRT, *right*). Note more homogeneous color distribution across both ventricles after CRT. Improved intraventricular synchrony and interventricular synchrony are evident and confirmed on related histograms (**d**)**.** (**d**) Phase histograms. Shown are RV phase histograms (*top*) and LV phase histograms (*bottom*), derived from phase images shown in (**c**) each plotting phase angle on abscissa and its frequency on the ordinate, within respective ventricular ROIs, color-coded for phase angle according to its sequence as in (**e**) (before CRT, *left*; after CRT, *right*). Reduced width and baseline scatter in both histograms after CRT supports improved LV synchrony, which increased from 0.84 to 0.97, whereas LV entropy decreased from 0.69 to 0.50, and the standard deviation of LVØ decreased from 61.7 to 19.62 with CRT, whereas improved vertical alignment of LV and RV histograms after CRT supports improved interventricular synchrony, which decreased from 41.2 to 6.92. (**e**) Color wheel. Here the color code is applied to serial phase angles in images and histograms, above and below, where the earliest ventricular phase angle is at approximately 0° [53]

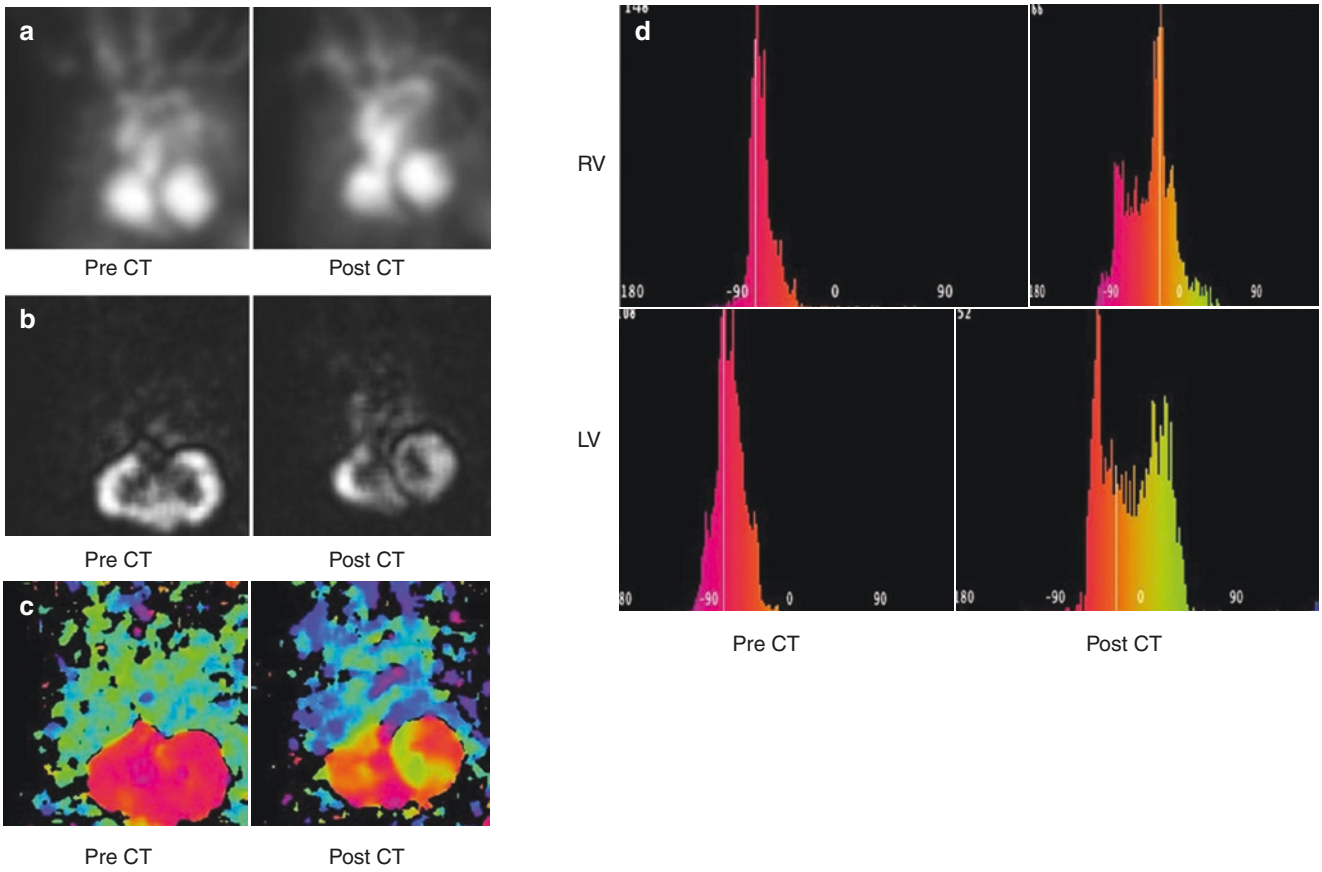

Fig. 7.38 ERNA images of a patient with poor CRT outcome. (**a**) ERNA cines. Shown are the best septal LAO projections of the gated ERNA acquired in a HF patient with a poor CRT outcome (before CRT, *left*; after CRT, *right*). NYHA class remained at III as pre-CRT LVEF of 35% fell to 30% after CRT. (**b**) Amplitude images. Shown are amplitude images derived from cines in (**a**) (before CRT, *left*; after CRT, *right*). Note the more heterogeneous appearance of the post-CRT image. (**c**) Phase images. Shown are phase images (before CRT, *left*; after CRT, *right*) derived from cines in (**a**) color-coded for phase angle according to sequence on the color wheel in Figure 7.38E. Note more heterogeneous and disparate phase distribution in each ventricle after CRT, compared with homogeneous biventricular distribution before CRT. Color and Ø changes indicate worsening of intraventricular synchrony and IVS confirmed on related histograms (**d**). (**d**) LV phase histograms. Shown are RV phase histograms, *above*, and LV phase histograms, *below* (before CRT, *left*; after CRT, *right*), derived from phase images shown in (**c**). Increased width and spectrum in both histograms after CRT indicates reduced intraventricular synchrony (LVS) as LVS fell from 0.96 to 0.87. LV entropy (LVE) increased from 0.36 to 0.66, and the standard deviation of LVØ (LVSDØ) increased from 12.29 to 28.34, whereas vertical misalignment of LV and RV histograms, apparent after CRT, supports observed increased IVS from 1.97 to 45.19 [53]

SPECT Blood Pool Imaging

With the increase in the use of echocardiographic procedures and the widespread acceptance of gated myocardial perfusion SPECT, gated planar blood pool imaging has decreased to less than 10% of all nuclear cardiac studies performed in the United States, although the percentage may be substantially higher in other countries. Conversely, the case for gated blood pool SPECT has considerably strengthened, owing to the increase in computer speed, the greater diffusion of multidetector cameras, and the general acceptance of state-of-the-art three-dimensional analysis and display techniques. We believe that gated blood pool SPECT will become the most commonly utilized nuclear cardiology method for blood pool scintigraphy, the main rationale for its use being its ability to assess both LV and RV function parameters, without a need for background subtraction. Gated blood pool SPECT images can be displayed in a parametric three-dimensional format, much like gated perfusion SPECT; because the epicardium is not visualized in blood pool imaging, a standard display will represent the LV and RV endocardium as shaded surfaces and their location at end diastole as wire grids (Fig. 7.39). The clinical circumstances in which this procedure is likely to become effective are the same as those in which resting blood pool scintigraphy is currently applied, chief among them the assessment of doxorubicin cardiotoxicity. Blood pool scintigraphy is also commonly employed in serial assessment of patients with aortic insufficiency and congestive heart failure and in patients who have undergone cardiac transplantation. Promising recent data have suggested that phase analysis from blood pool scintigraphy may be of clinical value in selecting patients who might benefit from biventricular pacing for resynchronization. Analysis of a regional and global ejection fraction on gated blood pool SPECT correlates well with independent calculations of regional wall motion based on MRI measurements and is superior to a visual analysis of wall motion [54]. Calculation of LV volumes and ejection fraction by cardiac MRI correlated well with similar measurements on gated SPECT blood pool imaging [55].

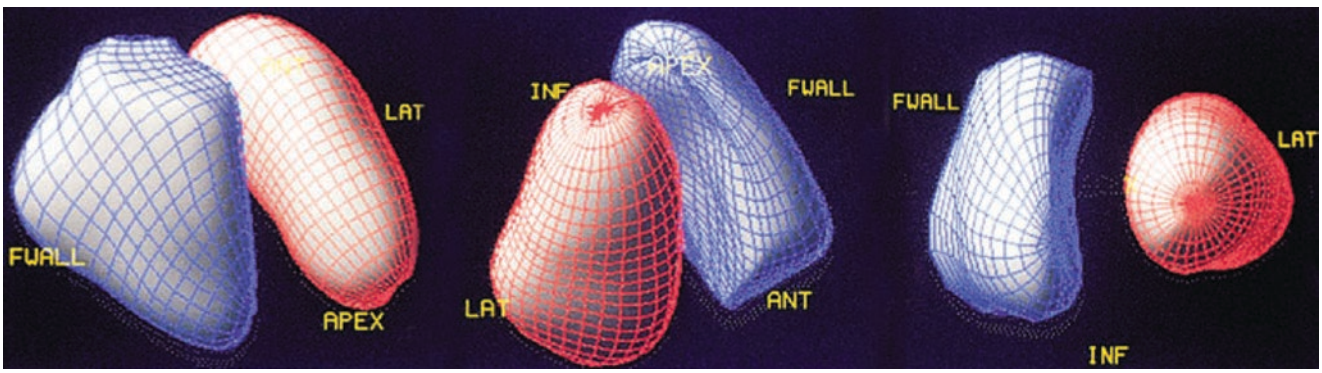

Fig. 7.39 Gated blood pool single-photon emission CT (SPECT): left and right ventricle. ANT anterior LV wall, FWALL free RV wall, INF inferior LV wall, LAT lateral LV wall

Figure 7.40 also illustrates SPECT blood pool imaging, demonstrating three-dimensional reconstructions of SPECT gated equilibrium images from multiple angles in end diastole and end systole.

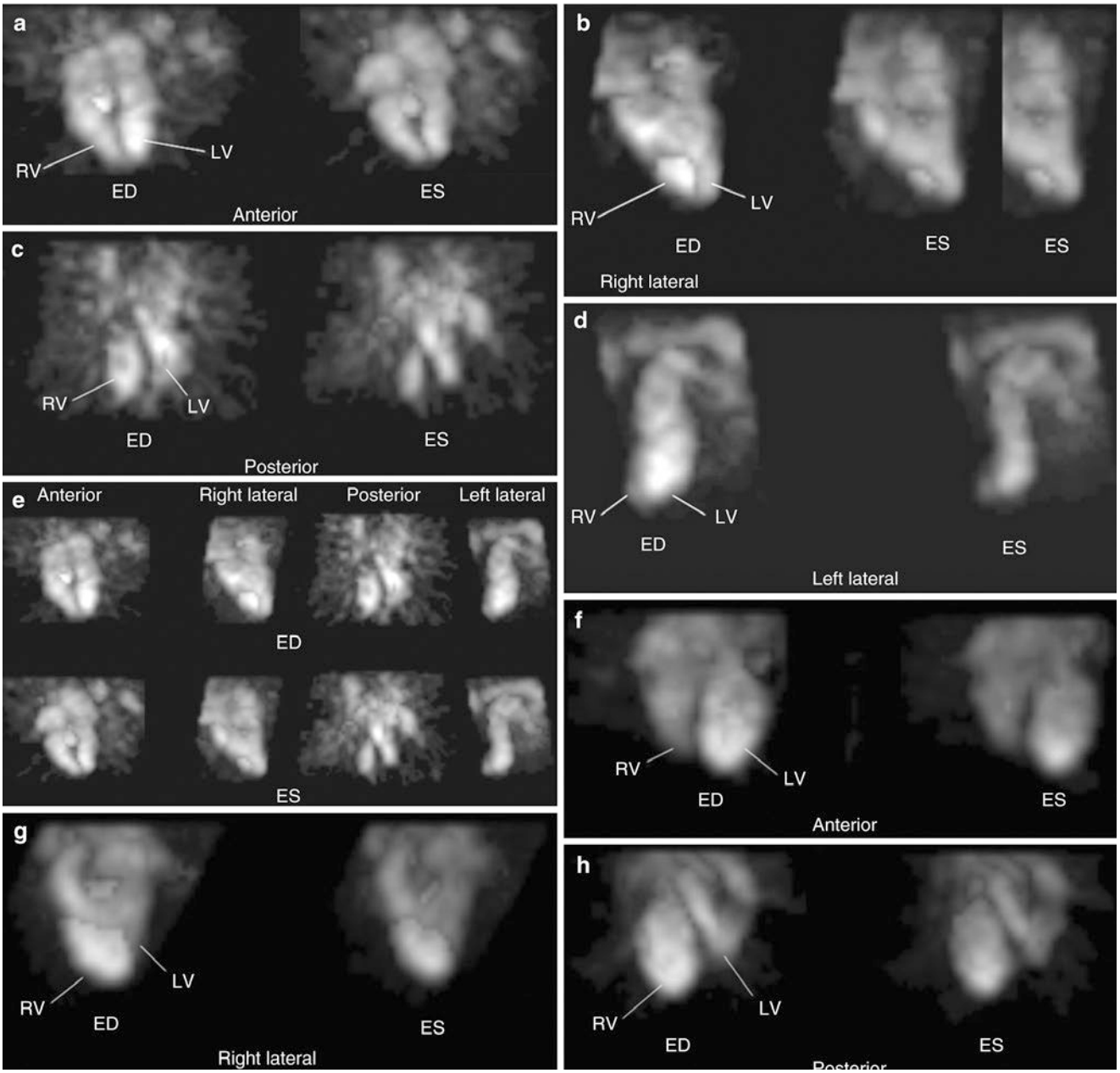

Fig. 7.40 SPECT blood pool imaging. This three-dimensional (3-D) reconstruction of SPECT gated equilibrium images of a normal ventricle in end diastole (ED) and end systole (ES) viewed from multiple angles counterclockwise around a 360° orbit, from anterior (**a**) to right lateral (**b**) to posterior (**c**) and left lateral (**d**) views. (**e**) ED and ES images in all views of this normal heart are shown in a single panel. (**f–i**) the same views as in (**a–d**) This 3-D reconstruction of ED and ES gated blood pool images (using the same views as **a–d**) shows a patient with an anterior, apical, and septal LV aneurysm. The *arrow* in (**i**) points to the dynamic base of the LV, where the distal aspects are essentially akinetic. This is not well appreciated in other views. (**j**) The ED and ES images in all views of this aneurysmal heart are shown in a single panel. (**k**) Shown is a reconstructed gated 3-D blood pool study in a patient with pre-excitation and a posterior septal bypass pathway in the LAO projection (*top*) and the posterior view (*bottom*). The sequential phase progression is sequentially highlighted in *white* from the upper left to lower right in each panel, as shown in the adjacent diagrams from *1* through *3*. In the *top panel*, the *white arrowheads* show the phase progression from the lateral left and right ventricular walls (*above*), progressing toward the middle of the image (*below*). However, in the *bottom* panel, the focus is really shown to be the posterior septum (*arrow*) [56]

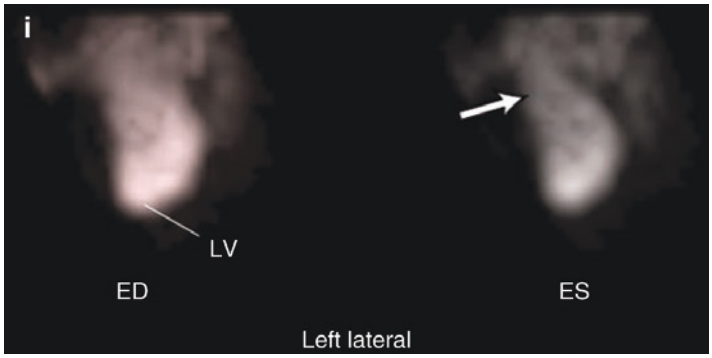

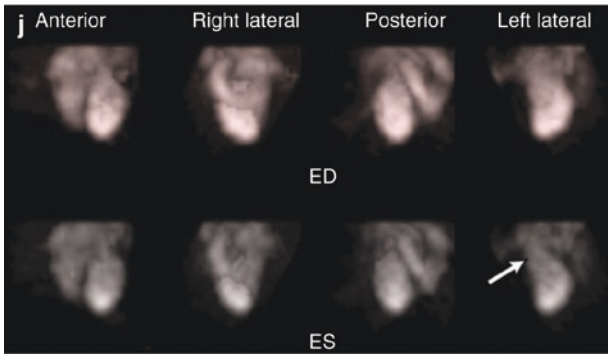

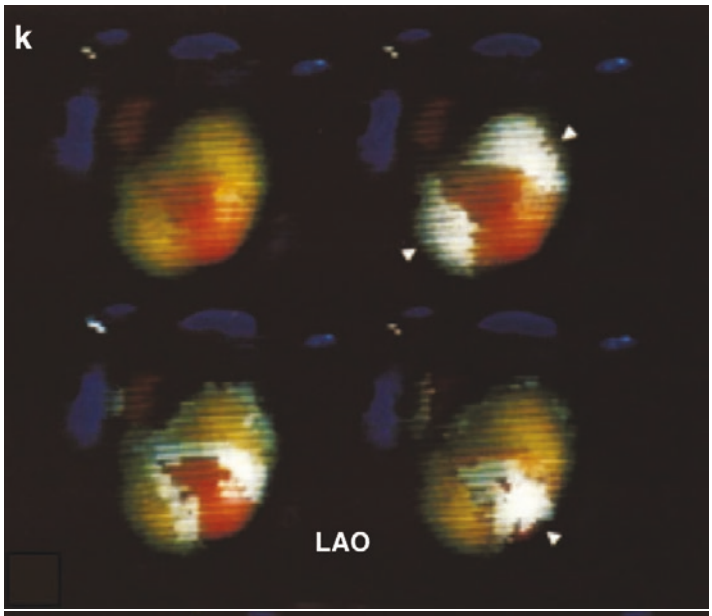

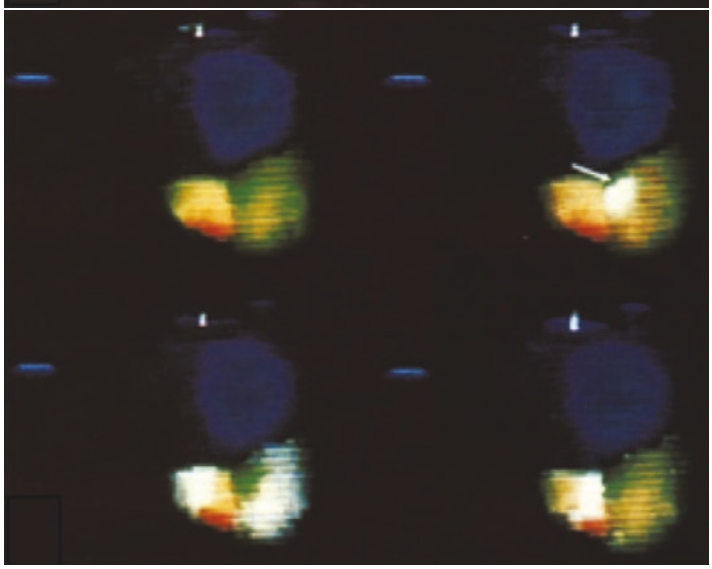

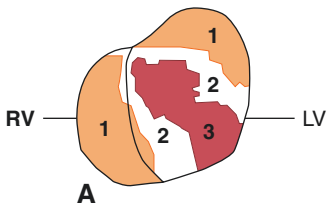

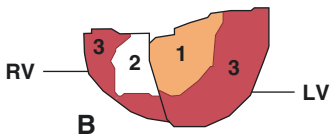

Fig. 7.40 (continued)

Gated Myocardial Perfusion SPECT

It is estimated that over 90% of myocardial perfusion SPECT studies performed in the USA in 2004 used ECG gating, which makes it possible to provide both perfusion and function information with a single radiopharmaceutical injection and a single acquisition sequence (Fig. 7.41). In our laboratory, we do not increase the injected dose or the acquisition time when gating a myocardial SPECT study: Typical parameters used are low-energy, high-resolution collimator(s), patient weight-based injection of 25–40 mCi of ^{99m}Tc-sestamibi/tetrofosmin or 3–4.5 mCi of ^{201}Tl, 3° spacing between adjacent projections, and 25-second (^{99m}Tc) or 35-second (^{201}Tl) acquisition time per projection [59]. The resulting total acquisition time can be as short as 12.5 minutes (^{99m}Tc) or 17.5 minutes (^{201}Tl) if a dual-detector camera with the detectors at a 90° angle is used.

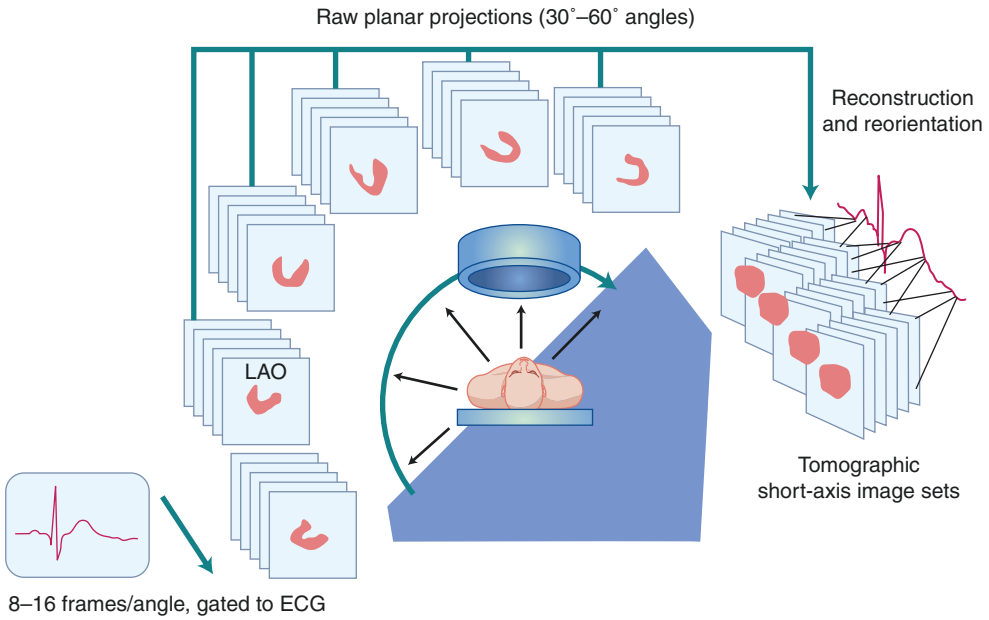

Fig. 7.41 Gated myocardial perfusion single-photon emission CT (*SPECT*): acquisition. A gated cardiac SPECT acquisition proceeds almost exactly like an ungated one: The camera detector(s) rotate around the patient, collecting projection images at equally spaced angles along a 180° or 360° arc. These projections are then filtered and reconstructed into tomographic short-axis and long-axis images [57, 58]. Gated SPECT imaging's distinguishing feature is that at each angle, several projection images (8, 16, or even 32) are acquired, each corresponding to a specific phase of the cardiac cycle. Reconstruction of all same-phase projections produces a three-dimensional "snapshot" of the patient's heart, frozen in time at that particular phase, and doing so for all phases results in four-dimensional image volumes (x, y, z, and time) from which cardiac function can be readily assessed [59]

Figures 7.42, 7.43, 7.44, 7.45, 7.46, and 7.47 demonstrate some clinical uses of phase images acquired by gated SPECT.

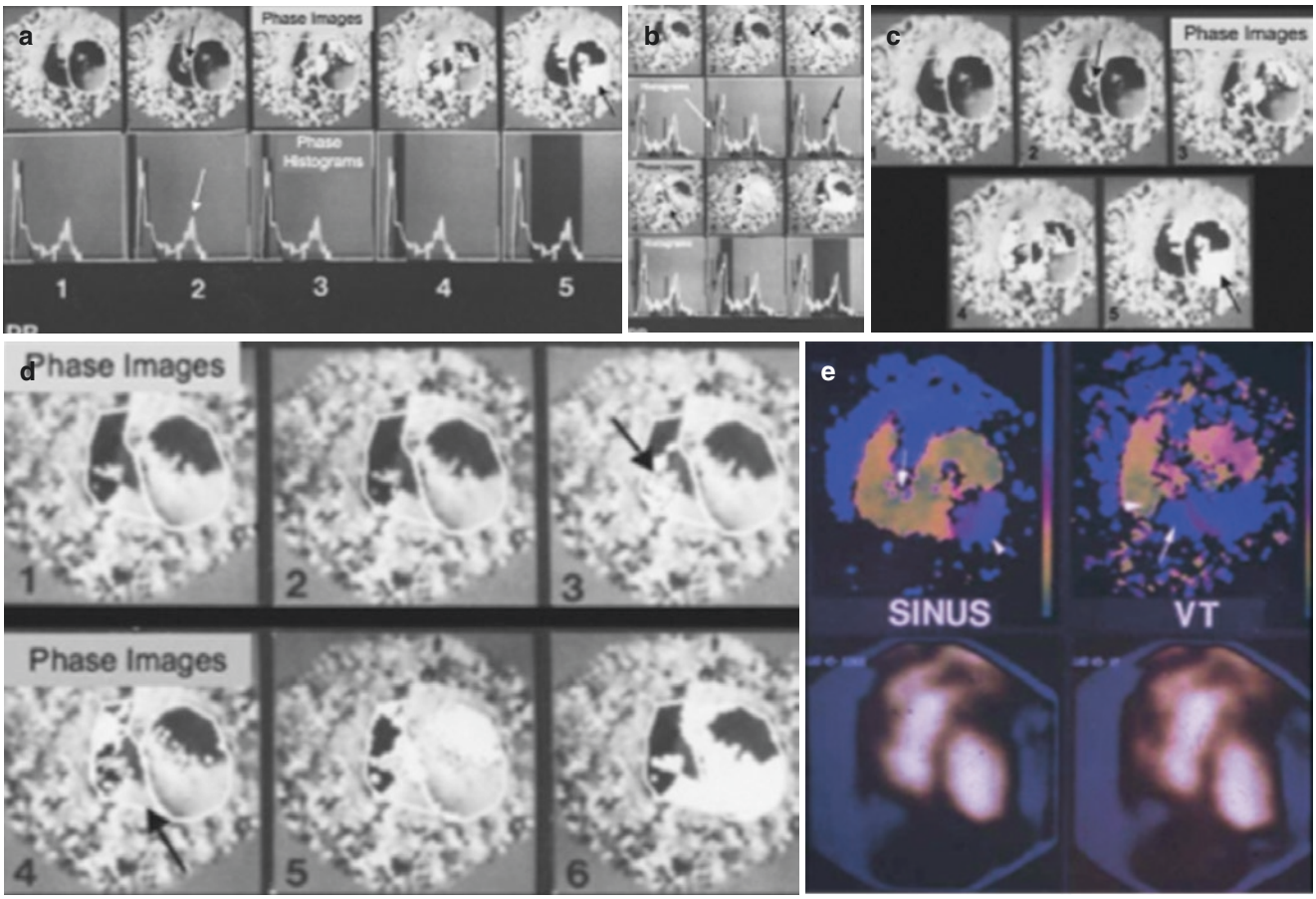

Fig. 7.42 Phase images in sinus rhythm (**a**) and ventricular tachycardia (VT) (**b**) in the "best-septal" LAO projection in a patient with VT. The phase images are displayed above their related LV (*white*) and RV (*black*) histograms, relating the phase angle, Ø, of each pixel, increasing from left to right on the abscissa, to the number of pixels with a given Ø, on the ordinate. The pixels with Ø spanned by the gray histogram sampling window are highlighted in white on the phase image, above. (**c**) and (**d**) are enlargements of the serially highlighted phase images shown in (**a**) and (**b**). In sinus rhythm (**a**), the earliest Ø is evident at the septal base (*black arrow*, panel 2) here projecting to the right, with an accompanying early LV site, a normal pattern. Initiation of both histograms is near simultaneous, but the late histogram peak of localized LVØ delay (*white arrow*, panel 2) corresponds to an apical aneurysm (*black arrow*, panel 5). In VT (**b**)**,** the RV histogram (*white arrow*, panel 2) precedes the LV. The earliest Ø is now in the distal RV, at sites highlighted in phase panels 2 and 3 (*black arrow*, phase panel 3). The late peaks on both histograms (*black arrows*, panel 3) correspond to an expanded LV aneurysm and a "new" RV apical aneurysm (*black arrow*, panel 4), distal to the VT exit site, which lies on its proximal border**.** (**e**) The lower panels present ungated blood pool images in the "best-septal" LAO projection for reference in interpreting the color phase images in sinus rhythm, sinus, and VT shown in preceding panels. These phase images present a color summary of sequential contraction, where the site of earliest Ø (in *green*) marks the septum and proximal RV (*arrow* in sinus rhythm), and the mid-RV in VT (*arrowhead*). The paradoxical motion of the apical LV aneurysm is featured in blue in sinus rhythm (*arrowhead*), and the new apical RV aneurysm is seen in blue in VT (*arrow*). Apical LV and RV scars, both supplied by an occluded left anterior descending coronary artery and a distal RV VT exit site, were confirmed at surgery. (From Botvinick et al. [60]; with permission from Springer Nature)

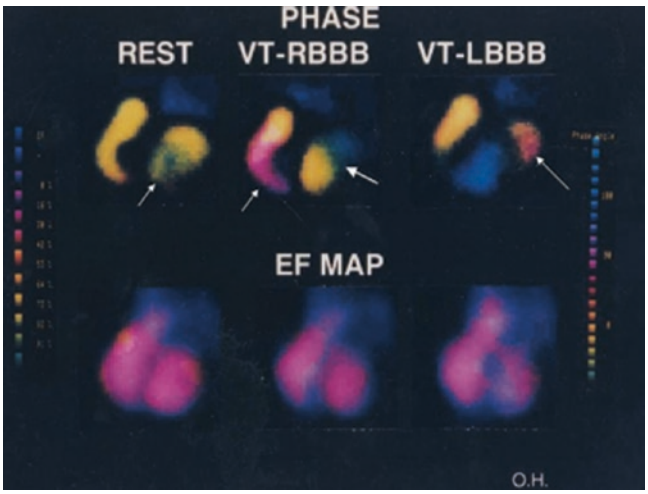

Fig. 7.43 Multiple VT exit sites: RBBB/LBBB patterns. Shown in the "best-septal" LAO projection are phase images acquired in a patient during sinus rhythm and during two different induced VT patterns, imaged at a similar rate, one with a RBBB and another with a LBBB. Below each phase image is the regional ejection fraction (EF) image, where ***green***, ***yellow***, and ***red*** indicate high values and ***blue*** **color** reflects akinetic to dyskinetic segments, as in the color scale at **right**. At rest, earliest Ø, ***green*** (***white arrow***) was confined to septal and adjacent LV regions with an RV contraction and conduction delay (***yellow***). On the related EF image, ventricular function is preserved only at the bases. The RBBB VT relates to a gross distal RV Ø delay, ***pink*** (***white arrow***), with earliest Ø at the mid- and basal LV, ***green-blue*** (***thick white arrow***), confirmed at electrophysiologic study. The function of both ventricles was modestly reduced. The LBBB VT related to a distal septal or RV apical exit site (***green***), with great delay in basal LV contraction, ***pink*** (***white arrow***). A gross Ø delay in the distal LV with aneurysm formation is evident in ***blue*** and on the EF image. (From Botvinick et al. [60]; with permission from Springer Nature)

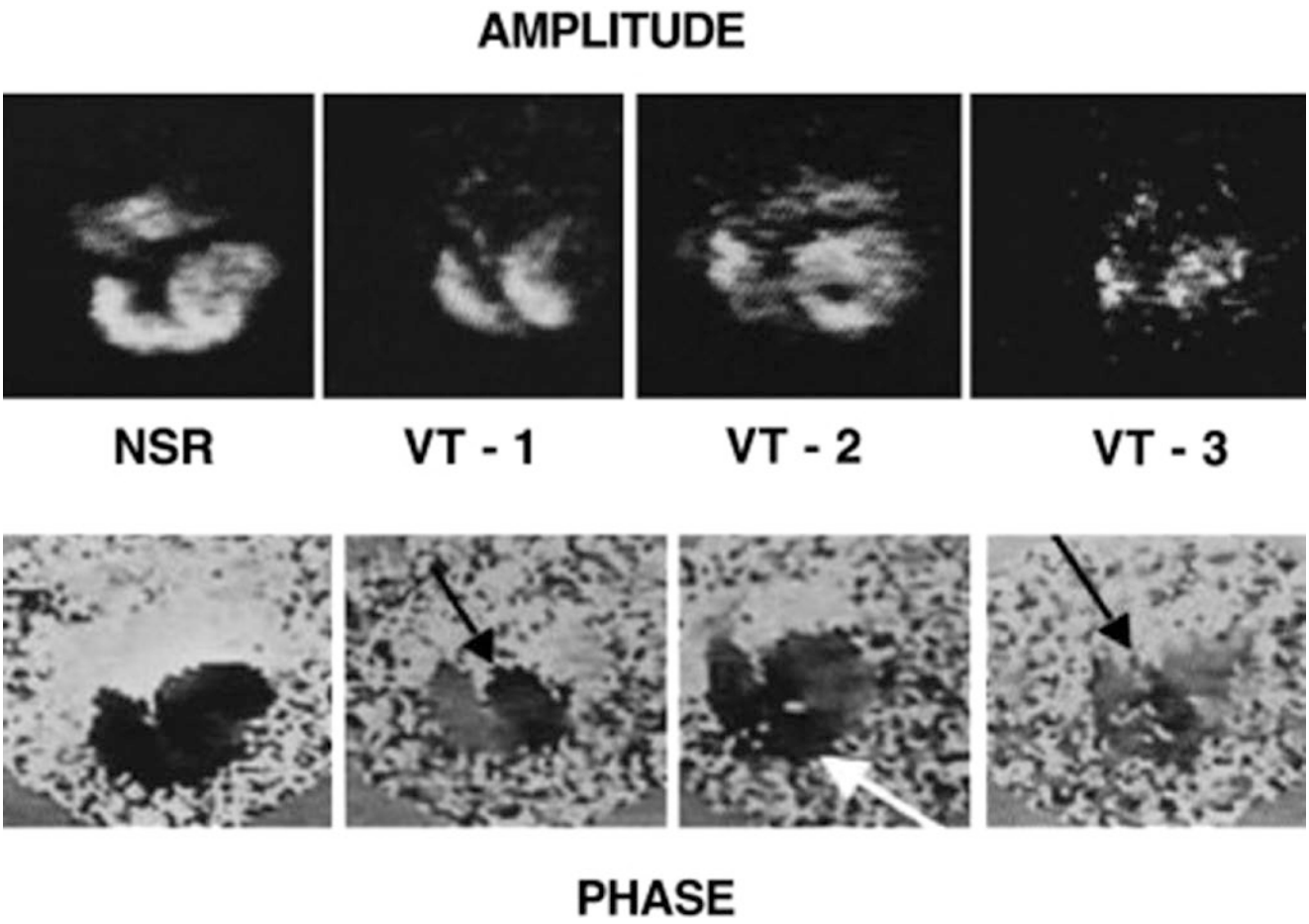

Fig. 7.44 Variable tolerance to multiple VT exit sites**.** Shown are the amplitude (*top row*), and the phase images (*bottom row*) generated from the equilibrium RNAs acquired in a patient in normal sinus rhythm (NSR) and with three VT exit sites, VT-1, VT-2, and VT-3. Intensity above is proportional to amplitude, and the phase image gray scale (*below*) parallels the contraction sequence. Regional amplitude and function were near normal in NSR; amplitude was moderately reduced with VT-1, with earliest Ø in the LV (*black arrow*), and an RBBB pattern; amplitude was well preserved with VT-2, with earliest Ø (*black*) in the RV (*white arrow*), and an LBBB pattern. The patient was intolerant to VT-3, with much-reduced amplitude and an LV septal exit site (*black arrow*), but with delayed RV and LVØ, seen in gray shades. The heart rate in each of these VT rhythms was similar. (From Botvinick et al. [60]; with permission from Springer Nature)

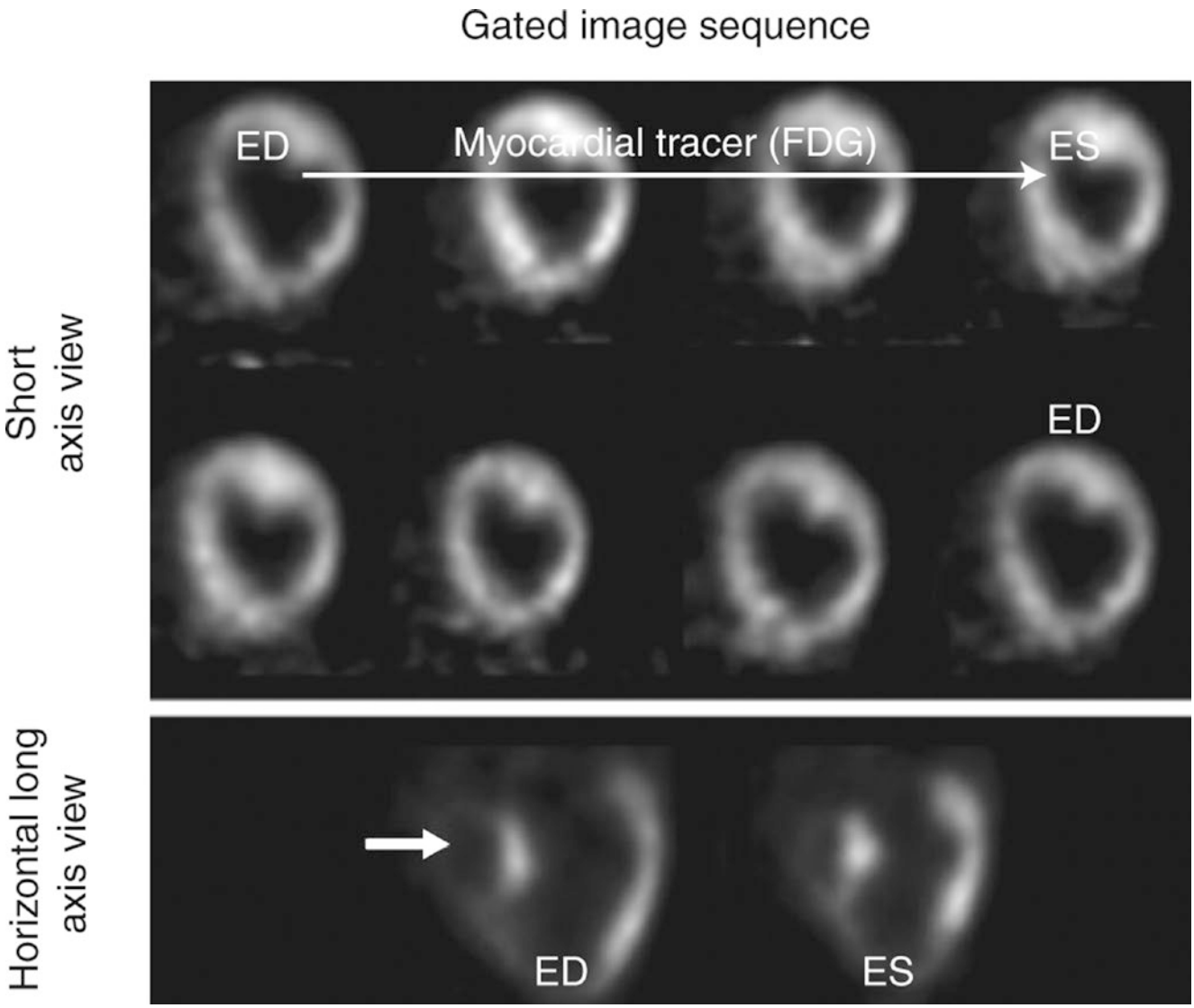

Fig. 7.45 Gated myocardial perfusion images. This sequence shows the gated set of eight images obtained from imaging a tracer that labels the myocardium, in this case ^{18}F-fluorodeoxyglucose (FDG). The small number of images and reduced sampling rate tends to slightly blur true end systolic (ES) with late systolic and early diastolic data, overestimating ES volume and underestimating ejection fraction. However, it has been shown that this effect on ejection fraction calculations is not too severe as long as the heart rate is not too low [40]. Using only eight images greatly distorts diastolic and systolic parameters such as peak ejection and filling rates, however. Note too the small right ventricle (*arrow*). ED end diastolic

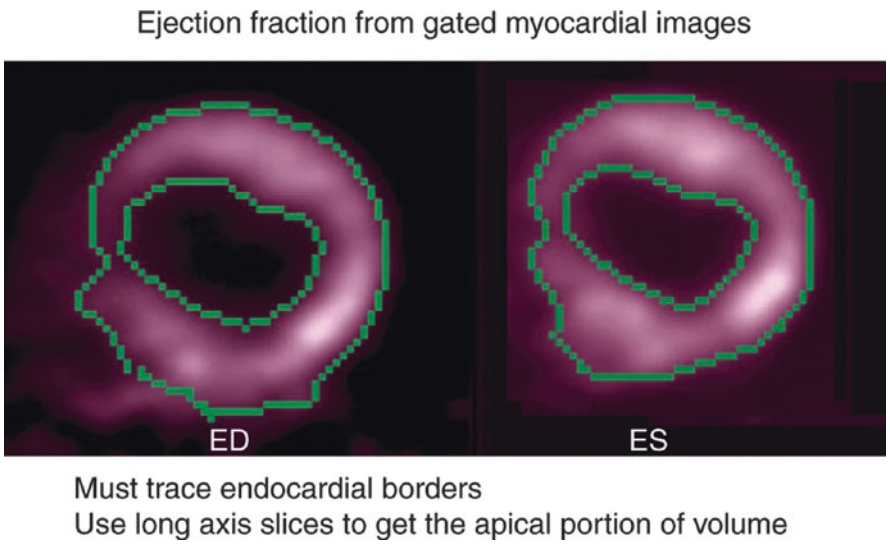

Fig. 7.46 Ejection fraction (EF) measurement. Left ventricular function can be computed from the series of gated myocardial uptake images to give a curve similar to that obtained from a gated blood pool study. Unfortunately, the resolution and noise of most SPECT perfusion studies is far worse than that shown in this gated FDG image sequence, leading to greater difficulties in accurately determining the endocardial edges and computing the EF. Unlike the gated blood pool images, counts are no longer proportional to blood volume. Instead, one must define the endocardial border from each image in the sequence for every slice, or at least end-diastolic (ED) and end-systolic (ES) frames for EF, and compute the volume from the sum of the enclosed areas of the endocardial surfaces. Short-axis slices do not give good endocardial border information near the apex, so long-axis views must also be used. This procedure has been successfully semiautomated in many commercial nuclear medicine cardiac analysis packages [16, 61]. However, the results one obtains depend to some extent on the resolution (as discussed below, regarding the partial volume effect) and noise in the images, so results can vary from one site to another and from one SPECT system to another [62]. Measurements from rest to stress should be more reliable, as the same filtering, imaging system, and other parameters are used for both. In the images shown here, the epicardial surface has also been outlined. LVEF calculated by gated myocardial perfusion SPECT was not significantly different from that of equilibrium RNA in the same 269 patients with a preserved LVEF. Myocardial perfusion SPECT lost accuracy with a small LV volume [63]

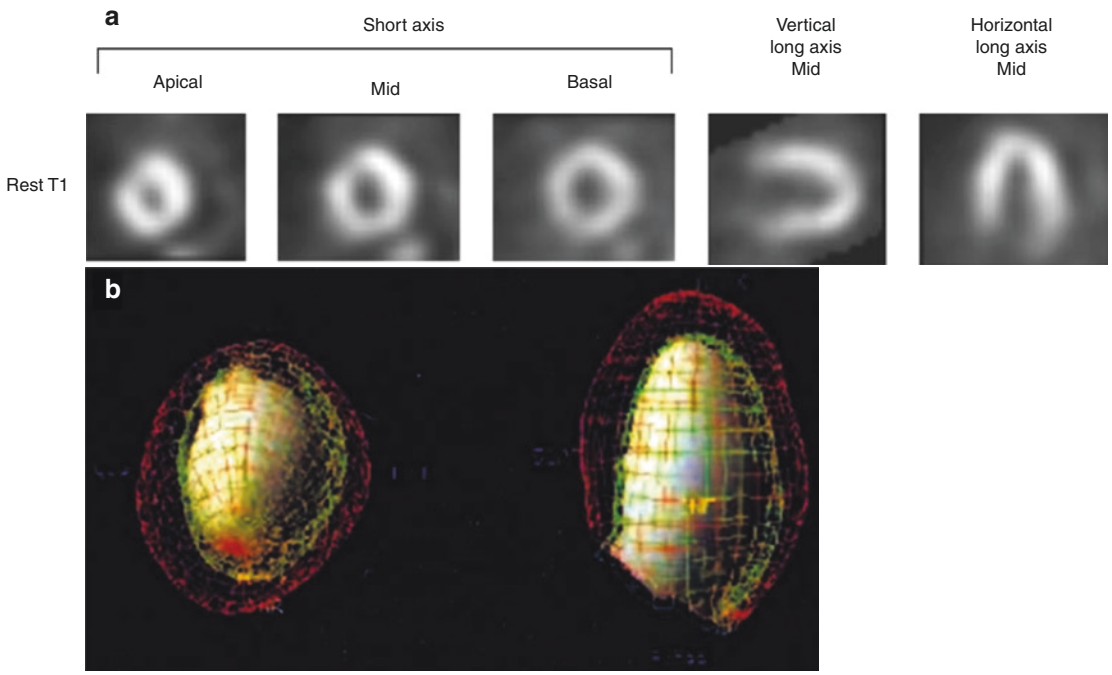

Fig. 7.47 (**a** and **b**) Display of left ventricular function. The epicardial and endocardial borders at end-diastolic (ED), end-systolic (ES), and the other points in the cardiac cycle can be put together to form the "wire cage" image as shown in this figure or even a pseudo-volumetric surface display. The epicardial and endocardial surfaces at ED are shown in *orange* and *yellow/green* in (**b**). The ES surface is shown in *gray*. Two different pseudo–3-D views are shown. These data were obtained from ^{99m}Tc-MIBI images; typical short-axis and long-axis images are shown in (**a**). Obviously, when there are severe perfusion defects, this methodology is problematic, and one must assume what the contours would have looked like had those segments of the myocardium been visible. Similarly, 3-D displays have been used to great effect in gated blood pool imaging [64–67]

Partial Volume Effect

Changes in myocardial wall thickening may be inferred from gated perfusion or metabolism images, using the so-called partial volume effect [68]. This term is somewhat misleading, in fact referring to two different phenomena that alter the relationship between image counts and intensity. The first effect is simply related to imaging an object using a scanner with less than perfect resolution. As demonstrated in Figure 7.48a, the effect becomes noticeable whenever the scanner resolution is comparable to the object being imaged. The second phenomenon related to partial volume effect is insufficient image sampling (Fig. 7.48b). Though insufficient sampling can be considered a separate phenomenon from the "partial volume effect," the consequences are quite similar. For example, systolic thickening translates into increased pixel intensity, and the contracting, thickening wall appears to brighten or move up the color scale in systole. Thickening or brightening then is gross evidence of regional myocardial viability, but cannot exclude a nontransmural infarction. The relationship between regional pixel intensity and thickening has been documented in phantoms and in correlations with echocardiography and MRI. Evidence of wall motion and thickening may be important for coronary disease diagnosis and appears to add to diagnostic specificity [69] from 84% to 92%, as motion and thickening in the presence of a "fixed" defect suggest an artifact of motion or attenuation rather than a true infarction [70].

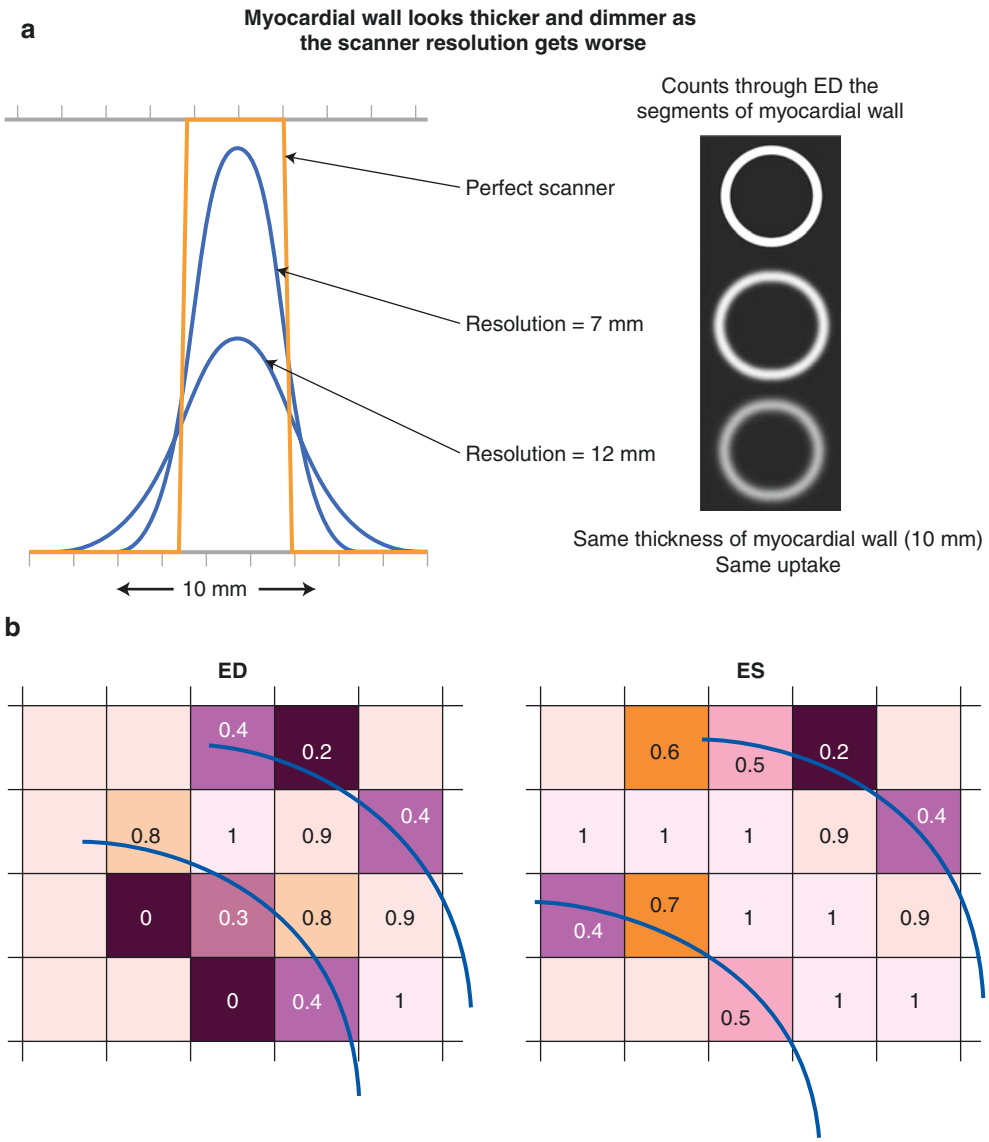

Fig. 7.48 Partial volume effect. (**a**) The *top right* image in is a simulated image of one short-axis slice of a 10-mm thick myocardial wall imaged at end diastole (ED) with a "perfect" scanner—that is, one with 0-mm resolution. The profile of counts through the line shown across the myocardial wall gives the square curve on the *left*. The width of this curve is exactly 10 mm. When the same myocardium is imaged with a scanner with a 7-mm resolution (typical of a PET scanner), the *middle right* image is obtained. It is somewhat blurrier and looks dimmer and wider, as shown on the corresponding profile on the *left*. Finally, when the 10-mm thick myocardial wall is imaged with a 12-mm full width at half-maximum scanner (typical of a very good SPECT scanner), the image at the *bottom right* results—still dimmer and apparently wider. In fact, all three images have the same total counts, the same "uptake" of tracer. As the resolution gets worse and worse, the counts get blurred more and more, giving the appearance of decreasing brightness and increasing width. If one were to add up all the counts under the three profiles, they would give exactly the same number of counts. (**b**) The second phenomenon related to partial volume effect is insufficient image sampling. Shown diagrammatically is a myocardial region in ED and end systole (ES) superimposed on a pixel grid in which only a small number of pixels span the myocardial wall (a situation typical of cardiac SPECT imaging). The *squares* represent pixels that are color-coded for and labeled with the percentage of the pixel occupied by the myocardium. Thickening brings a larger fraction of the pixels fully within the myocardial walls, producing a brighter (lighter) intensity response. Systolic thickening (for example, from 8 to 12 mm) translates into increased pixel intensity, and visually, the contracting, thickening wall appears to brighten or move up the color scale in systole [68]

Figure 7.49 illustrates a clinical application of the partial volume effect. In clinical imaging situations, the scanner has a fixed resolution, but the myocardial thickness changes with time, being thickest at end systole and thinnest at end diastole. This phenomenon suggests a method for measuring thickening [22, 23, 71]. The magnitude of the partial volume effect is determined by how poor the resolution of the scanner is compared with the thickness of the object being measured. Therefore, for a SPECT scanner with a 12-mm resolution, the partial volume effect will be less when the myocardial wall is 10 mm thick at end systole than when it is 5 mm thick at end diastole. Even though the uptake is the same, the partial volume effect will cause the thinner wall at end diastole to look dimmer, whereas the thicker wall at end systole shows minimal partial volume effect, so the uptake will appear brighter. Thus, the increase in brightness is an indication that the wall is thickening, but the degree of thickening may not be linearly related to the amount of brightening. If the myocardial wall at end systole is much thicker than the resolution, the partial volume blurring effect will be small and little brightening will occur. Therefore, although brightening always indicates thickening, a lack of brightening does not necessarily indicate that no thickening is occurring. This must be kept in mind when clinical interpretations of brightening are made.

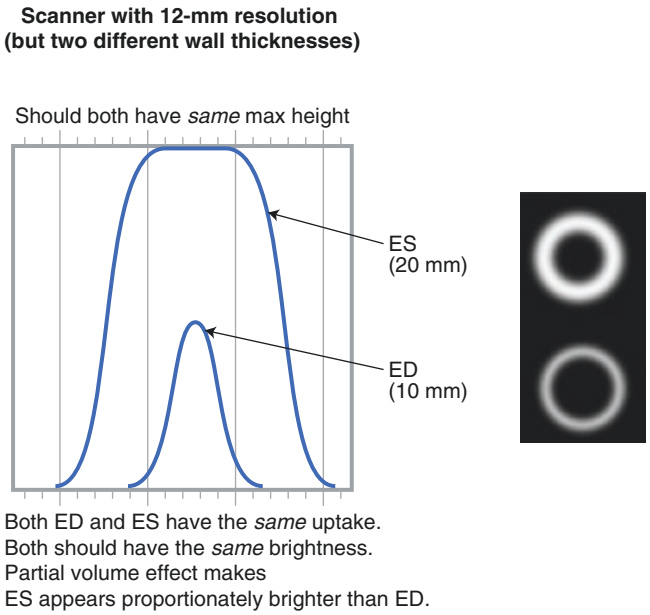

Fig. 7.49 Clinical application of the partial volume effect. The magnitude of the partial volume effect is determined by how poor the resolution of the scanner is compared with the thickness of the object being measured, so the effect will be less for a thicker myocardial wall at end systole (ES) than when the wall is thinner, at end diastole (ED). Even though the uptake is the same, the partial volume effect will cause the thinner wall at ED to look dimmer. Note that when the myocardial wall at ED is much thicker than the resolution (e.g., 20 mm or more), the partial volume blurring effect will be small and little brightening will occur between ED and ES, even though the wall does thicken

Figure 7.50 presents a clinical example of how the partial volume effect can be used to indicate whether thickening is occurring. It is important to remember that brightening always indicates thickening, but lack of brightening does not necessarily indicate that no thickening is occurring. This, as well as the related causes of thickening in the absence of brightening, must be kept in mind when clinical interpretations of brightening are made [72]. Figure 7.51 shows an example of brightening, a result of a partial volume effect, that is correlated with myocardial thickening.

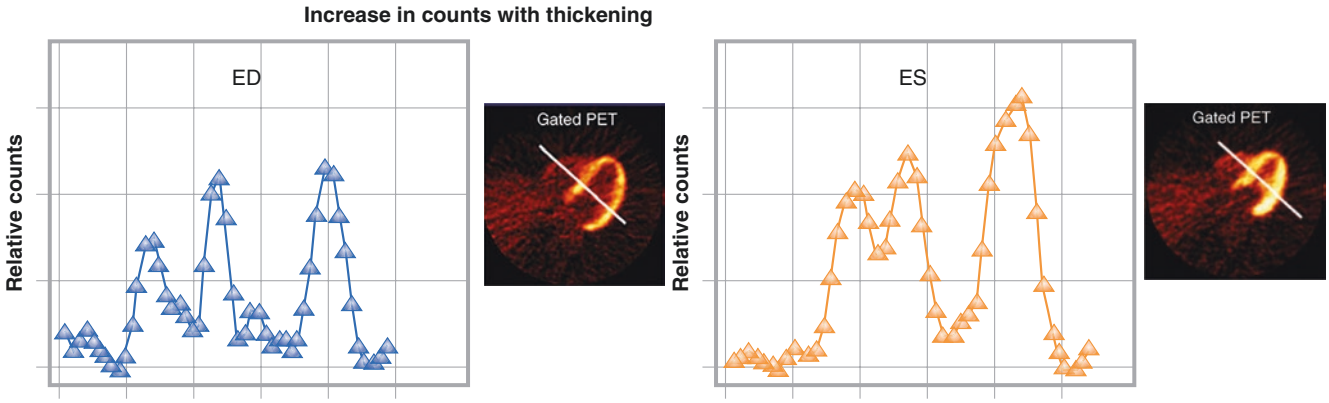

Fig. 7.50 Myocardial thickening. A clinical example of how the partial volume effect can be used to indicate whether thickening is occurring is illustrated here. The *upper left* image shows a transaxial myocardial uptake image, in this case [^{18}F]-FDG at end diastole (ED). The curve below this image is the profile of counts through the line shown in the image. The *upper right* image is the same transaxial slice, but at end systole (ES). Again, the profile through the image, as indicated, is shown below. Note that the myocardial walls in the ES image appear uniformly brighter than in the ED image, and this increase in brightness is clearly shown in the profiles. The brightness is a definitive indication that thickening has occurred. Note that the right ventricular wall also shows an increase in counts. This is clearly seen in the profile of counts, but is harder to appreciate visibly in the image

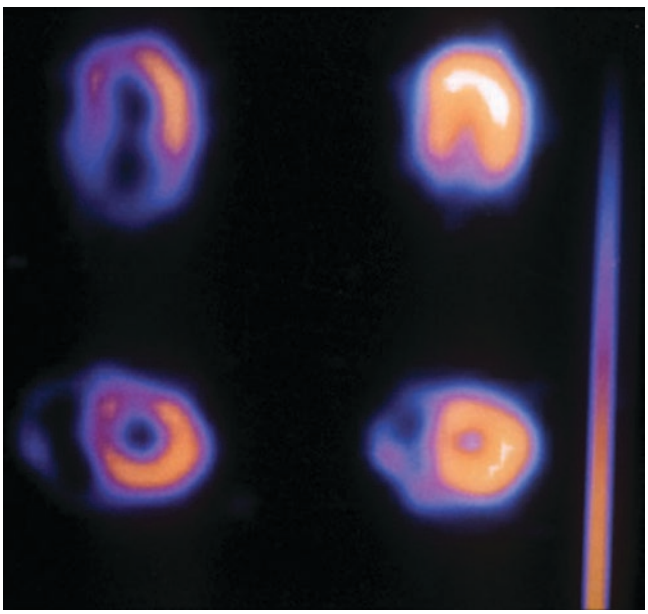

Fig. 7.51 Gated perfusion imaging. End-diastolic (*left*) and end-systolic (*right*) gated ^{99m}Tc-sestamibi perfusion images in a normal heart in selected short-axis (*top*) and horizontal long-axis (*bottom*) SPECT slices. Inward systolic motion is evident, as well as brightening, or increased intensity, during systole. The brightening, a result of a partial volume effect, is well correlated with myocardial thickening

Although the partial volume effect can be useful to determine whether thickening is occurring, it also can cause difficulties in myocardial perfusion imaging, as summarized in Table 7.6. Myocardial walls that are thin compared with the resolution of the system will appear to have less activity than they really do. The reader of an FDG scan may erroneously think that the region is nonviable, when in reality it is just thin. Similarly, if it is a perfusion scan, thin walls will erroneously appear to have reduced perfusion. If one compares two studies taken some months apart and a portion of the myocardial wall has thinned, that portion will erroneously appear to have less uptake. Of course, wall thinning is related to infarction and scar, which are also causes of reduced perfusion and uptake. Similarly, owing to their different physical properties and related associated spatial resolution, the same myocardial wall could appear broader with different intensity and erroneously appear to have relative less activity when imaged by ^{201}Tl compared with ^{99m}Tc radiotracers. All these factors must be taken into consideration when interpreting scans of myocardial uptake.

Thin myocardial walls may erroneously appear to be nonviable in FDG imaging.
Thin myocardial walls erroneously appear to have lower perfusion for ^{201}Tl and sestamibi or other perfusion agents.
Walls imaged with ^{201}Tl erroneously appear to be thicker with lower perfusion, compared with walls imaged with ^{99m}Tc perfusion agents.
Changes in myocardial thickness may make it appear that activity has changed.

Table 7.6 Partial volume effect: ambiguities and misleading effects

Gated Perfusion Imaging

Functional data may be derived from the perfusion study by either first-pass or postlocalization gated methods. As noted on Table 7.7, the first-pass method is more demanding of technique, instrumentation, and time, but it is based on a long-established method and generates a long-validated calculation of LVEF. Owing to its inconvenience and the availability of established functional data after gated imaging, first-pass acquisition is rarely performed. Equilibrium RNA is performed primarily to calculate accurate measures of ventricular function. Gated myocardial perfusion studies do provide information regarding left ventricle wall motion and LVEF, but they are performed to assess myocardial perfusion and viability. Their functional information serves as an important supplement to perfusion information, but they are never used when the primary study objective is to assess ventricular function. Their evolving application to synchrony assessment is an exception to this rule, and the gated perfusion method will gain use only as it demonstrates superiority and cost-effectiveness over other methods.

First-pass method
Needs ^{99m}Tc-based agents
Needs state-of-the-art, high-sensitivity cameras (detectors)
Performed with radionuclide administration
Can be performed with stress, but not always possible
May be performed with rest and stress
Left ventricular wall motion, volumes, and ejection fraction
Can provide right ventricular ejection fraction and wall motion
Evaluates features of background-free blood pool
Gated myocardial perfusion studies
May be performed with ^{201}Tl or ^{99m}Tc-based agents
Uses conventional cameras
Always delayed after radionuclide injection and after stress
May be performed with rest and stress
Left ventricular wall motion, volumes, and ejection fraction
Assesses left ventricular wall thickening
Accuracy dependent on endothelial border definition
Technical considerations in gated SPECT perfusion imaging
Acquisition and reconstruction of a 16-frame gated SPECT study requires 16 times as much RAM and takes 16 times as long for reconstruction.
For clinical utility, gated SPECT perfusion imaging needs a fast computer with 8 Mb of RAM and 500 Mb of hard disk space.
Requirements for vendor software:
Permit acquisition of up to 16-frame SPECT
Display time at each camera stop in seconds or in accepted beats within a user-defined R–R interval
Permit collapse of the study to an ungated study or image including only specified frames (e.g., an end-diastolic image)
Display dynamic beating short-axis slices, selected long-axis slices, and three-dimensional rendering of the beating heart
Calculate quantitative measures of regional perfusion, contraction, and wall thickening

Table 7.7 Comparison of Perfusion Methods and Technical Considerations for the Evaluation of Ventricular Function

Figures 7.52, 7.53, 7.54, 7.55, 7.56, 7.57, and 7.58 provide examples of the use of gated perfusion imaging.

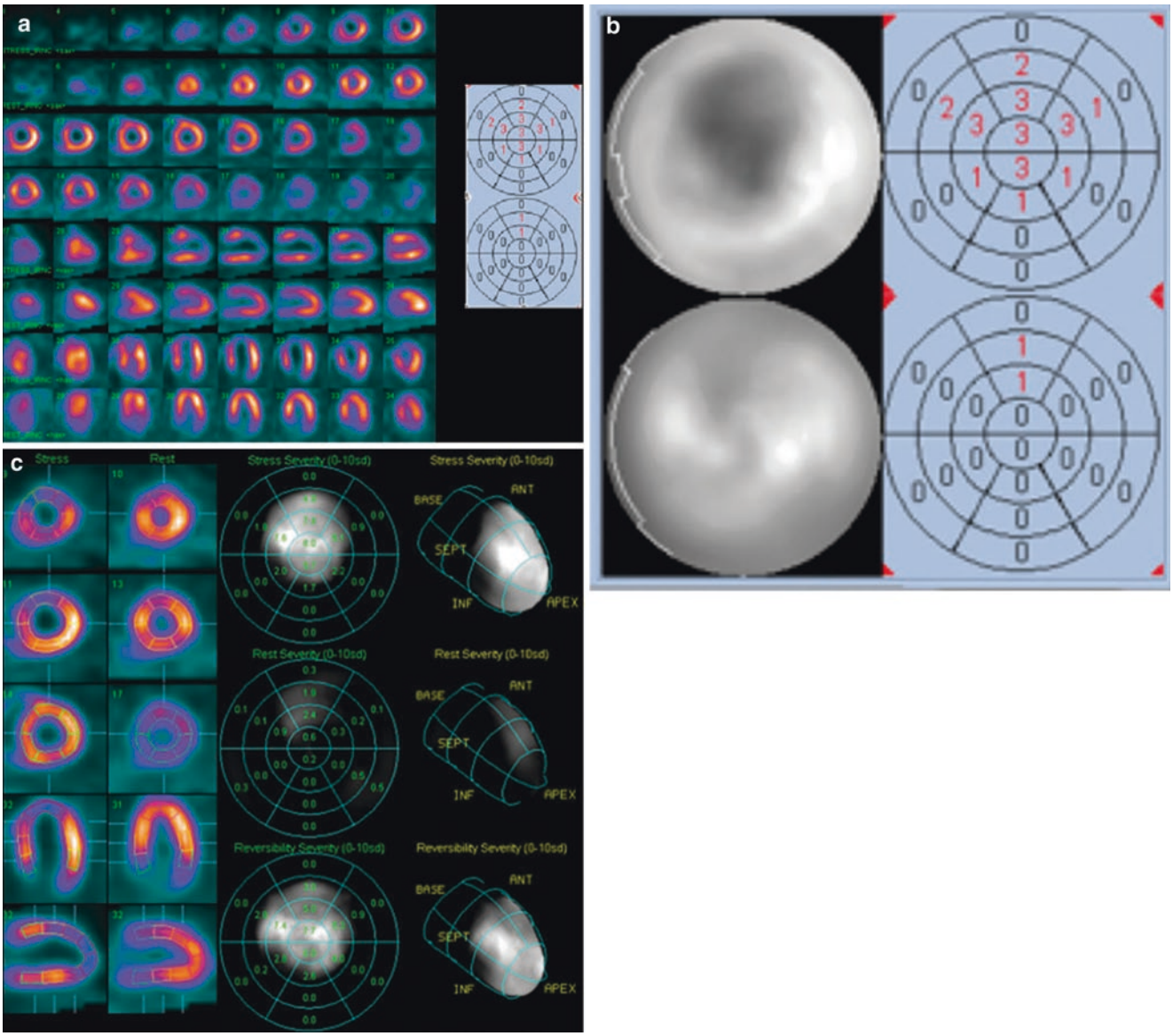

Fig. 7.52 Gated stress perfusion imaging. (**a**) Shown in the *top row* and continuing in the *third row*, from apex (*left*) to base (*right*), are color-coded SPECT stress perfusion images in a 49-year-old man with atypical chest pain and an equivocal stress test result. Images were performed with the dual-isotope ^{201}Tl rest, ^{99m}Tc stress protocol. In the *second* and *fourth rows* are the rest images in the same patient, acquired at baseline. Below these images, in alternating rows from top down, are stress and rest images in the same patient presented in vertical long axis, *left to right*, from the septum to the lateral wall, and the horizontal long axis, *left to right*, from the inferior to anterior walls. Cavitary dilatation with a gross, reversible, apical, anterior, and septal defect is evident, consistent with significant flow-limiting disease in the left anterior descending coronary artery. The summed stress score of 20 confirms the high related coronary risk. (**b**) Shown is the quantitative perfusion SPECT or quantitative perfusion AutoQuant (Cedars Sinai Hospital, Los Angeles, CA) display, with the *left panel* showing segmented stress slices, above, at the *far left*, followed by rest slices, below, and polar maps in the *right panels*, with stress above and rest below. Here the display is calibrated for the percentage of relative regional intensity. In the *right panel*, a color-coded defect is painted on a model left ventricle. (**c**) This display is similar to (**b**) but now shows, from top down, stress, rest, and difference polar maps with intensity scaled to the standard deviation derived from the normal rest–stress male activity distribution using this dual-isotope protocol. (**d**) Models of the epicardium (*orange mesh*) and endocardium at end diastole (*green mesh*) and at end systole (*solid orange*) in the anterior (*left*) and left lateral (*right*) projections taken from the gated myocardial perfusion images in this case at peak stress. Evident is anterior, apical, and septal wall motion abnormalities. Rest function was normal. Evidence of stress-induced dysfunction adds significant prognostic risk to any perfusion abnormalities induced. ANT anterior, INF inferior, SEPT septal

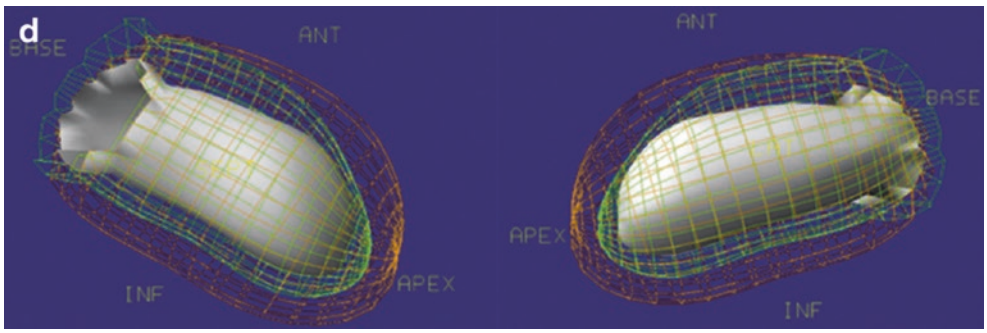

Fig. 7.52 (continued)

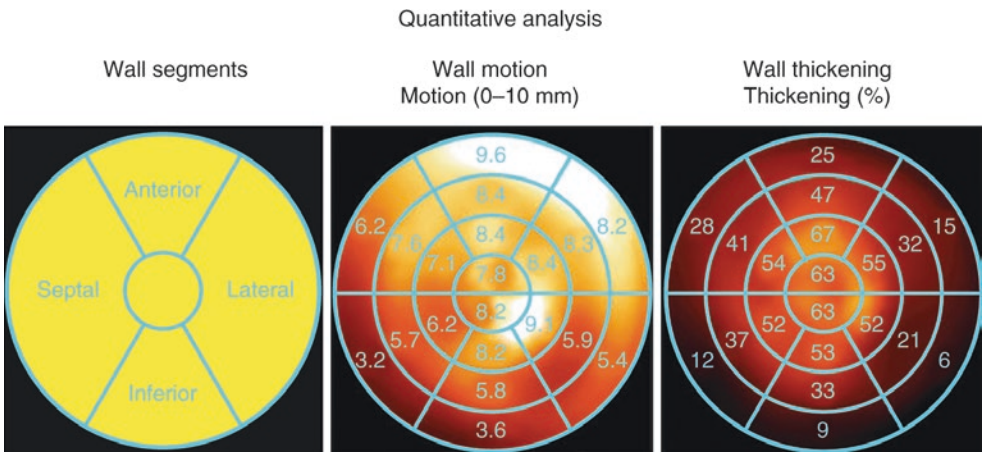

Fig. 7.53 Normal quantitative wall motion and thickening on gated perfusion imaging. Shown are AutoQuant (Cedars Sinai Hospital, Los Angeles, CA) polar maps demonstrating wall segments (*left*), normal wall motion (*center*), and normal wall thickening (*right*) [74]. Thickening is accurately measured as a percentage increase from end diastole by the linear relationship to the percentage increase in wall intensity. (From Yun et al. [74]; with permission from Wolters Kluwer)

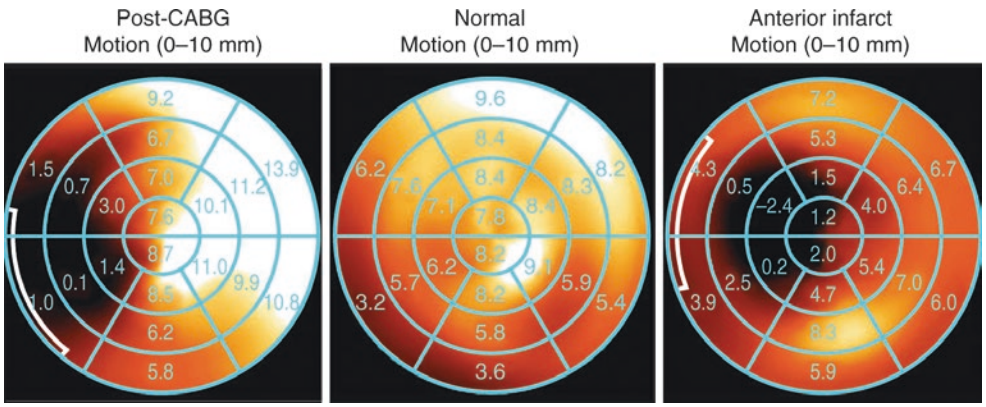

Fig. 7.54 Abnormal quantitative wall motion on gated perfusion imaging. Shown are AutoQuant (Cedars Sinai Hospital, Los Angeles, CA) polar maps demonstrating wall motion patterns in a patient after coronary artery bypass graft (CABG) surgery (*left*), in a normal patient (*center*), and in a patient with a prior anterior infarction (*right*). Abnormal septal wall motion is evident in the post-CABG and postinfarct patients. (From Yun et al. [74]; with permission from Wolters Kluwer)

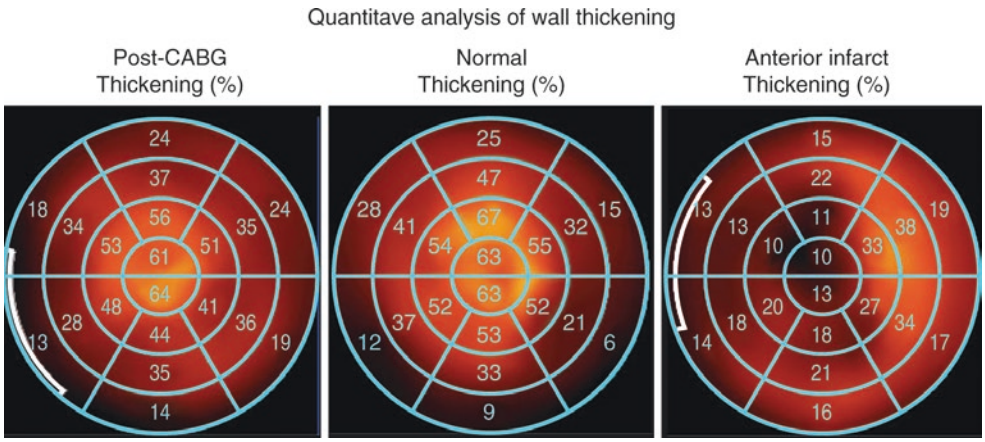

Fig. 7.55 Abnormal quantitative wall thickening on gated perfusion imaging. Shown are AutoQuant (Cedars Sinai Hospital, Los Angeles, CA) polar maps demonstrating wall thickening patterns in the same three patients as in Fig. 7.54: after coronary artery bypass graft (CABG) surgery (*left*), in a normal patient (*center*), and in a patient with a prior anterior infarction (*right*). Abnormal septal and apical wall thickening is evident only post-infarction. The abnormal wall motion after CABG is not accompanied by abnormal thickening because there is no intrinsic wall pathology. The abnormal wall motion post-CABG relates to the absence of the pericardial restraint, with a resulting anterior swing of the epicardium, seen on dynamic images, (From Yun et al. [74]; with permission from Wolters Kluwer)

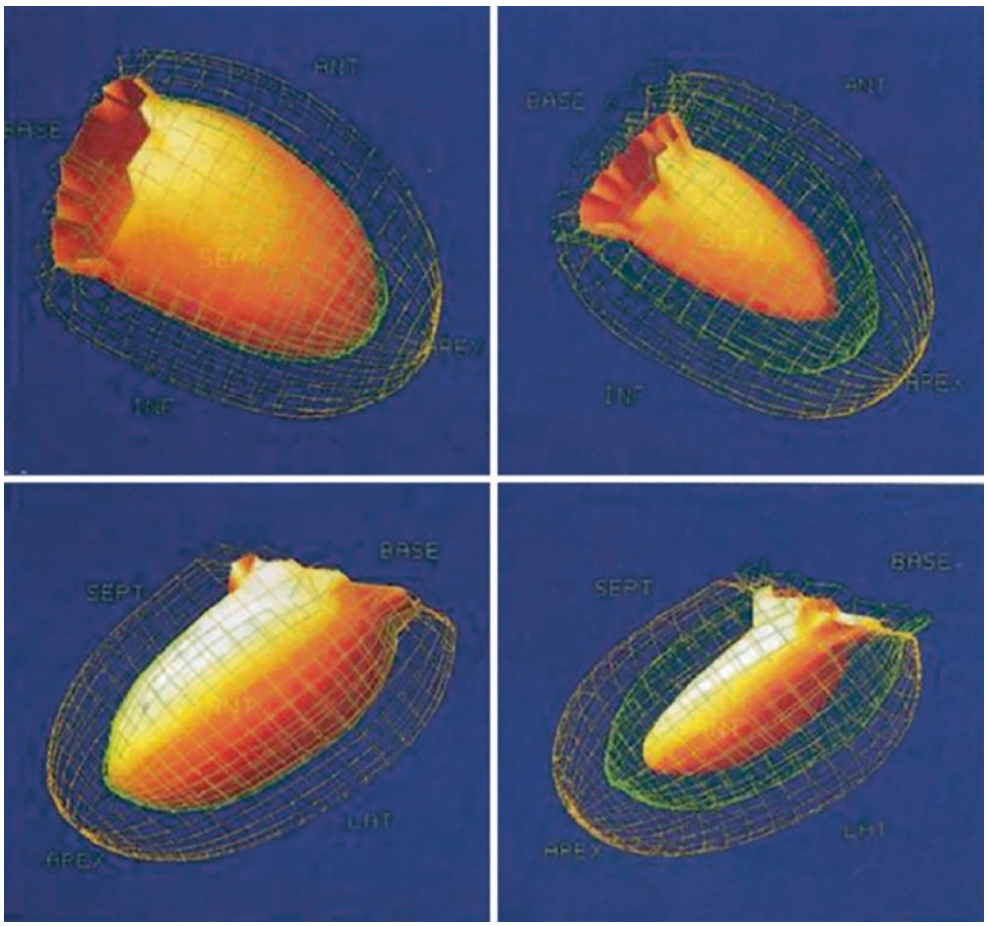

Fig. 7.56 Normal wall motion and thickening: ventricular model. Shown on the AutoQuant (Cedars Sinai Hospital, Los Angeles, CA) display of gated perfusion images is normal wall motion and thickening in anterior (*top*) and lateral (*bottom*) projections. End-diastolic frames are on the *left* and end-systolic frames are on the *right*. Here, again, the epicardium is represented by the *green mesh*, the endocardium at end diastole is the *orange mesh*, and the endocardium at end systole (*right*) is the *solid orange* surface. Note the symmetrical inward motion of the endocardium. (From Yun et al. [74]; with permission from Wolters Kluwer)

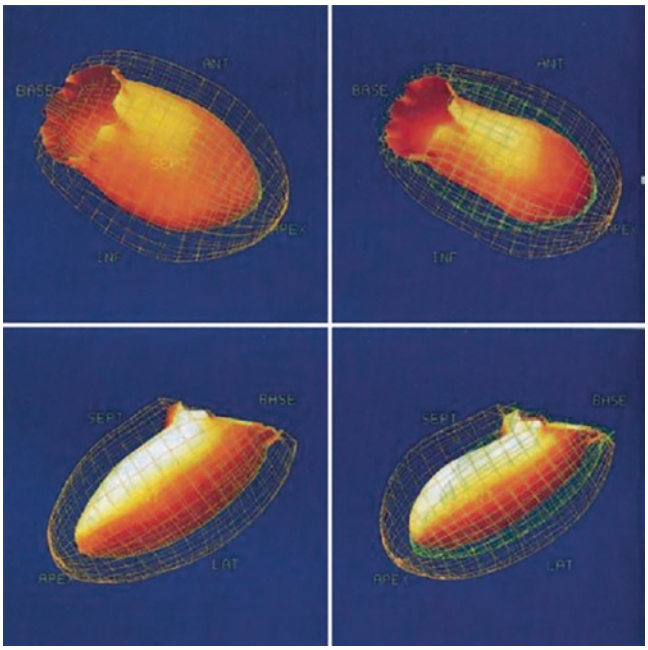

Fig. 7.57 Abnormal wall motion and thickening with anterior infarction: ventricular model. Shown on the same AutoQuant (Cedars Sinai Hospital, Los Angeles, CA) display of gated perfusion images is akinesis of the apex, septum, and distal anterior wall in anterior (*left*) and lateral (*right*) projections in a patient with a prior anterior myocardial infarction. The perfusion image showed a dense anterior, septal, and apical defect. (From Yun et al. [74]; with permission from Wolters Kluwer)

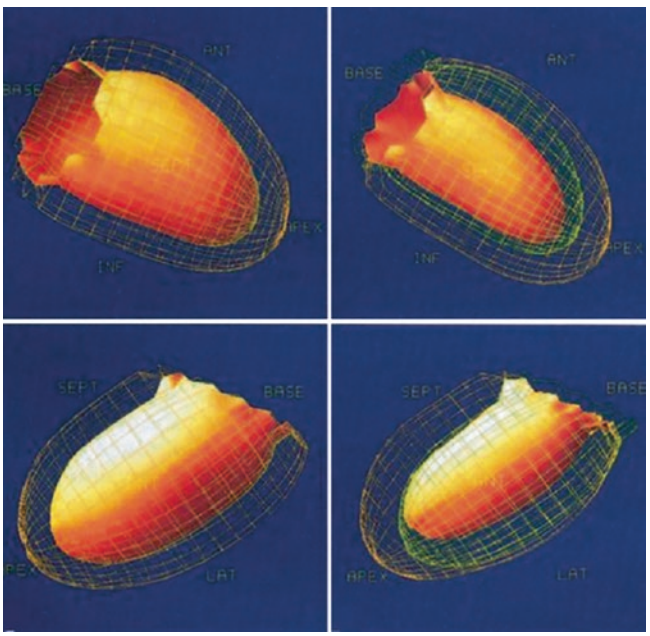

Fig. 7.58 Anterior swing after coronary artery bypass graft (CABG): ventricular model. Shown on the same AutoQuant (Meyer Instruments, Houston, TX) display of gated perfusion images as the prior figures is the pattern of abnormal wall motion seen after CABG or any cardiac surgery in the anterior (*left*) and lateral (*right*) projections. Here, the anterior swing of the epicardium is well seen in the lateral projection, where the septum appears to be akinetic but demonstrates normal wall thickening and is associated with preserved anterior wall motion, differentiating this pattern from that seen in patients after an anterior infarction. (From Yun et al. [74]; with permission from Wolters Kluwer)

References

1. Hoffmann G, Klein N. Die methode der radiokardiographischen funktions analyse. Nuklearmedizin. 1968;7:350–70.
2. Strauss HW, Zaret BL, Hurley PJ. A scintiphotographic method for measuring left ventricular ejection fraction in man without cardiac catheterization. Am J Cardiol. 1971;28:575–80.
3. Zaret BL, Strauss HW, Hurley PJ. A noninvasive scintiphotographic method for detecting regional ventricular dysfunction in man. N Engl J Med. 1971;284:1165–70.
4. Parker JA, Secker-Walker R, Hill R. A new technique for the calculation of left ventricular ejection fraction. J Nucl Med. 1972;13:649–51.
5. Green MV, Ostrow HG, Douglas MA, Myers RW, Scott RN, Bailey JJ, Johnston GS. High temporal resolution ECG-gated scintigraphic angiocardiography. J Nucl Med. 1975;16:95–8.
6. Steele P, Kirch D, LeFree M, Battock D. Measurement of right and left ventricular ejection fractions by radionuclide angiocardiography in coronary artery disease. Chest. 1976;70:51–6.
7. Bacharach SL, Green MV, Borer JS. A real-time system for multiimage gated cardiac studies. J Nucl Med. 1977;18:79–84.
8. Borer JS, Bacharach SL, Green MV. Real-time radionuclide cineangiography in the noninvasive evaluation of global and regional left ventricular function at rest and during exercise in patients with coronary-artery disease. N Engl J Med. 1977;296:839–44.
9. Freedman NMT, Bacharach SL, Cuocolo A, et al. ECG gated PET C-11 monoxide studies: an answer to the "background" question in planar Tc-99m gated blood pool imaging. J Nucl Med. 1992;33:938.
10. Boyd HL, Gunn RN, Marinho NV, Kanwatowski SP, Bailey DL, Costa DC, et al. Non-invasive measurement of left ventricular volumes and function by gated positron emission tomography. Eur J Nucl Med. 1996;23:1594–602.
11. Fischman AJ, Moore RH, Gill JB, Strauss HW. Gated blood pool tomography: a technology whose time has come. Semin Nucl Med. 1989;19:13–21.
12. Underwood SR, Walton S, Laming PJ, Jarritt PH, Ell PJ, Emanuel RW, Swanton RH. Left ventricular volume and ejection fraction determined by gated blood pool emission tomography. Br Heart J. 1985;53:216–22.
13. Ishino Y. Assessment of cardiac function and left ventricular regional wall motion by ^{99m}Tc multigated cardiac blood-pool emission computed tomography. Kaku Igaku. 1992;29:1069–81.
14. Bartlett ML, Srinivasan G, Barker WC, Kitsiou AN, Dilsizian V, Bacharach SL. Left ventricular ejection fraction: comparison of results from planar and SPECT gated blood-pool studies. J Nucl Med. 1996;37:1795–9.
15. Borer J, Supino P. Radionuclide angiography part II: equilibrium imaging. In: Iskandrian AE, Verani MS, editors. Nuclear cardiac imaging: principles and applications. New York: Oxford University Press; 2003. p. 323–67.
16. Botvinick EH, O'Connell JW, Kadkade PP, Glickman SL, Dae MW, Cohen TJ, et al. Potential added value of three-dimensional reconstruction and display of single photon emission computed tomographic gated blood pool images. J Nucl Cardiol. 1998;5:245–55.
17. Gill JB, Moore RH, Tamaki N, Miller DD, Barlai-Kovach M, Yasuda T, et al. Multigated blood-pool tomography: new method for the assessment of left ventricular function. J Nucl Med. 1986;27:1916–24.
18. Groch MW, Marshall RC, Erwin WD, Schippers DJ, Barnett CA, Leidholdt EM Jr. Quantitative gated blood pool SPECT for the assessment of coronary artery disease at rest. J Nucl Cardiol. 1998;5:567–73.
19. Groch MW, Marshall RC, Schippers D, et al. Three dimensional analysis of gated blood pool SPECT: applicability of multiple reference models. J Nucl Med. 1998;39:45P–145.
20. Germano G, Kavanagh PB, Wachter P. A new algorithm for the quantitation of myocardial perfusion SPECT. J Nucl Med. 2000;41:712–9.
21. Bartlett ML, Buvat I, Vaquero JJ, Mok D, Dilsizian V, Bacharach SL. Measurement of myocardial wall thickening from PET/SPECT images: comparison of two methods. J Comput Assist Tomogr. 1996;20:473–81.
22. Cooke CD, Garcia EV, Cullom SJ, Faber TL, Pettigrew RI. Determining the accuracy of calculating systolic wall thickening using a fast Fourier transform approximation: a simulation study based on canine and patient data. J Nucl Med. 1994;35:1185–92.
23. Garcia E, Bacharach SL, Mahmarian JJ, et al. Imaging guidelines for nuclear cardiology procedures: part 1. J Nucl Med. 1996;3:G3–46.
24. Botvinick EH. Editor. Topic 7, radionuclide angiography: equilibrium and first pass methods. Self-study program III. In: Botvinick E, editor. Nuclear medicine: cardiology. Society of Nuclear Medicine: Reston, VA; 2007.
25. Botvinick EH, Glazer H, Shosa D. What is the relationship and utility of scintigraphic methods for the assessment of ventricular function? Cardiovasc Clin. 1983;13:65–78.
26. Bodenheier MM, Banka FS, Fooshee CM. Quantitative radionuclide angiography in the right anterior oblique view: comparison with contrast ventriculography. Am J Cardiol. 1978;41:718–25.
27. Marshall RC, Berger HJ, Costin JC. Assessment of cardiac performance with quantitative radionuclide angiocardiography. Circulation. 1977;56:820–9.
28. VanDyke D, Anger HO, Sullivan RW. Cardiac evaluation from radioisotope dynamics. J Nucl Med. 1972;13:585–92.
29. Bacharach SL, Green MV, Borer SJ. Instrumentation and data processing in cardiovascular nuclear medicine: evaluation of ventricular function. Semin Nucl Med. 1979;9:257–74.
30. Wackers JF. New horizons for myocardial perfusion imaging with technetium-99m labeled isonitrile. In: Pohost GM, Higgins CB, Nanda NC, et al., editors. New concepts in cardiac imaging. Chicago: Year Book Medical Publishers; 1989. p. 93–108.
31. Upton MT, Rerych SK, Newman GE, Port S, Cobb FR, Jones RH. Detecting abnormalities in left ventricular function during exercise before angina and ST-segment depression. Circulation. 1980;62:341–9.
32. Udelson JE, Dilsizian V, Bonow RO. Nuclear cardiology. In: Libby P, Zipes DP, Mann DL, Bonow RO, editors. Braunwald's heart disease: a textbook of cardiovascular medicine. 8th ed. Philadelphia: WB Saunders; 2007. p. 287–331.
33. Garcia E, Botvinick EH, Hasagawa B, Ratzlaff N. Topic 1, physical and technical aspects of nuclear cardiology. Self-study program III. In: Botvinick E, editor. Nuclear medicine: cardiology. Society of Nuclear Medicine: Reston, VA; 2003.
34. Maltz OL, Treves S. Quantitative radionuclide angiocardiography. Determination of Qp/Qs in children Circulation. 1973;76:1049.
35. Bacharach SL, Green MV. Data processing in nuclear cardiology: measurement of ventricular function. IEEE Trans Nucl Sci. 1982;29:1343–54.
36. Strauss HW, Zaret BW, Hurley PJ. A scintigraphic method for measuring left ventricular ejection fraction in man without cardiac catheterization. Am J Cardiol. 1971;28:575–83.
37. Parker DA, Karvelis KC, Thrall JH, Froelich JW. Radionuclide ventriculography: methods. In: Gerson MC, editor. Cardiac nuclear medicine. 3rd ed. New York: McGraw Hill; 1997.
38. Links JM, Frank TL, Engdahl JC, Becker LC. Cardiac single-photon emission tomography with a 90 degrees dual-head system. Eur J Nucl Med. 1995;22:548–52.
39. Underwood SR, Walton S, Ell PJ, Jarritt PH, Emanuel RW, Swanton RH. Gated blood-pool emission tomography: a new technique for the investigation of cardiac structure and function. Eur J Nucl Med. 1985;10:332–7.
40. Bacharach SL, Green MV, Borer JS, Hyde JE, Farkas SP, Johnston GS. Left-ventricular peak ejection rate, filling rate, and ejection fraction—frame rate requirements at rest and exercise: concise communication. J Nucl Med. 1979;20:189–93.

41. Bacharach SL, et al. Assessment of ventricular function. In: Pohost GM, O'Rourke RA, Berman DS, Shah PM, editors. Imaging in cardiovascular disease. Philadelphia: Lippincott Williams & Williams; 2000.
42. Bonow R, Bacharach SL, Green MV. Impaired left ventricular diastolic filling in patients with coronary artery disease assessment with radionuclide angiography. Circulation. 1981;64:315–23.
43. Botvinick EH, Dae MW, O'Connell JW. Blood pool scintigraphy. Clin Cardiol. 1989;7:537–63.
44. Patel CD, Balakrishnan VB, Kumar L, Naswa N, Malhotra A. Does left ventricular diastolic function deteriorate earlier than left ventricular systolic function in anthracycline cardiotoxicity? Hell J Nucl Med. 2010;13:233–7.
45. Appel JM, Jensen BV, Nielsen DL, Ryberg M, Zerahn B. Systolic versus diastolic cardiac function variables during epirubicin treatment for breast cancer. Int J Cardiovasc Imaging. 2010;26:217–23.
46. Dae MW, Botvinick EH, O'Connell JW, Schiller NB, Bouchard A, Ports TA, Faulkner D. Increased accuracy of scintigraphic quantitation of valvular regurgitation using atrial-corrected Fourier amplitude ratios. Am J Noninvas Cardiol. 1987;1:155–62.
47. Frais M, Botvinick E, Shosa D, O'Connell JW. Phase image characterization of ventricular contraction in left and right bundle branch block. Am J Cardiol. 1982;50:95–103.
48. Kerwin W, Botvinick EH, O'Connell JW. Ventricular contraction abnormalities in dilated cardiomyopathy: acute effects of dual chamber simultaneous biventricular pacing to correct interventricular dyssynchrony. J Am Coll Cardiol. 2000;35:1221–7.
49. Munoz del Romeral L, Stillson C, Lesh M, Dae M, Botvinick E. The relationship of myocardial contraction and electrical excitation—the correlation between scintigraphic phase image analysis and electrophysiologic mapping. J Nucl Cardiol. 2009;16:792–800.
50. Munoz del Romeral L, Stillson C, Lesh M, Botvinick E. The variable functional effects of the pacing site in normal and scarred ventricles. J Nucl Cardiol. 2009;16:904–13.
51. O'Connell JW, Schreck C, Moles M, Badwar N, DeMarco T, Olgin J, et al. A unique method by which to quantitate synchrony with equilibrium radionuclide angiography. J Nucl Cardiol. 2005;12:441–50.
52. Lalonde M, Birnie D, Ruddy TD. deKemp RA, Wassenaar RW. SPECT blood pool phase analysis can accurately and reproducibly quantify mechanical dyssynchrony. J Nucl Cardiol. 2010;17:803–10.
53. Badhwar N, James J, Hoffmayer KS, O'Connell JW, Green D, De Marco T, Botvinick EH. Utility of equilibrium radionuclide angiogram-derived measures of dyssynchrony to predict outcomes in heart failure patients undergoing cardiac resynchronization therapy. J Nucl Med. 2016;57:1880–6.
54. Nichols KJ, Van Tosh A, Wang Y, Palestro CJ, Reichek N. Validation of gated blood-pool SPECT regional left ventricular function measurements. J Nucl Med. 2009;50:53–60.
55. Harel F, Finnerty V, Gregoire J, Thibault B, Marcotte F, Ugoloni P, Khairy P. Gated blood pool SPECT versus cardiac magnetic resonance imaging for the assessment of left ventricular volumes and ejection fraction. J Nucl Cardiol. 2010;17:427–34.
56. Oeff M, Scheinman MM, Abbott JA, Botvinick EH, Griffin JC, Herre JM, Dae MW. Phase image triangulation of accessory pathways in patients undergoing catheter ablation of posteroseptal pathways. Pacing Clin Electrophysiol. 1991;14:1072–85.
57. Germano G. Technical aspects of myocardial SPECT imaging. J Nucl Med. 2001;42:1499–507.
58. The Cardiovascular Imaging Committee, American College of Cardiology, The Committee on Advanced Cardiac Imaging and Technology, Council on Clinical Cardiology, American Heart Association, Board of Directors, Cardiovascular Council, Society of Nuclear Medicine. Standardization of cardiac tomographic imaging. J Am Coll Cardiol. 1992;20:255–6.
59. Germano G, Berman D. Acquisition and processing for gated perfusion SPECT: technical aspects. In: Germano G, Berman D, editors. Clinical gated cardiac SPECT. Armonk, NY: Futura; 1999. p. 93–113.
60. Botvinick E, Davis J, Dae M, O'Connell J, Schechtmann N, Abbott J, et al. Localization of ventricular tachycardia exit site and subsequent contraction sequence and functional effects with bedside radionuclide angiography. JACC Cardiovasc Imaging. 2008;1:605–13.
61. Nakajima K, Higuchi T, Taki J, Kawano M, Tonami N. Accuracy of ventricular volume and ejection fraction measured by gated myocardial SPECT: comparison of 4 software programs. J Nucl Med. 2001;42:1571–8.
62. Schaefer WM, Lipke CS, Standke D, Kühl HP, Nowak B, Kaiser HJ, et al. Quantification of left ventricular volumes and ejection fraction from gated 99mTc-MIBI SPECT: MRI validation and comparison of the Emory Cardiac Tool Box with QGS and 4D-MSPECT. J Nucl Med. 2005;46:1256–63.
63. Xia W, Lv Z, Wang G, Cai H, Ni J, Zhang Y, Ye B. A comparison and validation of blood-pool imaging and ECG-gated SPET myocardial perfusion imaging to assess left ventricular ejection fraction. Hell J Nucl Med. 2010;13(3):241–5.
64. Nakajima K, Nishimura T. Inter-institution preference-based variability of ejection fraction and volumes using quantitative gated SPECT with Tc-99m-tetrofosmin: a multicentre study involving 106 hospitals. Eur J Nucl Med Mol Imaging. 2006;33:127–33.
65. Honda N, Machida K, Mamiya T, Takahashi T, Takishima T, Hasegawa N, et al. Two-dimensional polar display of cardiac blood pool SPECT. Eur J Nucl Med. 1989;15:133–6.
66. Links JM, Devous MD Sr. Three-dimensional display in nuclear medicine: a more useful depiction of reality, or only a superficial rendering? J Nucl Med. 1995;36:703–4.
67. Metcalfe MJ, Cross S, Norton MY, Lomax A, Jennings K, Walton S. Polar map or novel three-dimensional display technique for the improved detection of inferior wall myocardial infarction using tomographic radionuclide ventriculography. Nucl Med Commun. 1994;15:330–40.
68. Botvinick EH, Hoffman JIE, Maddahi J, Garcia E, Rodrigues EA, Van Train K, Berman DS. Topic 5, myocardial perfusion scintigraphy-technical aspects. Self-study program III. In: Botvinick E, editor. Nuclear medicine: cardiology. Society of Nuclear Medicine: Reston, VA; 2003.
69. Indovina AG. Three-dimensional surface display in blood pool gated SPECT. Angiology. 1994;45:861–6.
70. Taillefer R, DePuey EG, Udelson JE, Beller GA, Benjamin C, Gagnon A. Comparison between the end-diastolic images and the summed images of gated Tc-99m sestamibi SPECT perfusion study in detection of coronary artery disease in women. J Nucl Cardiol. 1999;6:169–76.
71. Mok DY, Bartlett ML, Bacharach SL, et al. Can partial volume effects be used to measure myocardial thickness and thickening? IEEE Comp Cardiol. 1992;19:195–8.
72. Bacharach SL. Regional and global ventricular function. In: Dilsizian V, editor. Myocardial viability: a clinical and scientific treatise. Armonk, NY: Futura; 2000.
73. Botvinick EH, Dae MW, O'Connell JW. The scintigraphic evaluation of the cardiovascular system. In: Parmley WW, Chatterjee KC, editors. Cardiology. Philadelphia: JB Lippincott; 1983.
74. Yun J, Block M, Botvinick EH. Unique contraction pattern in patients after coronary bypass graft surgery by gated SPECT myocardial perfusion imaging. Clin Nucl Med. 2003;28:18–24.